DIPOLE MOMENTS AND NON-COVALENT BONDING IN GAS PHASE MOLECULES VIA ROTATIONALLY RESOLVED ELECTRONIC SPECTROSCOPY: BEYOND THE RIGID ROTOR

by

Diane Marie Miller

B.S., Franklin & Marshall College, 2003

Submitted to the Graduate Faculty of

Arts and Sciences in partial fulfillment

of the requirements for the degree of

Doctor of Philosophy

University of Pittsburgh

2010

UNIVERSITY OF PITTSBURGH

ARTS AND SCIENCES

This dissertation was presented by

Diane Marie Miller

It was defended on

August 12, 2010

and approved by

Committee Members:

Dr. Joseph J. Grabowski, Associate Professor
Department of Chemistry, University of Pittsburgh

Dr. Kenneth D. Jordan, Distinguished Professor of Computational Chemistry
Department of Chemistry, University of Pittsburgh

Dr. Timothy C. Steimle, Professor
Department of Chemistry & Biochemistry, Arizona State University

Dissertation Advisor:

Dr. David W. Pratt, Professor
Department of Chemistry, University of Pittsburgh

DIPOLE MOMENTS AND NON-COVALENT BONDING IN GAS PHASE MOLECULES VIA ROTATIONALLY RESOLVED ELECTRONIC SPECTROSCOPY: BEYOND THE RIGID ROTOR

Diane Marie Miller, PhD

University of Pittsburgh, 2010

Size, shape and charge play important roles in both the structure and dynamics of molecules. One prime example of this is the protein folding problem. Here, we use rotationally resolved fluorescence excitation spectroscopy to probe these properties of small, gas-phase molecules. The structures and permanent electric dipole moments of several substituted benzenes have been determined in both their ground and excited electronic states, providing insight into the nature of molecular charge distribution and how it changes upon the absorption of UV light. Non-covalent interactions are also explored; studies performed on a molecule composed of a flexible tail attached to a rigid aromatic body reveal information about the strength and character of π-hydrogen bonding.

TABLE OF CONTENTS

LIST OF TABLES

LIST OF FIGURES

LIST OF SCHEMES

LIST OF EQUATIONS

PREFACE

Foremost, I would like to thank my advisor, Dr. David Pratt, for being a source of inspiration and for giving me the opportunity to work in the world of high resolution spectroscopy. His approach to science and his tenacity helped me develop invaluable problem-solving skills. Most of all, I greatly admire his passion for education; he impressed upon me his belief that sharing science with the community is crucial and that we should strive to communicate our work to all audiences.

I would like to extend my deep appreciation to the previous and current Pratt group members. Not only did they help to make my research possible, but they also helped greatly in making the experience so enjoyable. I am especially thankful to Dr. Leonardo Alvarez-Valtierra, Dr. Cheolhwa Kang, Dr. Tri Nguyen, Alexei Nikolaev, and Dr. John Yi for mentoring me in the use of the lab equipment and for aiding in my understanding of the science behind the experiments; Dr. David Plusquellic and Dr. David Borst for their guidance with various computer programs; and Phil Morgan and Justin Young and for their assistance in the lab and for many helpful conversations.

I would also like to thank the department as a whole; I have had the pleasure of learning from many exceptional faculty members and of working with many dedicated, friendly staff members. In addition, I owe much thanks to the electronic, machine and glass shops—they were always willing to go above and beyond.

Finally, I am extremely grateful to my family and friends, especially my husband Pete, for their love, support, and encouragement.

1.0   INTRODUCTION

The gas-phase rotationally resolved fluorescence excitation spectrum (FES) of a molecule contains a wealth of information, including the molecule's structure or three-dimensional shape. This information comes from the rotational motions of the molecule, whose frequencies depend upon its moments of inertia. By modeling such a spectrum with a rigid rotor Hamiltonian, a molecule's rotational parameters can be determined. But, how can we learn even more? Further information can be gained by adding terms (when applicable) to the Hamiltonian. In this work, we will see that this concept can be exploited to gain knowledge of dipole moments and potential energy surfaces. The addition of terms has been achieved both by manipulation on the part of the researcher, like the inclusion of a static electric field to probe dipole moments, and by an inherent need based upon the dynamics of the system under study, such as is the case with torsional motion.

When we push deeper for information, we can find ourselves at a loss of experimental signal—for example, in the dipole moment experiments, the fluorescence intensity present in the absence of an electric field spreads out, decreasing the signal-to-noise. Pursuing the information revealed in the FES then becomes an issue of UV laser power. Chapter 2 discusses the implementation and setup of a Spectra-Physics Wavetrain external frequency doubler, a replacement for the previous intra-cavity doubling system. External doubling greatly increased UV power, allowing the study of systems that were previously beyond our grasp.

In Chapter 3, we look at *p*-aminobenzoic acid (PABA). PABA is classified as a "push-pull" molecule, with two substituents, an amino group and a carboxyl group, that may donate or withdraw electron density to or from the benzene ring. We determine the permanent electric dipole moments of PABA in its ground and excited electronic states and examine how the dipole moment changes upon excitation. Comparison is made to aniline, which has only an amino substituent.

In Chapter 4, we continue our investigation of permanent electric dipole moments, focusing on a family of aminobenzonitrile (ABN) molecules. Here, the dipole moments of 2-aminobenzonitrile (2ABN) and 3-aminobenzonitrile (3ABN) are determined in both the ground and excited states. Comparison is made to 4-aminobenzonitrile (4ABN), as well as to *ab initio* values. In addition, we address the question of whether dipole moments are additive by comparing the results to those for aniline and benzonitrile, molecules which each possess only one of the two substituents present in the ABNs.

In Chapter 5, we study 9-fluorenemethanol (9FM), consisting of a flexible –CH_2OH tail attached to a fluorene ring. Two conformers, *sym*-9FM and *unsym*-9FM, were detected, and of these conformers, it is observed that *sym*-9FM undergoes torsional motion of the –OH group. Further investigation of this motion using selectively deuterated 9FM provides detailed information about the π-hydrogen bonding interaction between the –CH_2OH tail and the aromatic system to which is attached.

In Appendix A, we further discuss and compare the experimentally determined dipole moments given in Chapters 3 and 4. In Appendix B, we examine the ground state potential energy surface of 9FM and 9FMD. In Appendix C, we describe collaborative work done on a

series of ethynylstyrenes and on *p*-vinylphenol. Both cases demonstrate how rotational spectroscopy can be used to distinguish between different molecular structures.

2.0   INCREASING UV LASER POWER: EXTERNAL CAVITY DOUBLING VIA A
SPECTRA-PHYSICS WAVETRAIN

In order to broaden the scope of research in the Pratt lab, more laser power was needed. Previously, UV laser light was generated with an intra-cavity frequency doubling setup, and typical power outputs were on the order of 100 - 400 µW.   The implementation of an external frequency doubling setup *via* a Spectra-Physics Wavetrain resulted in typical power outputs of 500 µW to 2 mW.

2.1   MOTIVATION

The Pratt group has studied the laser induced fluorescence of a large number of molecules, including complexes, with high resolution.[1] These experiments were conducted using a previously described setup,[2] which utilized intra-cavity frequency doubling for the conversion of visible light to UV. However, these studies have been limited to molecules that fluoresced in certain wavelength regions,[3] and, moreover, to relatively bright molecules (*i.e.*, molecules that could be studied with a few hundred microwatts of UV laser power). To make possible more challenging endeavors, such as the study of weakly fluorescing molecules and complexes, molecules in hard-to-reach wavelength regions, and dipole moments using Stark experiments,

greater laser power was needed. This was achieved by switching to an external frequency

doubling setup, which offers a higher conversion efficiency.

2.2   EXTERNAL DOUBLING SETUP

The previous setup[2] of the ring dye laser featuring intra-cavity frequency doubling is

shown in Figure 2.1. It can be seen in this figure that UV light exits the laser at M3, and a very

small amount of visible light is allowed to leak out at M4. For intra-cavity doubling, it is ideal

for mirrors M1-M4 to be 100% reflective in the visible region. In order to convert to
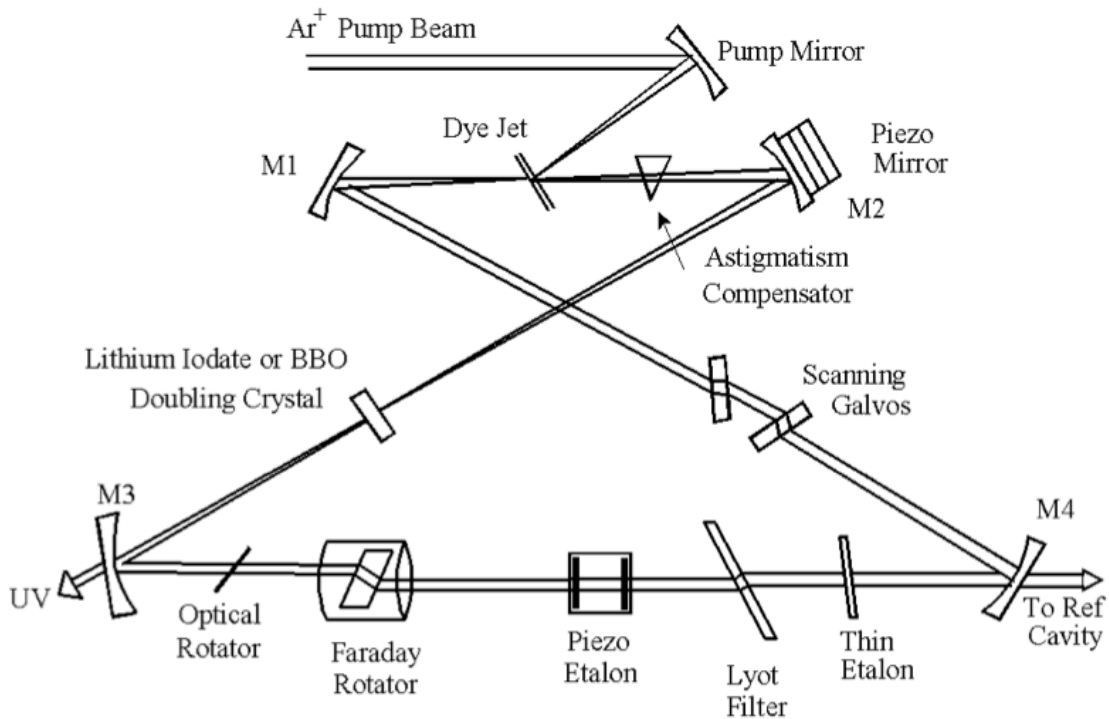
Figure 2.1. Schematic of the ring dye laser, as shown for intra-cavity frequency doubling.

external doubling, the doubling crystal was removed, and it was necessary that a sufficient amount of visible light was allowed to exit the ring dye laser. This was achieved by reducing the reflectance of one of the mirrors. M4 was selected as the mirror to be modified due to its location on the laser table and because it is flat (several of the other mirrors possess some degree of curvature). It was determined that M4 should have a reflectivity of ~ 95% in order to achieve optimum power output.[4]

After the described modification, the visible output of the ring dye laser from M4 ranged from 40 – 180 mW. This beam was directed toward a Spectra-Physics Wavetrain with two steering mirrors. While the majority of power was sent into the Wavetrain itself, beam splitters were used to send small portions of the light to an iodine cell for frequency matching purposes[2] and to a reference cavity for scanning and stabilization.[2] See Figure 2.2.

Inside the Wavetrain cavity, a crystal (either LBO or BBO) was used to achieve doubling. The output (UV light) was then redirected by several mirrors to a set of steering mirrors, which were finely tuned to guide the UV laser beam directly into the molecular beam, as described previously.[2] Two lenses, shown in Figure 2.2, were used to refocus the beam. Typically, this setup produced 500 μW to 2 mW of UV.

2.3   RESULTS

Implementation of the Wavetrain has allowed studies on molecules (and complexes) that were not previously possible. One prime example of this is *p*-aminobenzoic acid, or PABA (which is discussed in further detail in Chapter 3). While the fluorescence quantum yield of
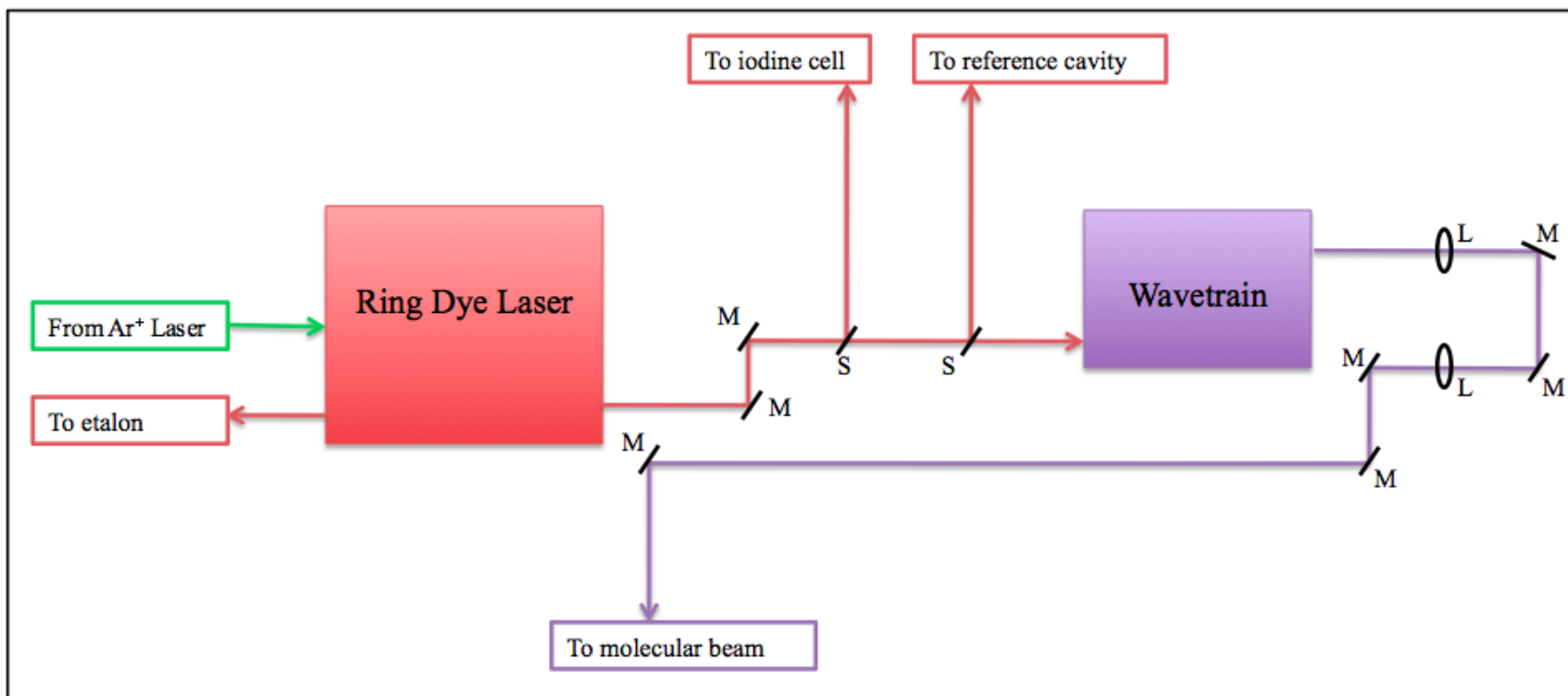
Figure 2.2. Schematic for the setup of the Wavetrain. L = lens, M = mirror, and S = beam splitter.

PABA is fairly high,[5] the collected fluorescence was relatively weak because PABA decomposes with heating (our method for getting it into the gas phase). Intra-cavity frequency doubling in this wavelength region produced ~ 300 μW of UV power, but the signal-to-noise ratio for PABA was poor (see Figure 2.3).[6] External frequency doubling produced ~ 1 mW of power, and we obtained the spectrum seen in Figure 2.4.
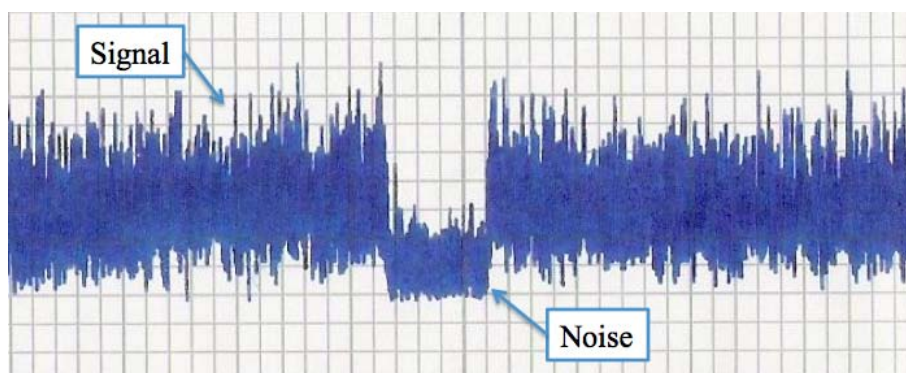
Figure 2.3. PABA signal to noise, as collected using intra-cavity frequency doubling.
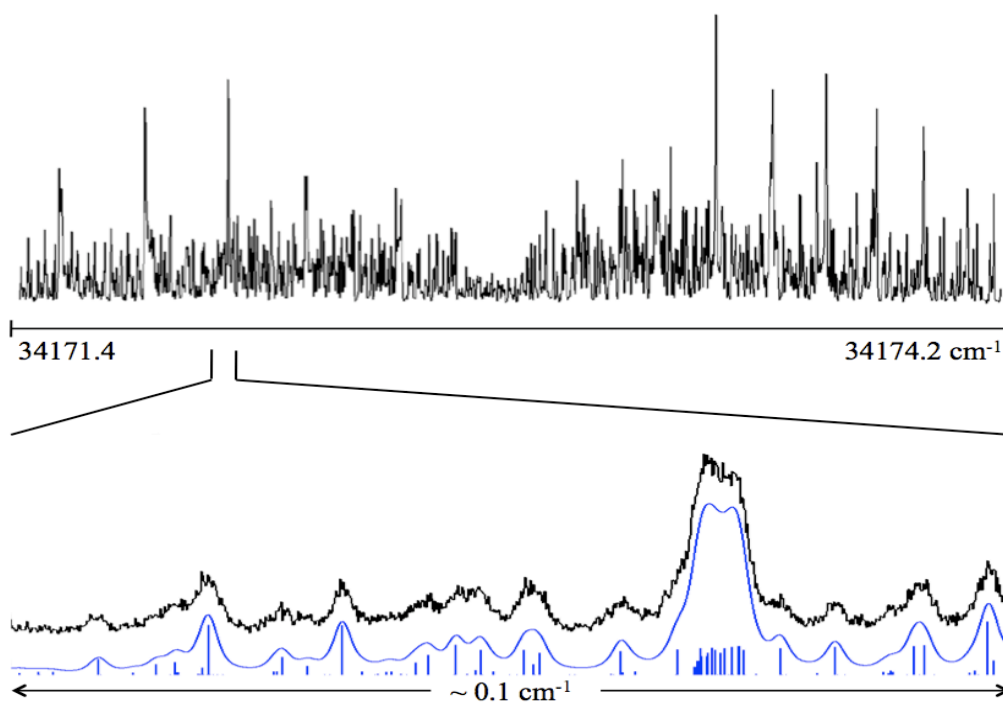
Figure 2.4. The origin spectrum of PABA. In the bottom panel, the experimental trace (black) is compared to two simulations (blue) with and without a convoluted lineshape function.

8

2.4   ACKNOWLEDGEMENTS

2.5   REFERENCES AND NOTES

1. See for example: (a) A. Held, B. B. Champagne, and D. W. Pratt. *J. Chem. Phys.* **95**, 8732 (1991), (b) S. Jagannathan and D. W. Pratt. *J. Chem. Phys.* **100**, 1874 (1994), (c) T. M. Korter, D. W. Pratt, and J. Küpper. *J. Phys. Chem. A*, **102**, 7211 (1998), (d) J. A. Reese, T. V. Nguyen, T. M. Korter and D. W. Pratt. *J. Am. Chem. Soc.* **126**, 11387 (2004), and (e) T. V. Nguyen, T. M. Korter, and D. W. Pratt. *Mol. Phys.* **103**, 1603 (2005).

2. W. A. Majewski, J. F. Pfanstiel, D. F. Plusquellic and D. W. Pratt, in *Laser Techniques in Chemistry.* T. R. Rizzo and A. B. Meyers, Eds. J. Wiley & Sons: New York (1995); p. 101.

3. Due to the nature of the dye curves, and also the coatings of the mirrors inside the cavity of the ring dye laser, not all wavelengths produce the same power of visible light (*i.e.*, the light produced in some regions is very weak). Therefore, it was difficult to get "workable" power outputs for certain wavelengths.

4. This value was selected based on the publication, C. V. Shank, J. Edighoffer, A. Dienes and E. P. Ippen. *Opt. Commun.* **7**, 176 (1973), and from conversations with L. E. Jusinski.

5. J. M. Bello and R. J. Hurtubise, *Appl. Spectrosc*. **42**, 619 (1988).

6. Note that Figure 2.3 is the result of a "fast scan," where the UV light produced was quickly and repeatedly scanned over several wavenumbers (coinciding with the origin band frequency of PABA). The noise was recorded by blocking the UV laser light from interacting with the molecular beam.

3.0 PUSH-PULL MOLECULES IN THE GAS PHASE. STARK-EFFECT MEASUREMENTS OF THE PERMANENT DIPOLE MOMENTS OF *p*-AMINOBENZOIC ACID IN ITS GROUND AND ELECTRONICALLY EXCITED STATES

3.1   ABSTRACT

Stark effect measurements of the permanent electric dipole moments of p-aminobenzoic acid (PABA) in the gas phase are reported, based on studies of its fully resolved $S_1 \leftarrow S_0$ electronic spectrum in the presence of an electric field. Ground state (S_0) PABA has $\mu = 3.3$ D, whereas excited state (S_1) PABA has $\mu = 4.4$ D. Despite PABA's reputation as a "push-pull" molecule, the photon-induced change in both the magnitude and orientation of μ is relatively small. Possible reasons for this behavior are discussed.

3.2   INTRODUCTION

Knowledge of the permanent electric dipole moment of a molecule can give us a wealth of information. Among other things, it can allow us to determine a molecule's conformation.[1,2] Electric deflection experiments are currently being used to measure the ground state dipole moments of biomolecules in the gas phase, and these values have been used to make conclusions about peptide motion and shape.[3,4] Recently, helix formation in alanine-based peptides was investigated; based on dipole measurements, it was suggested that the peptides formed β-sheets in the gas phase, which was surprising, as they usually form α-helices in solution.[4]

Dugourd and coworkers have also studied some smaller molecules, such as p-aminobenzoic acid (PABA).[5] PABA, shown in Figure 3.1, can be classified as a "push-pull" molecule, with two substituents, an amino group and a carboxyl group, that may donate or withdraw electron density to or from the benzene ring. PABA has been the focus of other gas phase studies,[6] including deflection studies of its dimer.[7,8]

High resolution fluorescence excitation spectroscopy performed in the presence of an electric field is a powerful tool that allows us to determine the electric dipole moments of isolated molecules by tracking the Stark shifts of individual transitions.[9] Here, this technique has been applied to PABA. We measure both the ground- and excited-state permanent electric dipole moments of PABA in the gas phase. Comparison is made to the electric deflection results and also to aniline (AN).
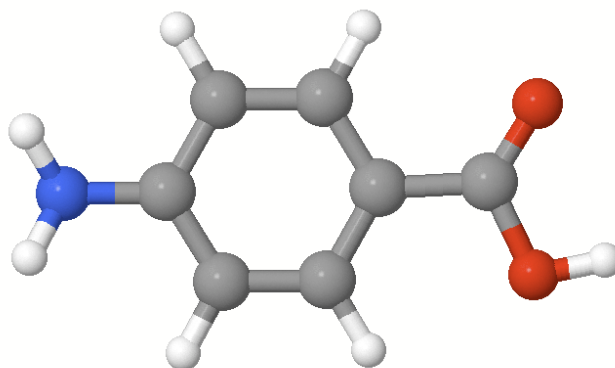
Figure 3.1. Structure of PABA.

3.3   EXPERIMENTAL

PABA (99% purity) was purchased from Sigma-Aldrich and used without further purification. To obtain vibrationally resolved LIF spectra, a 50/50 mixture of PABA and diatomaceous earth was heated to ~ 130 °C, seeded into ~ 2 kTorr of dry helium gas (> 90% purity), and expanded through a 1 mm diameter orifice pulsed valve (General Valve Series 9), operating at 10 Hz, into a vacuum chamber (10^{-5} Torr). Diatomaceous earth was used in order to limit decomposition of PABA. The gaseous sample was then crossed 2 cm downstream with the

output of a Quanta Ray Nd^{3+}: YAG (Model DCR-1A) pumped dye laser (Model PDL-1), using a mixture of Kiton Red and Rhodamine 590 dyes. Frequency doubling was done externally with a potassium dihydrogen phosphate (KDP) crystal. The visible portion of the laser output was filtered, leaving ultraviolet (UV) light with a spectral resolution of ~ 1 cm^{-1}. A photomultiplier tube (EMI 9813QB), positioned at right angles to both the laser and molecular beams, was used to collect the fluorescence. The data were processed by a boxcar integrator (Stanford Research Systems) and recorded using Quick Data Acquisition software (version 1.0.5).

Rotationally resolved experiments were performed using a molecular beam laser spectrometer, described elsewhere.[10] Briefly, the sample was heated to ~ 190 ºC, seeded in dry argon gas (> 99% purity), and expanded into a vacuum through a 240-µm quartz nozzle. The molecular beam was skimmed 2 cm downstream with a 1 mm diameter skimmer and then crossed 15 cm downstream with the frequency-doubled output of the dye laser. Rhodamine 590 dye was used, and ~ 1 mW of UV light was produced. Fluorescence was collected using spatially selective optics and detected by a photomultiplier tube (EMI 9813QB) and photon counting system. An iodine absorption spectrum and relative frequency markers were simultaneously collected. All information was processed using the jba95 data acquisition system.[10] Absolute transition frequencies in the excitation spectrum were determined by comparison with the I_2 absorption spectrum (accuracy $\approx$ 30 MHz). The frequency markers were generated by a stabilized etalon with a free spectral range of 299.7520 ± 0.0005 MHz at the fundamental frequency of the dye. Fitting of the field-free spectrum was done using the jb95 least squares fitting program.[11] The experimental set-up of the Stark cell and general analysis of Stark spectra have been described elsewhere.[9]

The high resolution spectra of PABA both in the presence and absence of an applied electric field are relatively weak; we presume that this is due to the decomposition of PABA upon heating (the fluorescence quantum yield is fairly high).[12] For this reason, the intracavity frequency doubler in our modified Spectra-Physics 380D ring laser was replaced by a Wavetrain external frequency doubler, also manufactured by Spectra-Physics. UV power levels of ~ 1 mW were generated using the Kiton Red/Rhodamine 590 dye mixture and a BBO doubling crystal cut for 600 nm, a factor of three improvement over intracavity doubling in this frequency region. Details of the setup have been provided in Chapter 2 of this work.

3.4   RESULTS

Figure 3.2 shows the vibrationally resolved fluorescence excitation spectrum (FES) of PABA. It is similar in many respects to the REMPI spectrum of laser-desorbed PABA taken by Meijer, *et al.*[6] The electronic origin is the strongest band in both spectra, and their frequencies are very nearly the same. There is also extensive vibrational structure in both spectra. However, there are significant differences in both the frequencies and intensities of the observed vibronic bands in the two spectra. Possibly, these differences may be traced to the different sample preparation methods; some decomposition of PABA no doubt occurs at the high temperatures that were used in our experiment. But it is also possible that there are some differences in the quantum yields of fluorescence and ionization when exciting different vibronic bands.

The rotationally resolved FES spectrum of the origin band of PABA is shown in Figure 3.3. Lacking a strong Q-branch, it is a *b*-type spectrum, with the transition moment lying

0_0^0
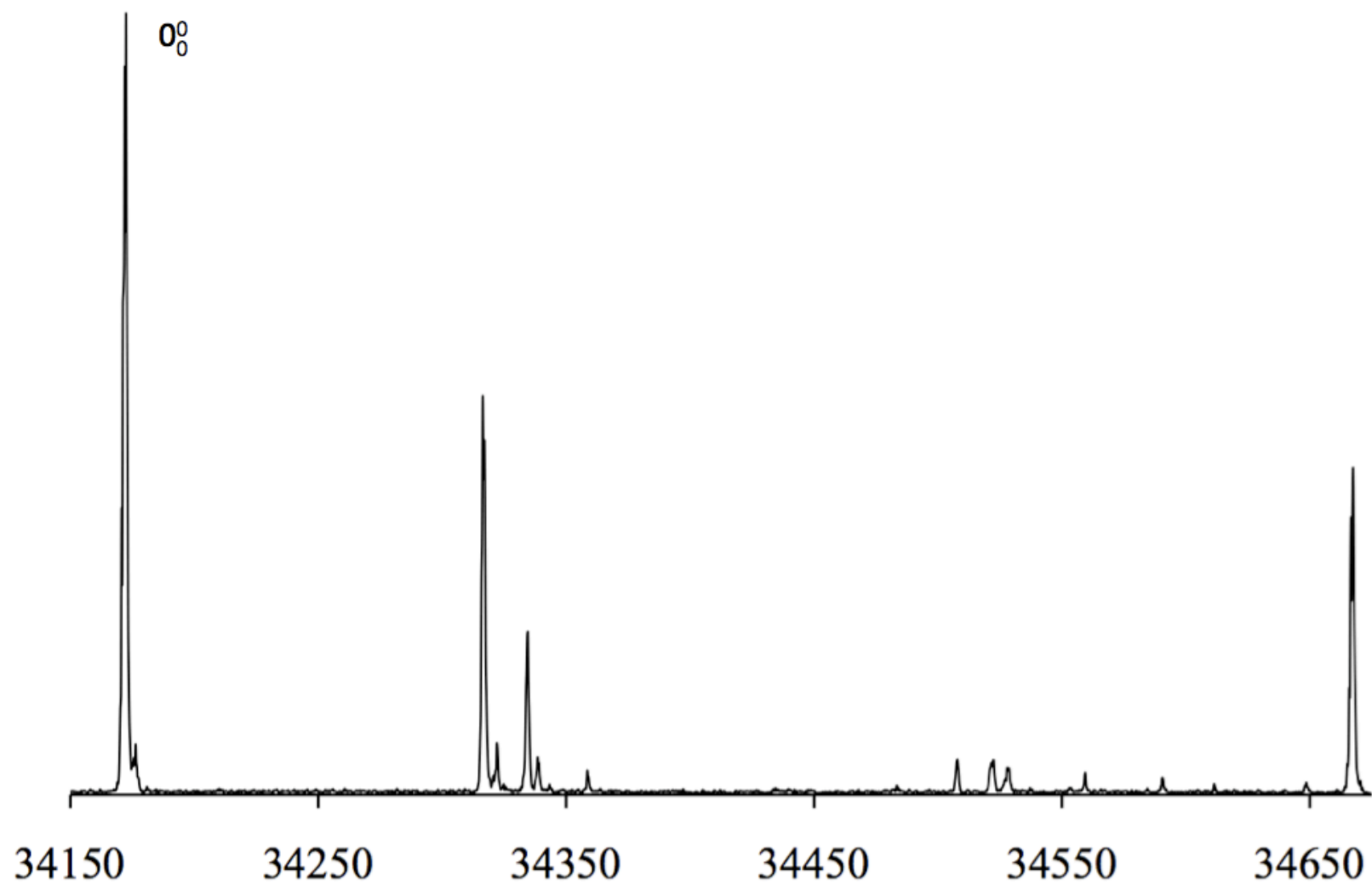
Figure 3.2. Low resolution fluorescence excitation spectrum of PABA.

primarily along the *b*-axis. A simulation was created using rotational constants obtained from *ab initio* calculations,[13] and these constants were varied until there was good overall agreement between the experimental spectrum and the simulation. Figure 3.3 shows a portion of the simulation; each individual line in the simulation represents an individual $|J'K_a'K_c'> \leftarrow |J''K_a''K_c''>$ transition, and width has been added to reproduce the overall shape seen in the experiment. Over 100 transitions were assigned, and the best fit had an OMC (observed minus calculated standard deviation) of 2.4 MHz. The parameters obtained from this fit are given in Table 3.1. Rotational constants are in good agreement with calculations, with differences of 1% or less, less for the ground state.

Table 3.1. Experimental inertial parameters of PABA. Parameters calculated at the MP2/6-31G** and CIS/6-31G** levels of theory have also been included for comparison.

	Experimental	**Calculated**	**% Error**
S_0			
A (MHz)	3833.6 (1)	3821.3	0.3
B (MHz)	793.2 (1)	791.8	0.2
C (MHz)	657.8 (1)	656.3	0.2
ΔI (amu Å^2)	-0.66	-0.48	
S_1			
A (MHz)	3692.3 (1)	3740.2	1.3
B (MHz)	795.5 (1)	804.7	1.2
C (MHz)	655.1 (1)	662.5	1.1
ΔI (amu Å^2)	-0.67	-0.32	
a/b/c	5/95/0		
Origin (cm^{-1})	34172.8		
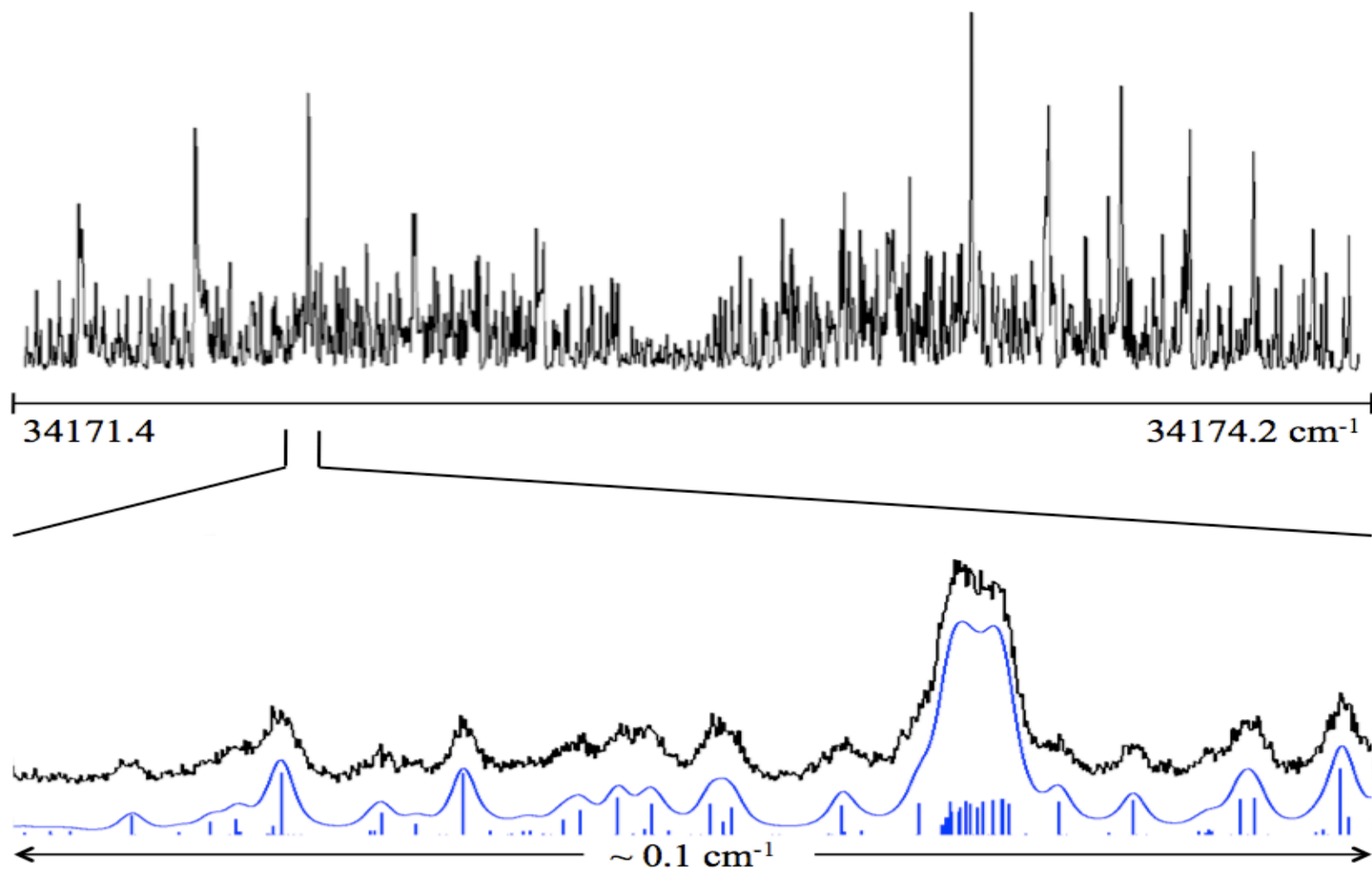
Figure 3.3. The field-free origin spectrum of PABA, occurring at 34,172.8 cm^{-1}. Also shown in the bottom panel is a comparison of a small portion of the experimental spectrum (black trace) with two simulated spectra (blue trace), with and without a convoluted lineshape function.

The linewidth of individual transitions in the rotationally resolved origin band was fit using a Voigt profile comprised of a Gaussian linewidth of 18 MHz and a Lorentzian linewidth of ~ 30 MHz. The Gaussian component is due to Doppler broadening of the molecular beam; the Lorenztian component comes from lifetime broadening of the molecule. Based on our value of 30 MHz, the first excited state of PABA has a lifetime around 5.3 ns. This is much longer than estimated by Meijer, *et al.*,[6] who put the lifetime at a few hundred picoseconds. If the lifetime were that short, the lines seen in our experiment would be much broader, and we would not observe a resolved spectrum.

Application of an electric field causes transitions seen in the field-free spectrum to split and shift in frequency, as shown in Figure 3.4. The magnitudes of these shifts depend on both the field strength and dipole moment values. A special program[9] was used, in conjunction with jb95, to simulate and fit the experimental Stark spectra. This program carries out an exact diagonalization of truncated matrices and uses the following Hamiltonian,

$$\hat{H} = \hat{H}_r + \hat{H}_e \tag{3.1}$$

The first term, $\hat{H}_r$, is the rigid-rotor Hamiltonian,

$$\hat{H}_r = AJ_a^2 + BJ_b^2 + CJ_c^2 \tag{3.2}$$

and $\hat{H}_e$ is the Stark Hamiltonian,

$$\hat{H}_e = -E_Z \sum_{g=a,b,c} \mu_g \phi_{Z_g} \tag{3.3}$$

Here, A, B and C are the rotational constants; J_a, J_b and J_c are the projections of the angular momentum on the a, b and c inertial axes; E_Z represents the electric field applied along the Z axis; μ_a, μ_b and μ_c are the dipole moment components along each inertial axis; and the direction cosines relating the lab and molecular frames are represented by ϕ. Other details have been
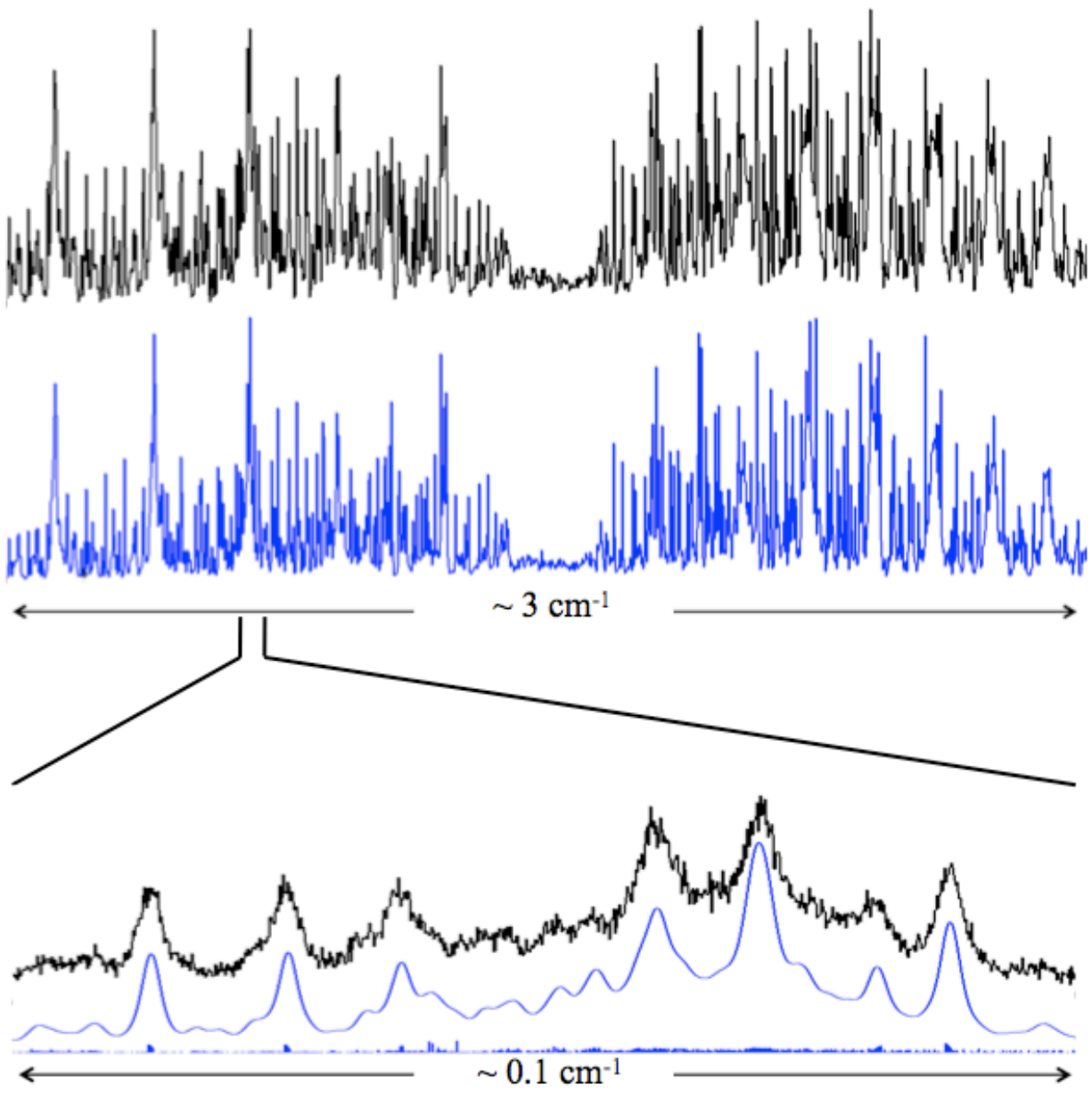
Figure 3.4. Origin spectrum of PABA, at a calibrated electric field strength of 1184 V/cm. The black trace is the experimental spectrum, and the blue trace is the simulated spectrum. The top portion shows the whole spectrum, while the bottom trace shows a close up of the highlighted section, again with and without a convoluted lineshape function.

described previously.[9]   Recently, an improvement was made that more fully integrated the programs. One of the main features is a set of trackbars that allows the user to change the dipole moment components and "instantly" see the effects on the simulation.

Different transitions in the spectrum are affected differently by the application of the field. Certain transitions are more sensitive than others, both to the application of the electric field and to the different dipole moment components. This is illustrated in Figure 3.5. The positions of P- and R-branch lines with high K values, particularly those equal or nearly equal to J, are especially sensitive to μ_a, the positions of Q-branch lines are especially sensitive to μ_b, and the positions of the lines with $K_a = 0$ are especially sensitive to μ_c. Thus, to fit the spectrum in Figure 3.4 (and others at other field strengths), we first estimated μ_a, μ_b and μ_c using *ab initio* methods, simulated an overall spectrum, and then focused on individual transitions that are most sensitive to the different dipole moment components to obtain a final fit of the observed spectrum. This is also shown in Figure 3.4. Typical OMC values of these fits are 7 MHz, substantially less than the linewidth.

3.5   DISCUSSION

The value of μ_a obtained by electric deflection methods, 2.8 (2) D,[4] is in reasonable agreement with our directly measured value of 3.12 (8) D. This is not too surprising, since PABA is a near symmetric top and behaves well in an electric field.[5,14] In addition to the μ_a component, we are also able to measure the μ_b and μ_c components of the dipole moment, and we
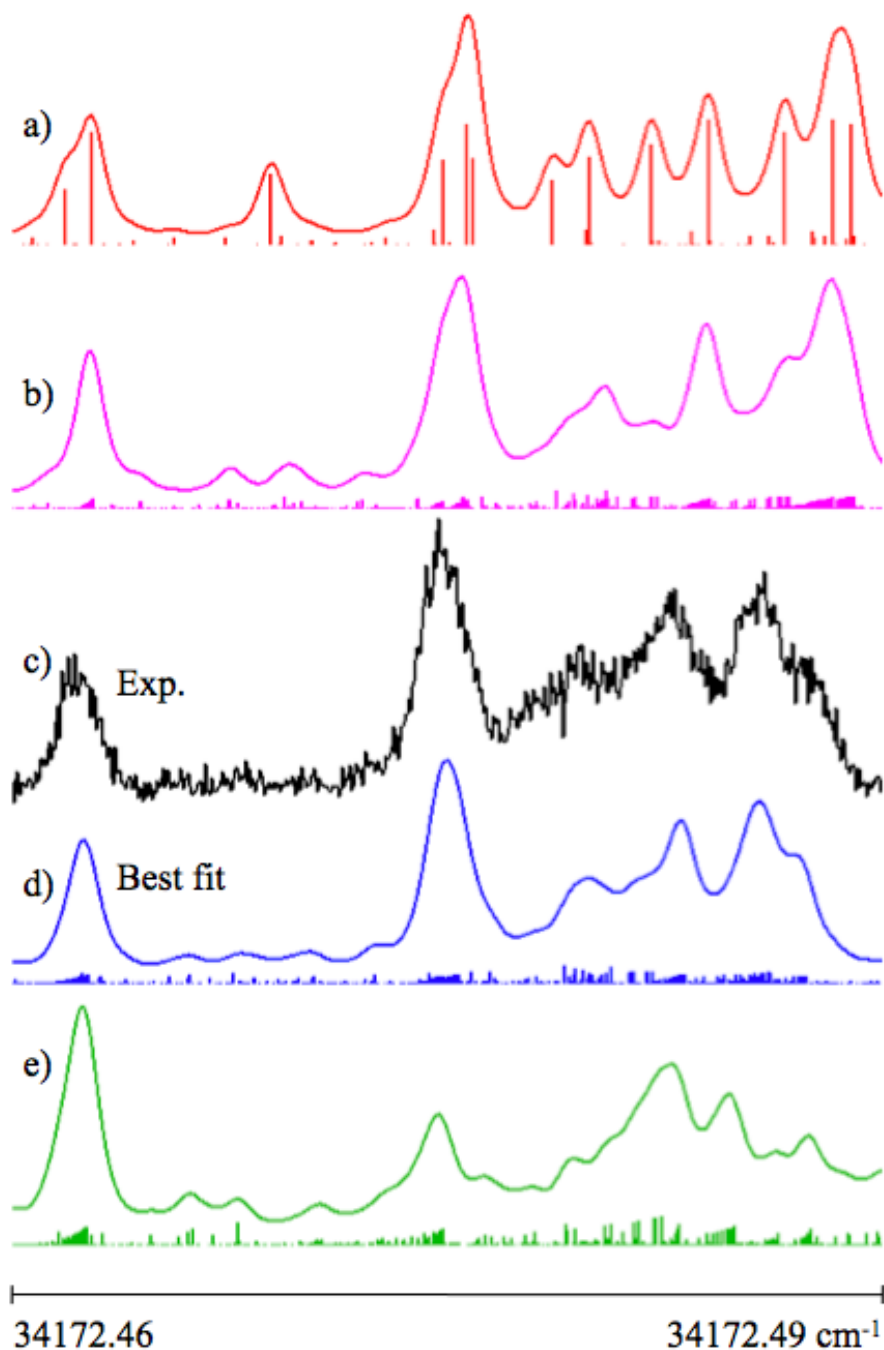
Figure 3.5. Several simulations, both with and without a convoluted lineshape function, are compared to a portion of the Q-branch of the experimental spectrum to illustrate the dependence of the Stark spectra on the various dipole moment components. Simulation (a) is the zero-field spectrum, and traces (b) - (e) are at a calibrated field strength of 1184 V/cm. All simulations use the experimental rotational constants in Table 3.1. Simulation (b) assumes $\mu_a'' = 3.12$ and $\mu_a' = 4.21$ D, with the other components set to zero. The experimental spectrum (c) is shown for comparison. Below, simulation (d) is shown with $\mu_a'' = 3.12$, $\mu_a' = 4.21$, $\mu_b'' = 1.2$, $\mu_b' = 1.3$, $\mu_c'' = 0.0$ and $\mu_c' = 0.0$ D (the parameters obtained from our fits). Finally, simulation (e) was created with non-zero values of all dipole moment components, with $\mu_a'' = 3.12$, $\mu_a' = 4.21$, $\mu_b'' = 1.2$, $\mu_b' = 1.3$, $\mu_c'' = -1.26$ and $\mu_c' = -0.86$ D. The assumed values of μ_c are the calculated ones (Table 3.2).

are able to measure all components in the electronically excited state. Thus, we also determine the orientation of the dipole moment in the molecular coordinate system, and how it changes when the photon is absorbed.

The experimentally determined values of the dipole moment components are shown in Table 3.2. In general, the measured values of the components of μ are substantially different from the calculated ones, with errors up to 31%. A special case is the out-of-plane component, μ_c. From our fits, μ_c was determined to be zero in both states, despite calculations predicting non-zero values; this has also been observed for AN.[9] A planar molecule would have $\mu_c = 0$. PABA, like AN, is relatively planar, except for the amino group which is positioned out of the plane. Calculations estimate the dihedral angle between the NH_2 and C_6H_4N planes to be ~28° in the ground state and ~20° in the excited state. In aniline, the amino group undergoes an inversion motion that is fast relative to the rotational motion, resulting in an average value of zero for μ_c.[9,16] We presume the same is true for PABA.

Table 3.2. Experimental dipole moment values for PABA. Parameters calculated at the MP2/6-31G** and CIS/6-31G** levels of theory have also been included for comparison.

	Experimental	Calculated	% Error
S$_0$			
μ_a (D)	3.12 (8)	2.75	11
μ_b (D)	1.2 (2)	1.2	0
μ_c (D)	0.00 (1)	-1.18	
μ (D)	3.3 (2)	3.24	
S$_1$			
μ_a (D)	4.21 (8)	5.35	27
μ_b (D)	1.3 (2)	1.7	31
μ_c (D)	0.00 (1)	-0.82	
μ (D)	4.4 (1)	5.69	

Figure 3.6 shows a comparison of the molecular orbitals of aniline and PABA. The HOMO-1 (ϕ_2), HOMO (ϕ_3), LUMO (ϕ_4), and LUMO-1 (ϕ_5) orbitals are depicted. For PABA, the nodal pattern of the LUMO and LUMO+1 orbitals are reversed, relative to AN. On the basis of results observed for different conformations of alkyl benzenes,[17] this is not surprising; addition of the carboxyl group to AN breaks the symmetry of the molecule, rotating the positions of the nodal planes of the LUMO and LUMO+1 orbitals.

Calculations done at the CIS/6-31G** level of theory predict the S_1 state of AN to be a linear combination of one-electron excitations, $\Psi(S_1) = 0.28 \, (\phi_2\phi_5) + 0.64 \, (\phi_3\phi_4)$, with small contributions from other excitations. For PABA, calculations done at the same level of theory predict a similar combination; $\Psi(S_1) = 0.20 \, (\phi_2\phi_5) + 0.65 \, (\phi_3\phi_4)$, with small contributions from other excitations. The dominant excitation for both is HOMO to LUMO, and by multiplying the signs of these orbitals, we can predict the transition moment orientation of the excitation in PABA. The result of this multiplication is depicted in the lower portion of Figure 3.6, and it shows that the predicted transition moment should lie parallel to the *a* axis for PABA. However, our experiments clearly show that the $S_1 \leftarrow S_0$ transition is *b*-type, which means that the ordering of the molecular orbitals must follow that of AN. We conclude that the slight breaking of the symmetry by the carboxyl group must have a negligible effect on the positions of the nodal planes of the molecular orbitals of PABA.

The ground- and excited-state total dipole moments of PABA and AN are depicted in Figure 3.7. It should be noted that we do not obtain the direction of the dipole components from our fits; the directions shown in the figure are based on chemical intuition and the results of *ab initio* calculations. A comparison of the dipole moment values of PABA and AN is made in
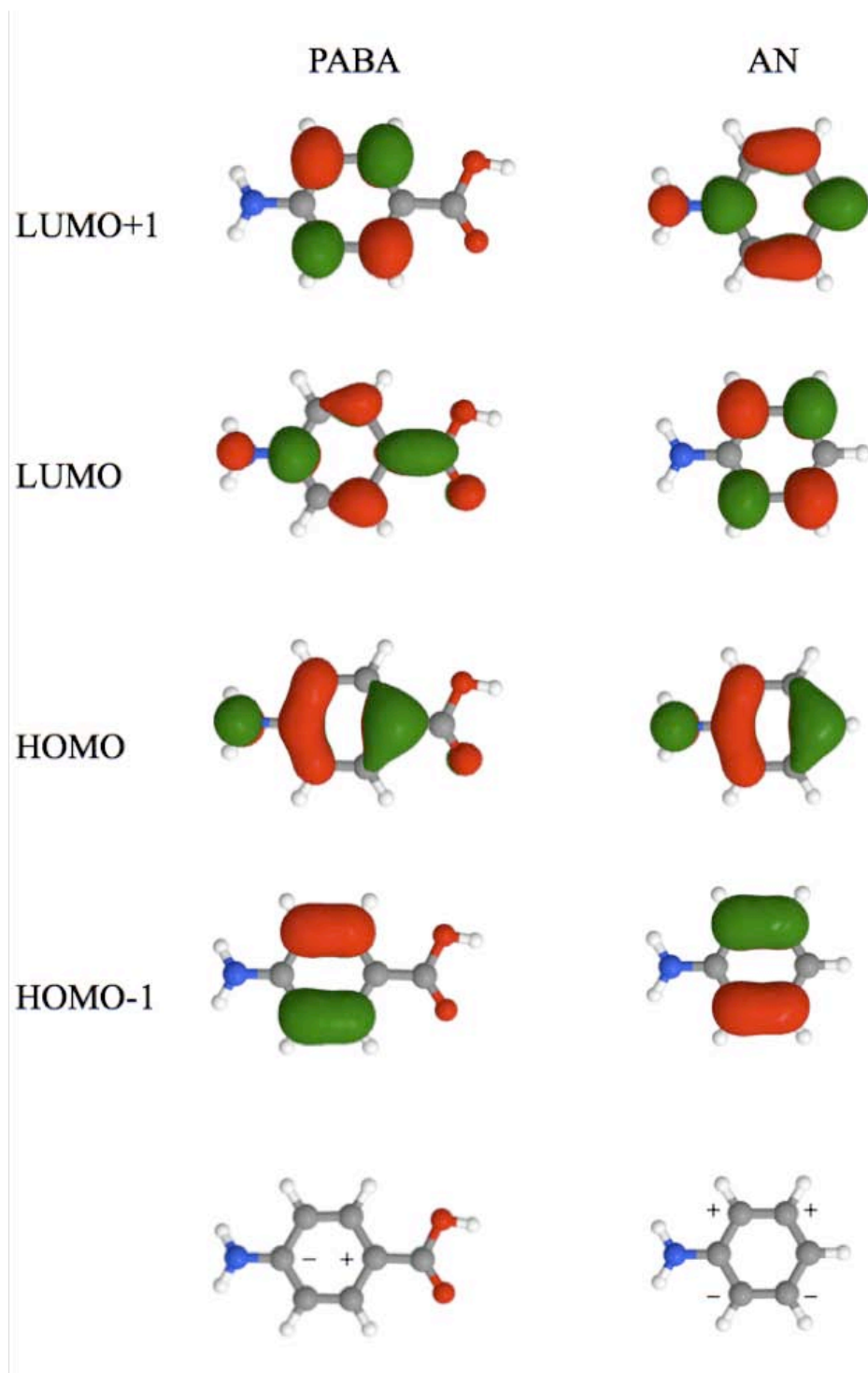
Figure 3.6. HOMO-1 (ϕ_2) , HOMO (ϕ_3) , LUMO (ϕ_4) , and LUMO-1 (ϕ_5) orbitals of PABA and AN, as predicted by HF/6-31G** calculations. The bottom portion shows the result of multiplication of the signs of the ϕ_3 and ϕ_4 orbitals, giving predicted transition moment orientations.
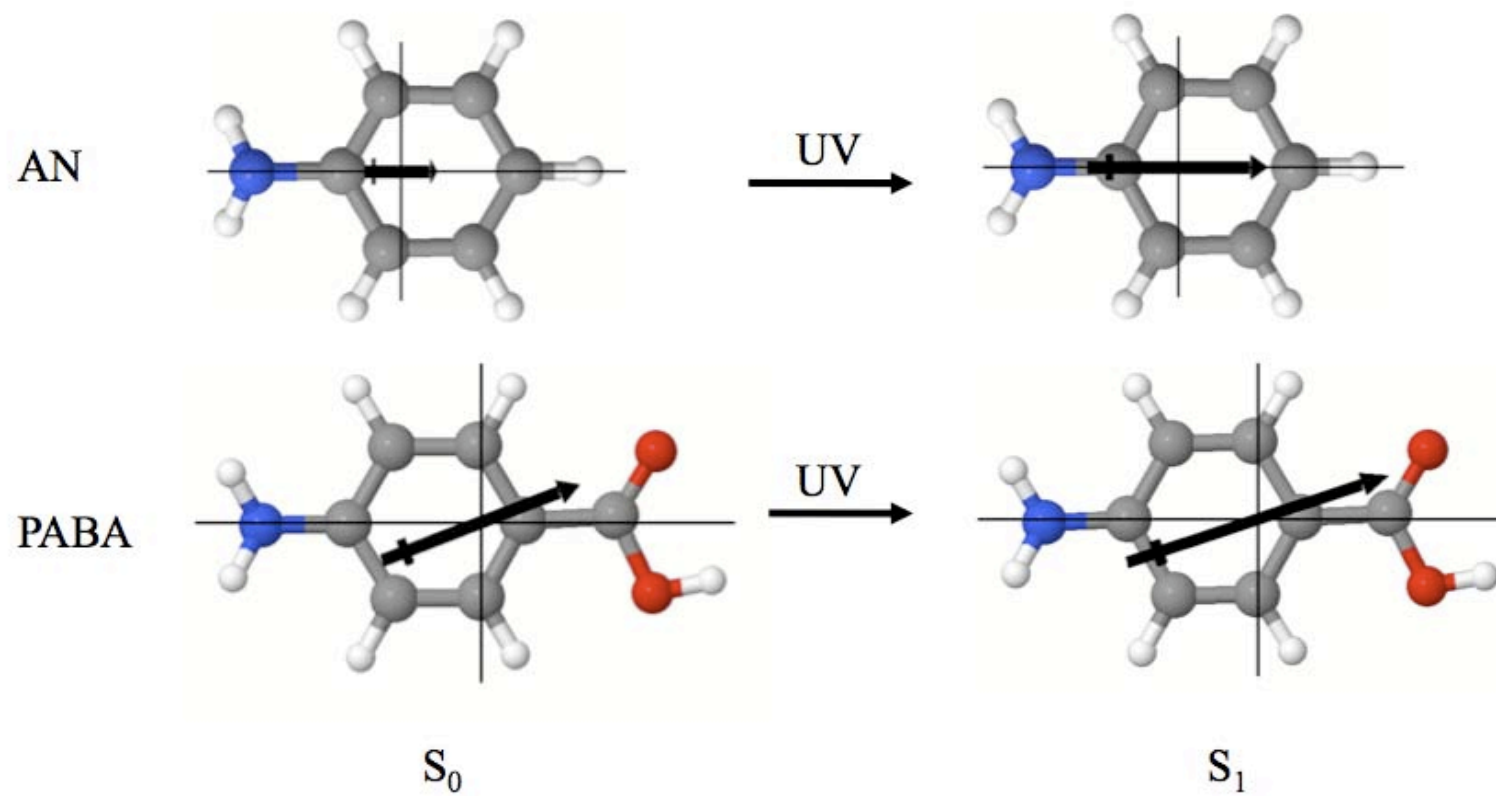
Figure 3.7. Arrows depicting the dipole moment magnitudes and orientations of PABA and AN in both the ground and excited states.

Table 3.3. The ground state μ_a dipole moment component of PABA, 3.12 (8) D, is larger than that of AN, 1.129 (5) D. This is due to the presence of the carboxyl group on PABA; -COOH groups are electron withdrawing (see Figure 3.6). Another measure of this effect is the proton affinity of the molecule in the gas phase, the energy released in the reaction $B + H^+ \rightarrow BH^+$. AN has a proton affinity of 877 kJ/mol, whereas that for PABA is somewhat less, 864.7 kJ/mol,[18] owing to the decrease in electron density on the -NH$_2$ group. Also notable is the magnitude μ_b of in PABA; the difference in the electron densities of the =O and –OH groups must be quite substantial, as μ makes a large angle with the a axis ($\sim 21°$ in S$_0$ and $\sim 18°$ in S$_1$).

The change in μ_a upon excitation is larger in AN than in PABA. Figure 3.8 shows electron density difference plots for AN and PABA, with light areas representing regions of electron density gain and dark areas representing electron density loss.[19] In AN, it can be seen that charge is being transferred from the amino group to the ring, resulting in the 1.67 D increase in μ_a. The increase in μ_a (1.1 D) in PABA is smaller than this. The electron density difference plot of PABA shows that the amino group donates electron density to the ring, as it does in AN, and that the carboxyl group also donates electron density to the ring. The donation made by the amino group increases μ_a relative to the ground state because it occurs in the same direction as the ground-state dipole. However, the donation of charge from the carboxyl group to the ring in PABA occurs in the opposite direction. Thus, the μ_a component still increases in PABA upon excitation, but the magnitude of the increase is less, relative to AN, due to the counteracting effect of the carboxyl group.

Table 3.3. Comparison of experimental dipole moment values of PABA and AN.

	PABA	Aniline[9,15]
S_0		
μ_a (D)	3.12 (8)	1.129 (5)
μ_b (D)	1.2 (2)	0.00 (1)
μ_c (D)	0.00 (1)	0.00 (1)
μ (D)	3.3 (2)	1.129 (5)
S_1		
$\Delta\mu_a$ (D)	1.1 (2)	1.67 (1)
$\Delta\mu_b$ (D)	0.1 (4)	0.00 (1)
$\Delta\mu_c$ (D)	0.00 (2)	0.00 (1)
$\Delta\mu$ (D)	1.1 (3)	1.672 (7)
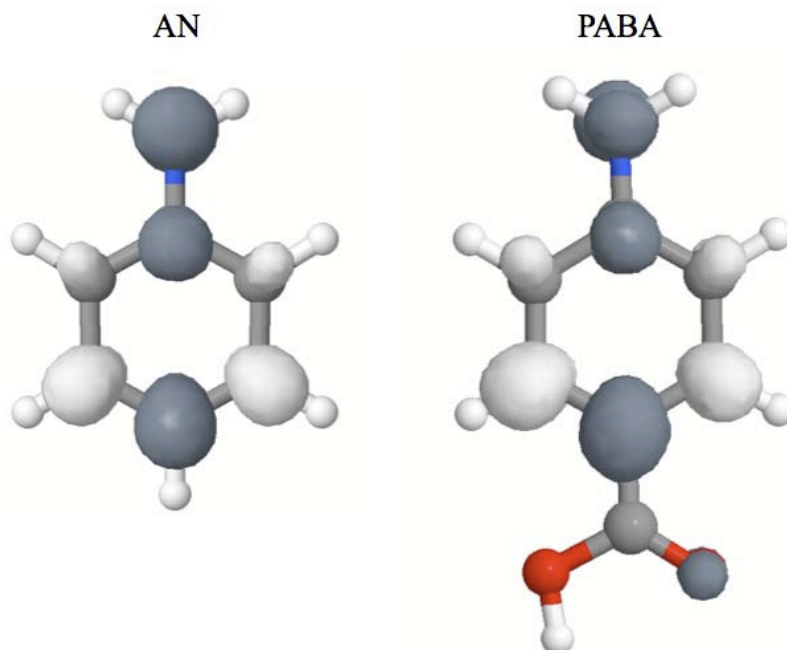
Figure 3.8. Electron density difference plots for AN and PABA. Light areas represent regions of electron gain, and dark areas represent regions of electron loss.

3.6   CONCLUSIONS

Rotationally resolved electronic spectroscopy has been performed in the presence of an electric field to determine the permanent electric dipole moment values for PABA in the gas phase in both its ground and excited states. The value of μ_a in the S_0 state is in reasonable agreement with electric deflection measurements made by Dugourd, *et al.*[5] The dipole moments of PABA have also been compared to those of AN. The addition of the carboxyl group withdraws electron density from the ring, resulting in an overall ground state dipole moment that is larger than that of AN. There is also a significant μ_b component to the dipole in PABA; this indicates that there is a considerable electron density difference between the =O and –OH groups of the carboxyl. The change in μ_a of PABA upon excitation is slightly smaller in magnitude compared to that of AN, and the percent change is much smaller. Calculations suggest that both the amino and carboxyl substituents transfer some electron density back to the ring upon excitation. Because the donation of electron density from the carboxyl group occurs in a direction opposite to the dipole moment, the effect of the donation from the amino group is mitigated, resulting in a smaller change in μ_a than in AN.

3.7   ACKNOWLEDGEMENTS

3.8   REFERENCES AND NOTES

1. J. A. Reese, T. V. Nguyen, T. M. Korter and D. W. Pratt, *J. Am. Chem. Soc.* **126**, 11387 (2004).

2. T. V. Nguyen and D. W. Pratt, *J. Chem. Phys.* **124**, 054317 (2006).

3. R. Antoine, I. Compagnon, D. Rayane, M. Broyer, Ph. Dugourd, G. Breaux, F. C. Hagemeister, D. Pippen, R. R. Hudgins and M. F. Jarrold, *J. Am. Chem. Soc.* **124**, 6737 (2002).

4. Ph. Dugourd, R. Antoine, G. Breaux, M. Broyer and M. F. Jarrold, *J. Am. Chem. Soc.* **127**, 4675 (2005).

5. I. Compagnon, R. Antoine, D. Rayane, M. Broyer and Ph. Dugourd, *J. Phys. Chem. A.* **107**, 3036 (2003).

6. G. Meijer, M. S. de Vries, H. E. Hunziker, and H. R. Wendt, *J. Chem. Phys.* **92**, 7625 (1990).

7. I. Compagnon, R. Antoine, D. Rayane, M. Broyer and Ph. Dugourd, *Phys. Rev. Lett.* **89**, 253001 (2002).

8. M. Abd El Rahim, R. Antoine, L. Arnaud, M. Broyer, D. Rayane, A. Viard and Ph. Dugourd, *Eur. Phys. J. D.* **34**, 15 (2005).

9. T. M. Korter, D. R. Borst, C. J. Butler and D. W. Pratt, *J. Am. Chem. Soc.* **123**, 96 (2001).

10. W. A. Majewski, J. F. Pfanstiel, D. F. Plusquellic and D. W. Pratt, in *Laser Techniques in Chemistry.* T. R. Rizzo and A. B. Meyers, Eds. J. Wiley & Sons: New York (1995); p. 101.

11. D. F. Plusquellic, R. D. Suenram, B. Maté, J. O. Jensen and A. C. Samuels, *J. Chem. Phys.* **115**, 3057 (2001).

12. J. M. Bello and R. J. Hurtubise, *Appl. Spectrosc.* **42**, 619 (1988).

13. M. J. Frisch, *et al. Gaussian 03*, Revision 6.0. Gaussian, Inc.: Wallingford, CT (2004).

14. M. Abd El Rahim, R. Antoine, M. Broyer, D. Rayane and Ph. Dugourd, *J. Phys. Chem. A.* **109**, 8507 (2005).

15. D. G. Lister, J. K. Tyler, J. H. Høg and N. W. Larsen, *J. Mol. Struct.* **23**, 253 (1974).

16. J. M. Hollas, M. R. Howson, T. Ridley, and L. Halonen, *Chem. Phys. Lett.* **98**, 611 (1983).

17. R. T. Kroemer, K. R. Liedl, J. A. Dickinson, E. G. Robertson, J. P. Simons, D. R. Borst and D. W. Pratt, *J. Am. Chem. Soc*. **120**, 12573 (1998).

18. E. P. Hunter and S. G. Lias, *J. Phys. Chem. Ref. Data.* **27**, 413 (1998).

19. These plots were created by taking ($\phi_4^2 - \phi_3^2$) for aniline and ($\phi_5^2 - \phi_3^2$) for PABA (since the calculated LUMO and LUMO+1 are reversed).   Ideally, each plot would have been generated from a normalized linear combination of the HOMO to LUMO and the HOMO-1 to LUMO+1 excitations. However, since the orbital ordering was reversed for PABA, we could not rely on the calculated coefficients.

4.0   ON THE ELECTRIC DIPOLE MOMENTS OF ASYMMETRIC TOPS. MEASUREMENT BY HIGH RESOLUTION ELECTRONIC SPECTROSCOPY IN THE GAS PHASE.

4.1   ABSTRACT

Reported here are Stark-effect measurements of the permanent electric dipole moments of two structural isomers of aminobenzonitrile, 2ABN and 3ABN, using high resolution laser molecular beam techniques. When combined with previous results on 4ABN, the data show that each structural isomer has a unique dipole moment, in both its ground (S_0) and electronically excited (S_1) states, thereby providing a means of distinguishing them. Possible applications of the method to other, biologically relevant molecules are discussed.

4.2   INTRODUCTION

The "molecular design of life"[1] is significantly influenced by the properties of isolated molecules. Thus, the three-dimensional structures and functions of proteins depend upon the size, shape, and charge distributions of the side chains in the 20 different amino acid building blocks that are used to construct them. Protein-protein interactions, leading to aggregation and disease, are also believed by some to be influenced by the dipole moments of their components parts.[2] It is thus a bit surprising that the dipole moments of the individual amino acids, and their dependence on the conformation of the isolated molecule, remain largely unexplored by experimental techniques.

Significant progress towards achieving this goal has been made, beginning with the work of Brown and co-workers on glycine, histamine, alanine, and related molecules a number of years ago.[3] More recently, several neutral aliphatic amino acids in the gas phase have been studied using laser ablation, molecular beam Fourier transform microwave spectroscopy,[4] and

34

their preferred structures determined by measurements of their rotational and ^{14}N quadrupole coupling constants. Mons and co-workers,[5] and others, have probed the structures of small peptides using IR/UV double resonance techniques. But the dipole moments of many of these species have yet to be reported. Compagnon *et al.*[6] have coupled a matrix assisted laser desorption source to an electric beam deflection setup to measure the permanent electric dipole of tryptophan isolated in a molecular beam. More recently, this method has been applied to a variety of species, including glycine-based[7] and alanine-based peptides.[8] In the latter work, the authors concluded that alanine-based peptides formed β-sheets in the gas phase, rather than the α-helices normally observed in aqueous solution, because the observed dipole moments were much smaller than expected.

One possible explanation for this anomaly, offered first by Abd El Rahim, *et al.*[9], is that the gas-phase alanine-based peptides are actually helical in shape, and that deviations from their expected deflection behavior were a consequence of the asymmetry of the molecule. This idea was tested, and it was indeed found that, in a family of aminobenzonitrile (ABN) molecules, there were increasing deviations from the calculated Stark-effect behavior with increasing asymmetry in the series 4ABN, 3ABN, and 2ABN, shown below in Scheme 4.1.

4ABN   3ABN   2ABN
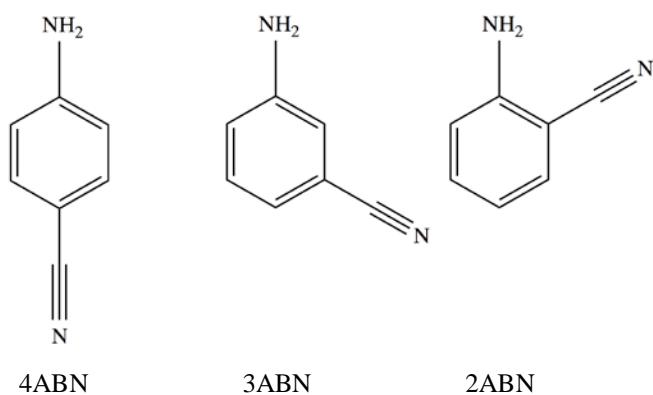
Scheme 4.1

Described herein are the results of Stark-effect experiments by high-resolution laser spectroscopy on two of these molecules, 2ABN and 3ABN. (Similar results for 4ABN have previously been reported.[10]) The objectives of this work were (a) to show that the permanent electric dipole moments of these species could, in fact, be measured, (b) to compare the measured values with *ab initio* values upon which the calculations of Abd El Rahim, *et al.*[9] were based, and therefore, (c) to validate (or invalidate) their explanation of the observed deflection behavior. We find that this explanation is correct, a fact that was anticipated by others.[11] But we also show, as a consequence, that the method described here (as well as related microwave methods) can still be relied upon for future measurements of the dipole moments of the "building blocks of life".[1]

4.3   EXPERIMENTAL

2ABN (98% purity) and 3ABN (99% purity) were purchased from Sigma-Aldrich and used as received. Vibrationally resolved fluorescence excitation spectra (FES) were obtained by heating the sample to ~ 40 ºC, seeding the resulting vapor into 2-2.5 kTorr of dry helium gas (> 90% purity), and expanding the mixture through a 1 mm diameter orifice pulsed valve (General Valve Series 9, operating at 10 Hz) into a vacuum chamber (10^{-5} Torr). The cooled sample was then crossed 2 cm downstream of the nozzle with the output of a Quanta Ray Nd^{3+}: YAG (Model DCR-1A) pumped dye laser (Model PDL-1). DCM dye was used to obtain the correct visible laser frequency; this was then doubled externally with a potassium dihydrogen phosphate (KDP) crystal. Any remaining visible light was filtered, leaving ultraviolet (UV) light with a spectral resolution of ~ 1 cm^{-1}. Fluorescence was collected with a photomultiplier tube (EMI 98139B)

positioned at right angles to both the laser and nozzle beams. The data was processed by a boxcar integrator (Stanford Research Systems) and recorded using Quick Data Acquisition software (Version 1.0.5).

The molecular beam laser spectrometer used to obtain rotationally resolved spectra has been described elsewhere.[12] Briefly, the samples were each heated to ~ 120 ºC, seeded in dry argon gas (> 99% purity), and expanded into a vacuum through a 240 µm quartz nozzle. The molecular beam was formed by skimming the expansion 2 cm downstream of the nozzle with a 1 mm diameter skimmer, and then crossed 15 cm downstream with the frequency-doubled output of a modified continuous ring dye laser. DCM dye was used for 2ABN, and DCM Special dye was used for 3ABN. The visible output of the dye laser was externally frequency-doubled by a Spectra-Physics Wavetrain using a 630 nm LBO crystal; ~ 400 µW and ~ 200 µW of UV light was produced at the 2ABN and 3ABN origin frequencies, respectively. Fluorescence was collected using spatially selective optics and detected by a photomultiplier tube (EMI 9813 QB) and photon counting system. All information was processed using the jba95 data acquisition system.[13] Absolute transition frequencies in the excitation spectrum were determined by comparison to the I_2 absorption spectrum (accuracy ~ 30 MHz), which was recorded simultaneously with the high resolution spectrum. Frequency markers also were collected; these were generated by passing a small portion of the fundamental through a stabilized etalon with a free spectral range of 299.7520 ± 0.0005 MHz. Fitting of the zero-field spectra was performed using the jb95 rotational least-squares fitting program.[14] The experimental set-up of the Stark cell and the procedure for analyses of Stark spectra have been described in detail elsewhere;[15] applied field strengths ranged from ~ 95 to 1900 V/cm.

4.4   RESULTS

Vibrationally resolved FES of 2ABN and 3ABN are shown in Fig. 4.1. Both spectra are consistent with previously published data on the two molecules.[16,17] In comparison to the FES of 4-aminobenzonitrile (4ABN),[17] the spectra of 2ABN and 3ABN show more vibrational activity. 4ABN contains a symmetry plane and is a near symmetric top molecule ($\kappa = -0.94$); 2ABN and 3ABN, to varying degrees, are less symmetric, allowing more transitions to be observed.

The rotationally resolved FES of the origin band of 2ABN at zero field is shown in Figure 4.2a. The band shows 44/55 a/b hybrid character,[18] with the transition moment lying between the a and b axes. Rotational constants obtained by ab $initio$ calculations,[19] shown in Table 4.1, were used to create an initial simulation. Transitions were assigned and the rotational constants were adjusted until the simulation was in good agreement with the experimental spectrum. The parameters obtained from this fit are given in Table 4.1. A portion of the simulation is shown in the lower part of Fig. 4.2a, demonstrating its good agreement with experiment. Each line of the simulation represents an individual $|J'K_a'K_c'> \leftarrow |J''K_a''K_c''>$ transition; 101 transitions were assigned. Width has been added to reproduce the overall shape of the experimental spectrum. The best fit had an OMC (observed minus calculated standard deviation) of 1.9 MHz. The measured rotational constants are in good agreement with theoretical ones, with differences of less than 1% for the ground state and less than 2% for the excited state.

Figure 4.2b shows the corresponding rotationally resolved FES of the origin band of 3ABN at zero field. An initial simulation was created using the ab $initio$ values given in Table 4.1, and transitions were assigned and the rotational constants were adjusted until the simulation
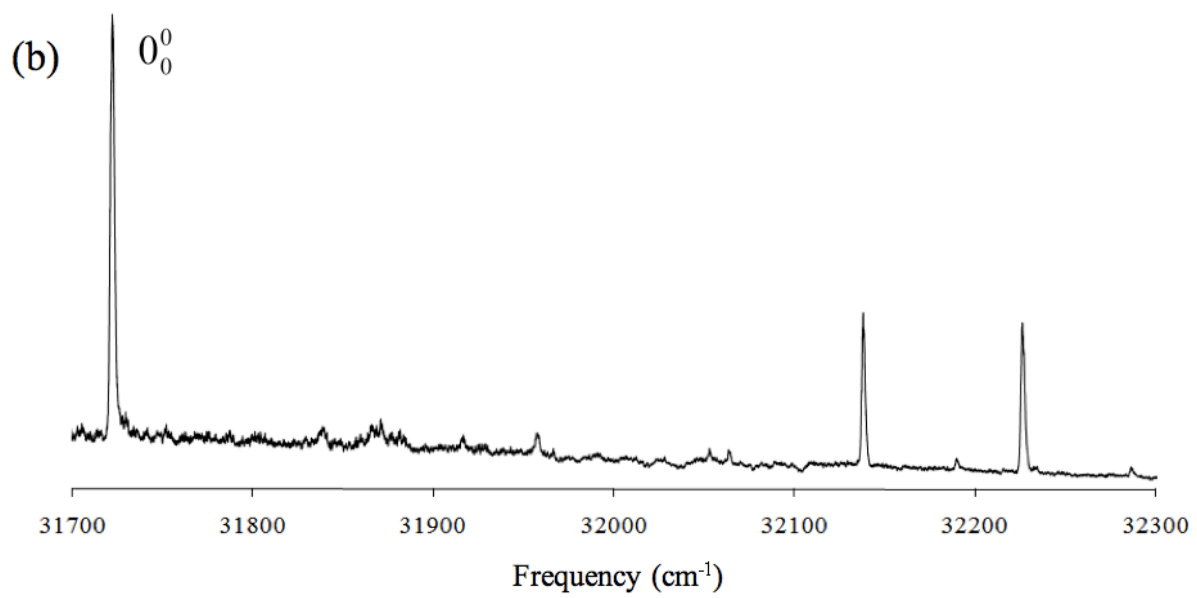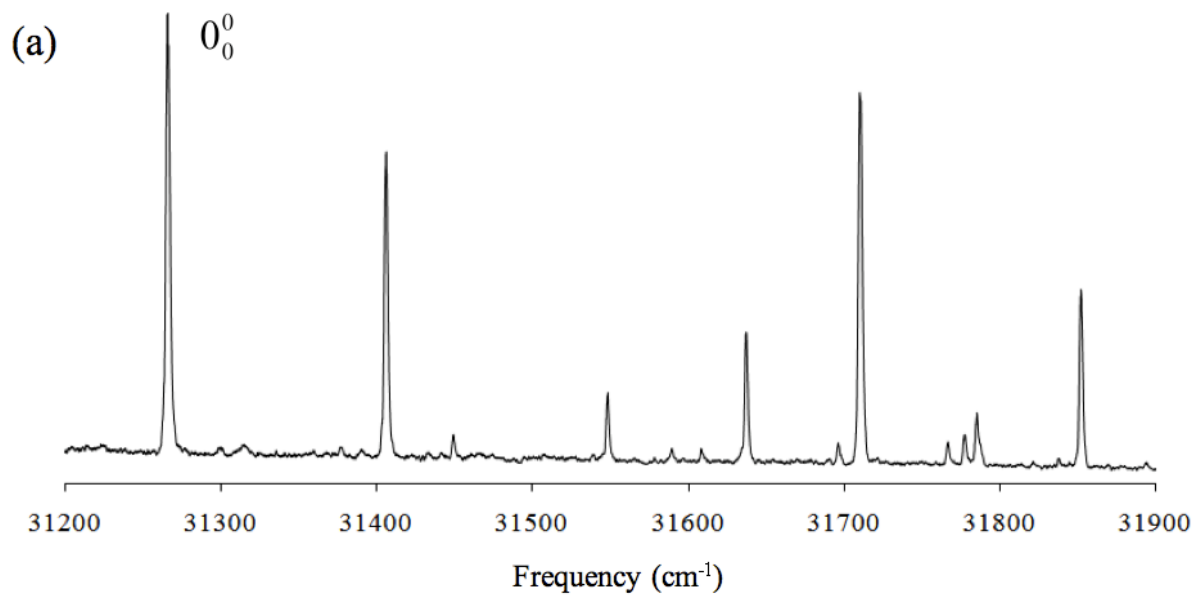
Figure 4.1. Vibrationally resolved fluorescence excitation spectra of 2ABN (a) and 3ABN (b).
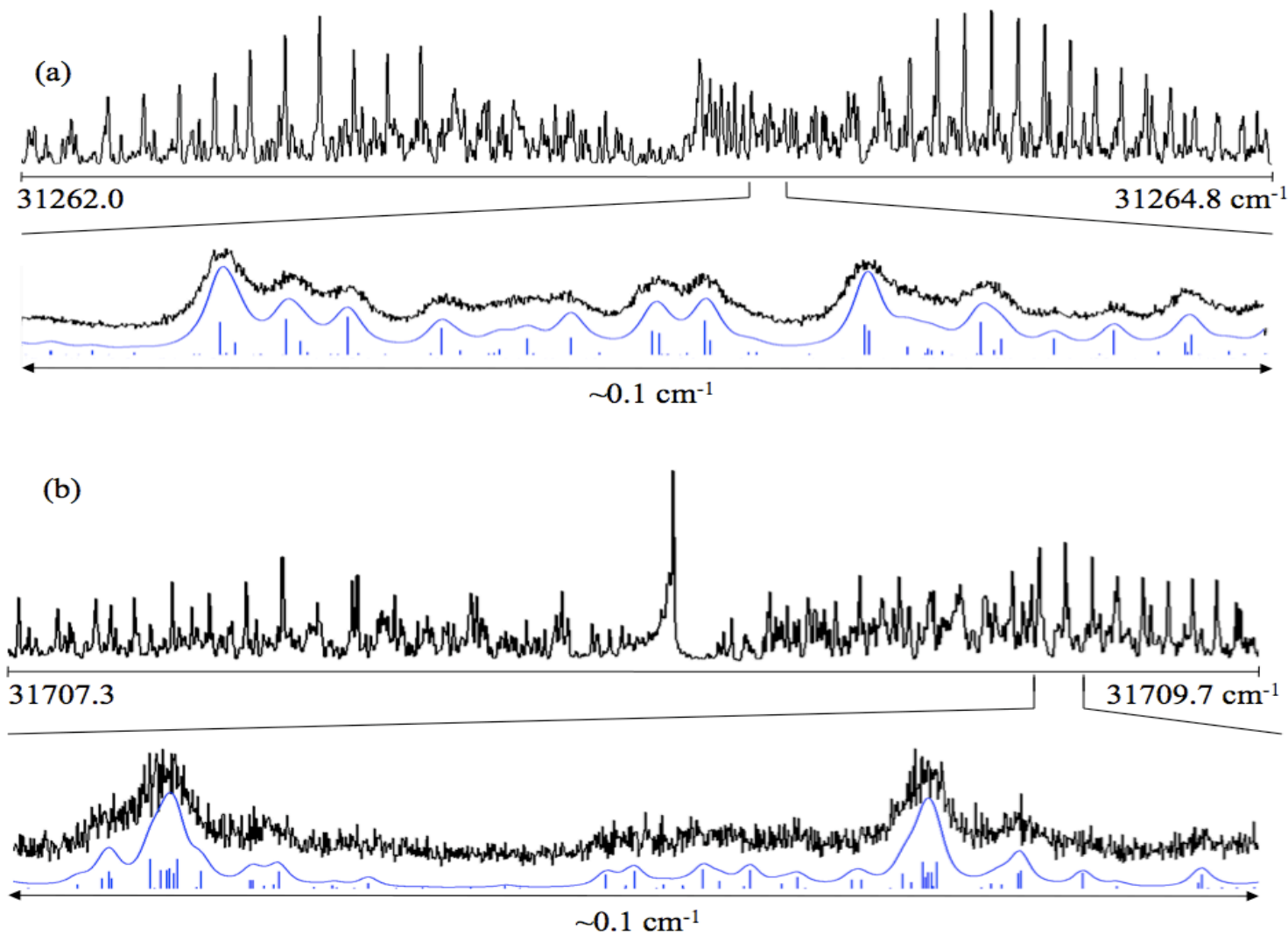
Figure 4.2. (a) Field-free origin band spectrum of 2ABN, occurring at 31263.5 cm^{-1}. The bottom panel shows a comparison of a small portion of the experimental spectrum (black trace) with two simulated spectra (blue trace), with and without a convoluted lineshape function. (b) Field-free origin band spectrum of 3ABN, occurring at 31708.6 cm^{-1}. The bottom panel shows a comparison of a small portion of the experimental spectrum (black trace) with two simulated spectra (blue trace), with and without a convoluted lineshape function.

Table 4.1. Experimental inertial parameters of 2ABN and 3ABN. Theoretical values calculated using the MP2/6-31G** and CIS/6-31G** methods also have been included for comparison.

	2ABN			3ABN		
	Experiment	**Theory**	**Error (%)**	**Experiment**	**Theory**	**Error (%)**
S_0						
A (MHz)	3009.0 (1)	2992.5	0.5	3372.7 (1)	3366.3	0.2
B (MHz)	1509.0 (1)	1499.1	0.6	1209.9 (1)	1201.1	0.7
C (MHz)	1005.2 (1)	999.8	0.5	890.8 (1)	886.0	0.5
ΔI (amu Å^2)	-0.10	-0.52		-0.22	-0.50	
S_1						
A (MHz)	3093.8 (2)	3085.6	0.3	3373.6 (1)	3435.1	1.8
B (MHz)	1464.4 (1)	1488.1	1.6	1189.4 (1)	1201.0	1.0
C (MHz)	994.1 (1)	1003.9	1.0	879.5 (1)	890.0	1.2
ΔI (amu Å^2)	-0.08	0.02		-0.08	-0.10	
$a/b/c$	45/55/0			25/75/0		
Origin (cm^{-1})	31263.5			31708.6		

was in good agreement with the experimental spectrum. A portion of the best-fit simulation, with and without added linewidth, is shown in the lower portion of Fig. 4.2b. Over 100 transitions were assigned; the best fit had an OMC of 4.6 MHz. The measured rotational constants are shown in Table 4.1, and they are again in good agreement with calculations, with differences of less than 1% for the ground state and less than 2% for the excited state. Fits of the spectral line intensities are consistent with a band having 25/75 *a/b* hybrid character. This is substantially different from the band character seen for 2ABN.

Figure 4.3 shows the spectrum of 2ABN in the presence of an electric field of 950 V/cm. To simulate the behavior of the spectrum in the presence of an applied electric field, a special program[15] was used, in conjunction with jb95. This program carries out exact diagonalizations of truncated matrices and uses the following Hamiltonian:

$$\hat{H} = \hat{H}_r + \hat{H}_e \tag{4.1}$$

The first term, $\hat{H}_r$, is the rigid-rotor Hamiltonian,

$$\hat{H}_r = AJ_a^2 + BJ_b^2 + CJ_c^2 \tag{4.2}$$

and $\hat{H}_e$ is the Stark Hamiltonian,

$$\hat{H}_e = -E_Z \sum_{g=a,b,c} \mu_g \phi_{Z_g} \tag{4.3}$$

Here, *A*, *B* and *C* are the rotational constants, J_a, J_b and J_c are the projections of the angular momentum on the *a*, *b* and *c* inertial axes, E_Z represents the electric field applied along the *Z* axis, μ_a, μ_b and μ_c are the dipole moment components along each inertial axis, and ϕ represents the direction cosines relating the lab and molecular frames. Other details have been described previously.[15] Application of an electric field causes transitions observed in the field-free

spectrum to split and shift in frequency, as is apparent from Eq. 4.3. The magnitudes of these

shifts depend on both the field strength and dipole moment values.
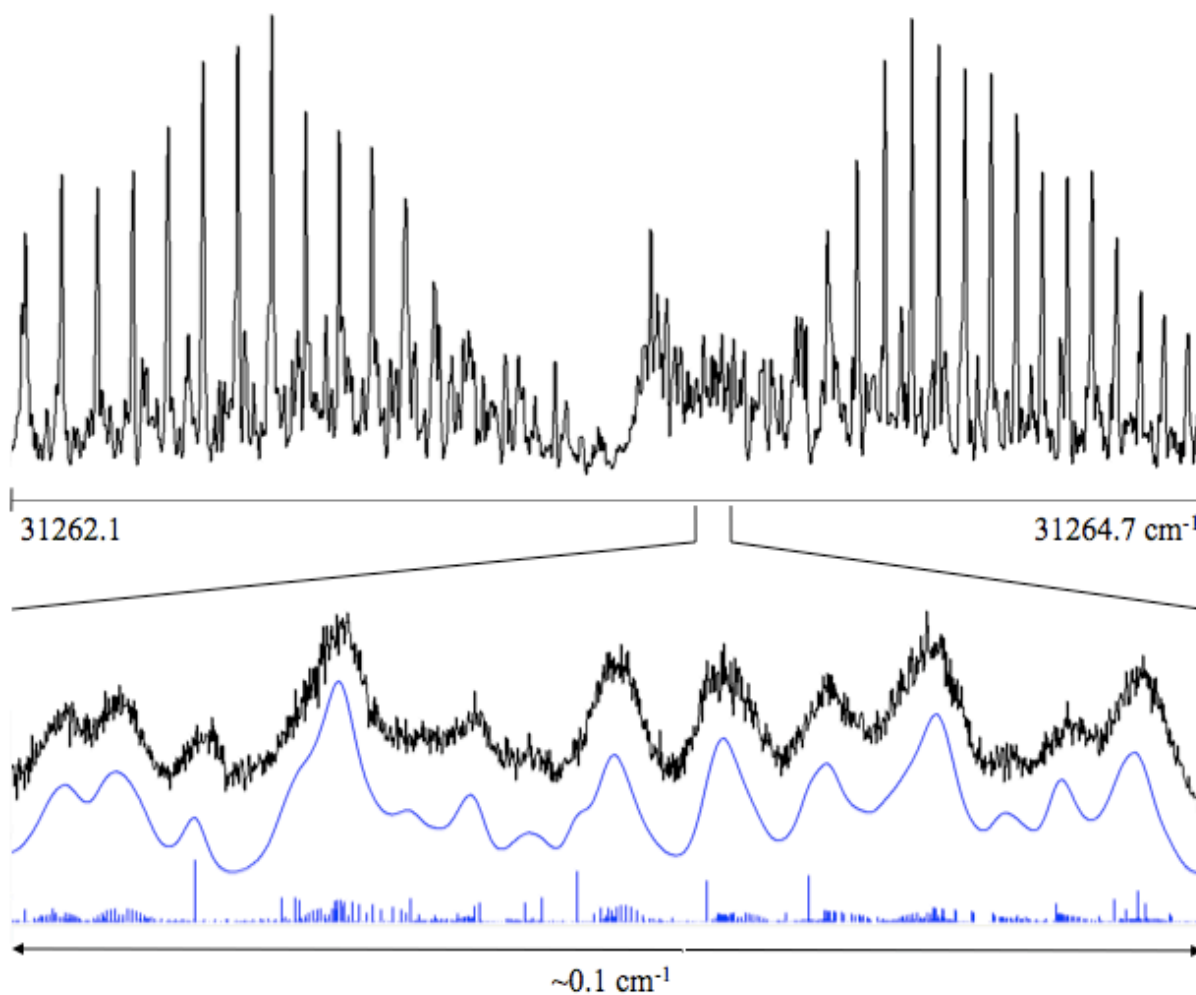
Figure 4.3. Origin band spectrum of 2ABN, in presence of an electric field of 950 V/cm. The top panel shows the entire spectrum, and the bottom panel shows a comparison of a portion of the experimental spectrum (black trace) with two simulated spectra (blue trace), with and without a convoluted lineshape function.

By tracking the shifts of the spectral transitions in the presence of the external electric field, values of the dipole moment components of 2ABN were determined for both the ground and excited states. First, μ_a, μ_b and μ_c were estimated using *ab initio* methods, and an initial simulation of the overall spectrum was created. The components were then varied until the simulation resembled the experimental spectrum. Next, lines were assigned, paying particular attention to those transitions that were most sensitive to the dipole moment components. The positions of P- and R-branch lines with high K values, particularly those equal or nearly equal to J, are especially sensitive to μ_a; the positions of the lines with $K_a = 0$ are especially sensitive to μ_c; and the positions of Q-branch lines are sensitive to all three dipole moment components, especially μ_b. The assigned transitions were then fit and used to create a new simulation, and the process was iterated until the simulation was in good agreement with the experiment. An example of the fit for 2ABN is shown in the lower portion of Fig. 4.3. Typical OMC values of these fits are ~6 MHz, substantially less than the linewidth.

Spectra of 3ABN taken with an applied electric field were fit in a manner similar to those of 2ABN, see Figure 4.4. Relative to 2ABN, the spectra of 3ABN were somewhat noisier, and the fits were characterized by slightly larger OMC values (12 MHz or less). Still, it proved possible to extract relatively precise values of μ in both electric states of each molecule based on fits of their Stark spectra at five different field strengths.

Table 4.2 lists the derived values of μ that were obtained in this work. We note here that $\Delta\mu = \mu(S_1) - \mu(S_0)$ is relatively large for 3ABN and relatively small for 2ABN. We also note that the agreement between theory and experiment is poor, for both molecules in both electronic states. Differences in the values of μ_c are anticipated (see below). But the remaining calculated dipole moment components differ from the measured ones by as much as 50%. Clearly,
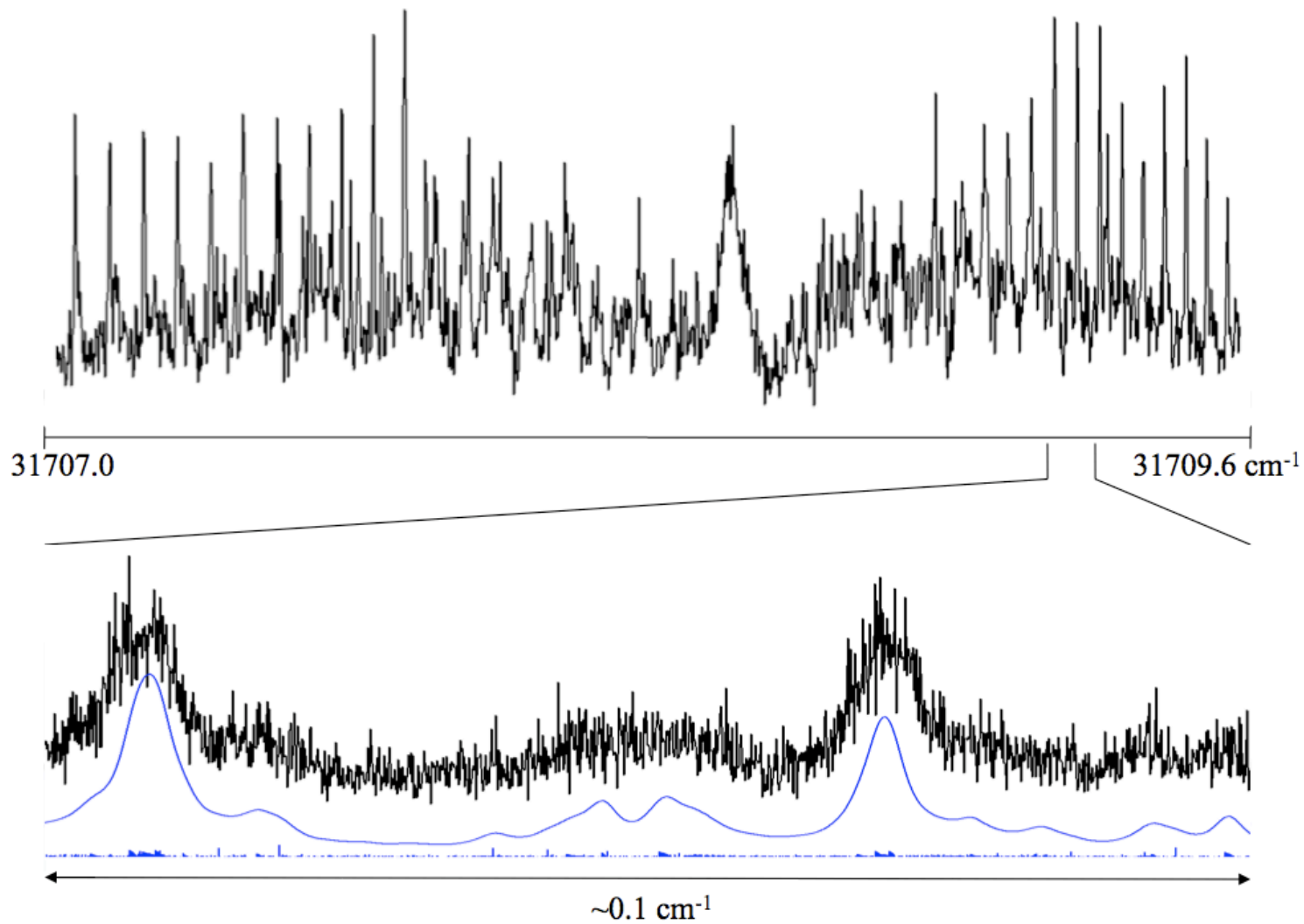
Figure 4.4. Origin band spectrum of 3ABN, in presence of an electric field of 950 V/cm. The top panel shows the entire spectrum, and the bottom panel shows a comparison of a portion the experimental spectrum (black trace) with two simulated spectra (blue trace), with and without a convoluted lineshape function.

31707.0

31709.6 cm^{-1}

~0.1 cm^{-1}

Table 4.2. Experimental dipole moment values of 2ABN and 3ABN. Theoretical values calculated using the MP2/6-31G** and CIS/6-31G** methods also have been included for comparison.

	2ABN			3ABN		
	Experiment	**Theory**	**Error (%)**	**Experiment**	**Theory**	**Error (%)**
S$_0$						
μ_a (D)	3.6 (1)	3.4	6	4.8 (3)	5.1	6
μ_b (D)	1.9 (2)	1.7	10	1.2 (4)	0.6	50
μ_c (D)	0.0 (1)	1.1	-	0.0 (1)	1.2	-
μ (D)	4.1 (2)	4.0	2	4.9 (4)	5.3	8
θ, a/b (°)	28	27		14	7	
S$_1$						
μ_a (D)	3.4 (2)	3.9	15	6.8 (3)	8.1	19
μ_b (D)	3.4 (2)	3.5	3	0.0 (4)	-0.4	-
μ_c (D)	0.0 (1)	0.0	0	0.0 (1)	0.0	0
μ (D)	4.8 (3)	5.2	8	6.8 (3)	8.1	19
θ, a/b (°)	45	42		0	3	

the calculation methods and basis sets used are inadequate to the task of predicting accurate values of the permanent electric dipole moments of isolated large molecules. (Abd el Rahim, *et al.* [9] have reported improved values using larger basis sets.) Despite this fact, the discrepancies between the measured and calculated values are too small to explain the "anomalous" electric deflection behavior of the three aminobenzonitriles.[9]

Both theory and experiment agree that the ABN's have pyramidal NH_2 groups, especially in their ground electronic states, necessitating non-zero values of μ_c. But this localized structure is just one well of the double minimum potential along this coordinate; the inverted structure has a value of μ_c which has the same magnitude but is opposite in sign. Ground state values of μ_c less than 0.1 D are required by our fits of the Stark behavior in ABNs. Since the calculated values are much larger than this (*cf.* Table 4.2), we conclude that motion along this coordinate is fast, compared to the frequency of rotational motion. A similar effect occurs in aniline, where the ground-state inversion barrier is on the order of 550 cm^{-1}.[15, 20, 21]

4.5   DISCUSSION

Both 2ABN and 3ABN consist of a benzene ring to which amino (-NH_2) and nitrile (-CN) substituents are attached. But the different relative placement of these substituents has several consequences for their spectra. Moving the amino group from the 2- to the 3- position changes the orientation of the inertial axes and, consequently, the group's placement relative to the axis system of the molecule. See Fig. 4.5. In 2ABN, the amino group lies closest to the *b*-axis, but in 3ABN, the amino group lies closest to the *a*-axis. The difference in the location

47
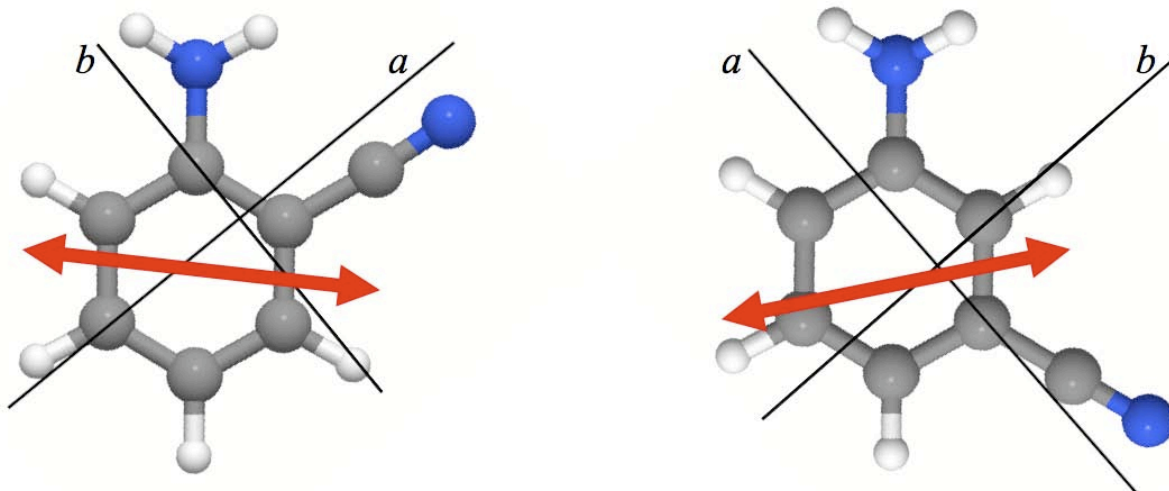
Figure 4.5. Structures of 2ABN and 3ABN with the *a* and *b* inertial axes shown for reference. The red arrows represent the predicted transition moment orientations.

of the axes is apparent on comparison of the ground state rotational constants, given in Table 4.1. In 2ABN, the substituents are on opposite sides of the *a*-axis, while in 3ABN the substituents are on **o**pposite sides of the *b*-axis. Therefore, 2ABN has the smaller value of *A*, whereas 3ABN has the smaller value of *B*. Overall, 2ABN has a more compact shape, resulting in a larger value of *C*.

The appearances of the fully resolved electronic spectra of 2ABN and 3ABN also are quite different (Figure 4.3). The spectrum of 2ABN (45/55, *a/b*) has much more *a*-character than that of 3ABN (25/75, *a/b*); their transition moment (TM) orientations must be very different. Thus, it is possible that the electronic structures of the two molecules are quite different. Alternatively, it may be that these differences are more simply explained by differences in the orientations of their respective inertial axes.
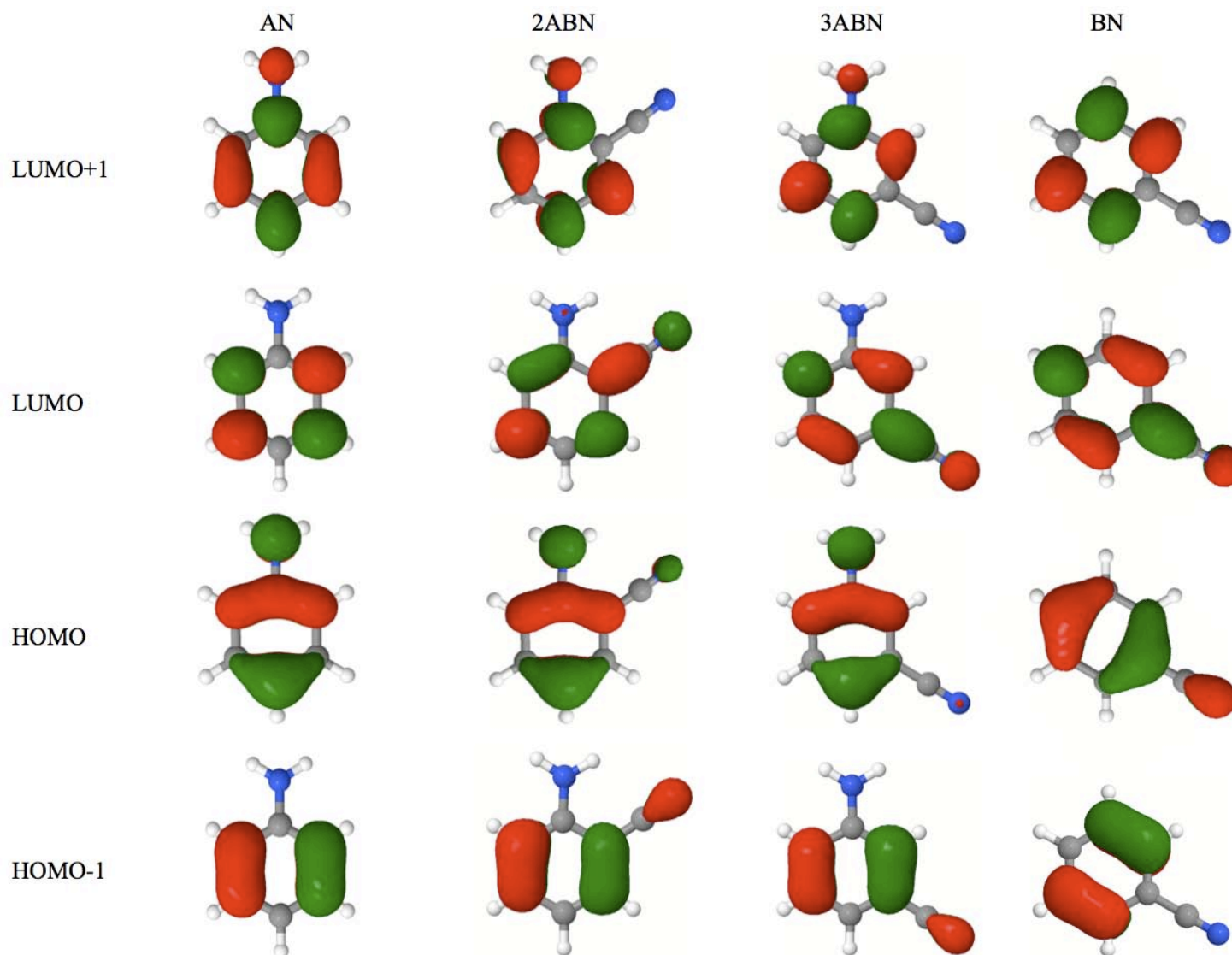
Figure 4.6. HOMO-1 (ϕ_2), HOMO (ϕ_3) , LUMO (ϕ_4) , and LUMO-1 (ϕ_5) molecular orbitals of AN, 2ABN, 3ABN, and BN as predicted by HF/6-31G** calculations.

HF/6-31G** calculations[19] were performed to address this issue. Figure 4.6 summarizes the results for aniline (AN), benzonitrile (BN), and the two aminobenzonitriles, 2ABN and 3ABN. Comparisons of the molecular orbitals (MO's) of the four molecules show that the highest occupied molecular orbital (HOMO) and HOMO-1 of 2ABN and 3ABN are very similar to those of AN. (There is some delocalization of charge onto the –CN substituent in the ABNs). Their lowest unoccupied molecular orbital (LUMO) and LUMO+1 are similar to those of both AN and BN, but bear a closer resemblance to those of BN. Both AN and BN display b-type spectra.[9,14] In CIS/6-31G** calculations, the S_1 state of AN is represented by the linear combination $\Psi(S_1) = 0.28\ (\phi_2\phi_5) + 0.64\ (\phi_3\phi_4)$, whereas the S_1 state of BN is represented by the linear combination $\Psi(S_1) = 0.55\ (\phi_2\phi_4) + 0.41\ (\phi_3\phi_5)$. Similar calculations for the two ABN's yield the results $\Psi(S_1) = 0.19\ (\phi_2\phi_5) + 0.67\ (\phi_3\phi_4)$ for 2ABN and $\Psi(S_1) = 0.21\ (\phi_2\phi_5) + 0.66\ (\phi_3\phi_4)$ for 3ABN. Thus, the –NH$_2$ group dominates in both cases; the S_1-S_0 TM's take up orientations that are perpendicular to the amino group, and these orientations differ between the two molecules because of the difference in the orientations of their inertial axes. See Figure 4.5. Thus, the electronic structures of both 2ABN and 3ABN are very similar, when viewed in this way.

Permanent dipole moments are more sensitive measures of the charge distributions in the two molecules and how these change when the photon is absorbed. Parts a and b of Figure 4.7 give visual images of these changes. (It should be noted that we do not obtain the direction of the dipole components from our fits; the directions shown in the figure are based on chemical intuition and the results of *ab initio* calculations.) Amino groups and cyano groups attached to an aromatic ring are electron donating and electron withdrawing, respectively. Thus, to a first
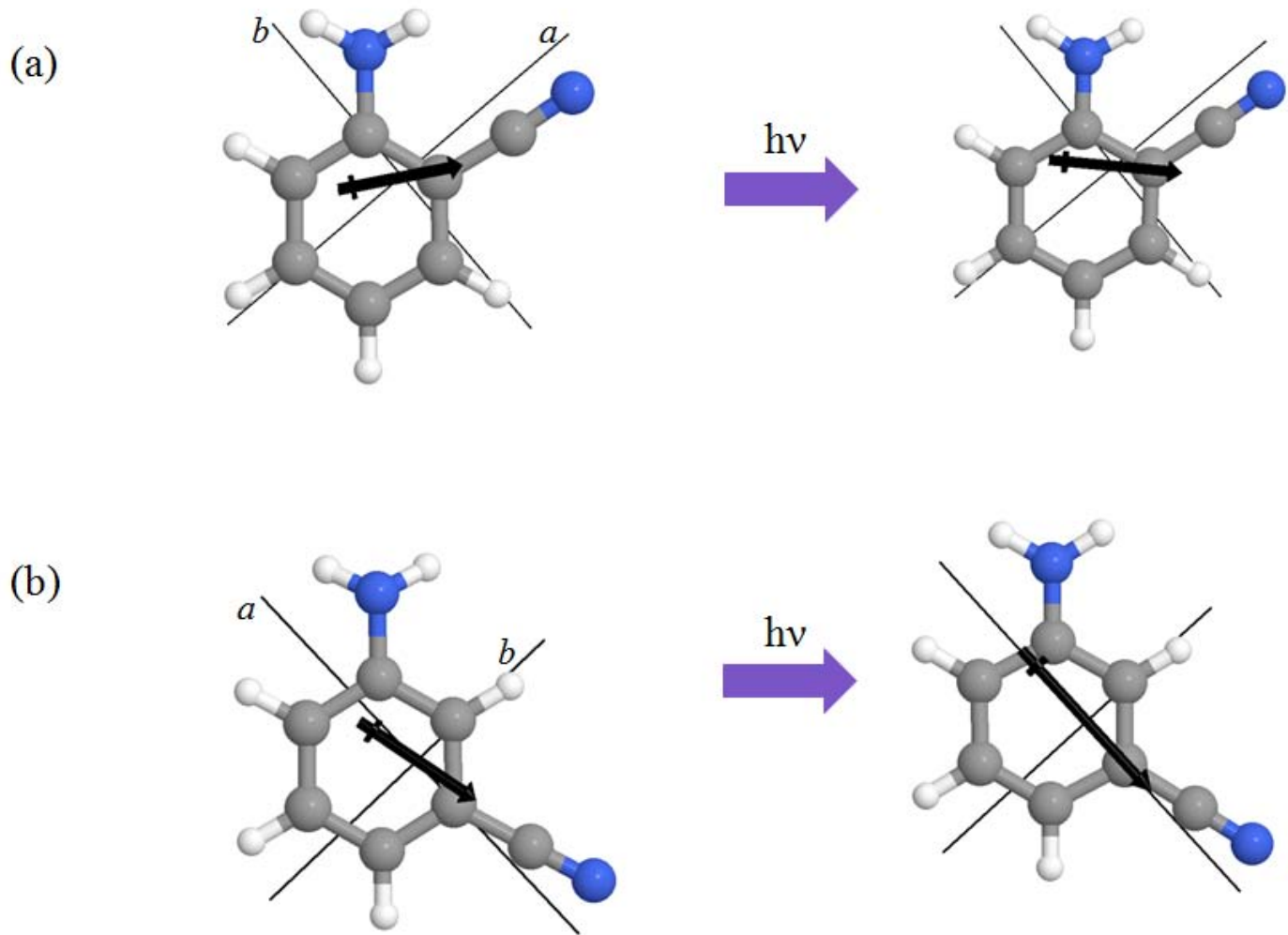
Figure 4.7. Measured dipole moments are shown on the structures of 2ABN (a) and 3ABN (b) in both the ground and excited electronic states.

Table 4.3. Predicted and measured dipole moments of 2ABN and 3ABN, compared to the previously measured values for AN, BN, and 4ABN, based on the vector addition model.

	AN[16]	BN[10]	2ABN		3ABN		4ABN[10]	
			Predicted	**Measured**	**Predicted**	**Measured**	**Predicted**	**Measured**
S_0								
μ_a (D)	1.13	4.48	3.7	3.6 (1)	5.1	4.8 (3)	5.61	6.41 (3)
μ_b (D)	0.00	0.00	1.6	1.9 (2)	0.7	1.2 (4)	0.00	0.00
μ (D)	1.13	4.48	4.0	4.1 (2)	5.1	4.9 (4)	5.61	6.41 (3)
S_1								
μ_a (D)	2.80	4.57	2.6	3.4 (2)	6.5	6.8 (3)	7.37	7.20 (3)
μ_b (D)	0.00	0.00	2.6	3.4 (2)	-0.6	0.0 (4)	0.00	0.00
μ (D)	2.80	4.57	3.7	4.8 (3)	6.5	6.8 (3)	7.37	7.20 (3)

approximation, the measured dipole moments of the two ABN's would be expected to be equal to the vector sums of the two substituent dipoles, -NH_2 and –CN, at least in the ground electronic state. This prediction was tested by forming the vector sums of the two dipoles using the measured dipole moments of AN[15] and BN[10] and the *ab initio* geometries of the two ABN's; the results are shown in Table 4.3. 2ABN has a predicted dipole moment of 4.0 D, compared to the measured value of 4.1 D; the resultant dipole vector makes a smaller angle with *a* than with *b* ($\mu_a/\mu_b \sim 1.9$). 3ABN has a predicted dipole moment of 5.1 D compared to the measured value of 4.9 D; the resultant dipole vector makes an even smaller angle with *a* than with *b* ($\mu_a/\mu_b \sim 4$). Thus, to a reasonable approximation, the dipole moments of 2ABN and 3ABN are the vector sums of the two component dipoles, in the ground electronic state. A similar conclusion has been reached for 4ABN. [10]

Excitation of both molecules to their S_1 states leads to large increases in both the magnitudes and orientations of their dipole moment vectors. In 2ABN, the increase in the magnitude of μ (4.8 D in the S_1 state) is caused by large increase in μ_b and a small decrease in μ_a, effects that are nicely captured by the vector addition model. The –NH_2 group is a stronger donor, and the –CN group is a stronger acceptor in the S_1 state. In 3ABN, owing to the aforementioned change in the inertial axes, the larger value of μ (6.8 D in the S_1 state) is caused by a large increase in μ_a and a small decrease in μ_b, again reflecting the stronger electron donor/acceptor character of the -NH_2/-CN groups. More striking is the change in orientation of the dipole moment vectors; these change by +/- 15° when the photon is absorbed. Large solvatochromic shifts of the fluorescence spectra of both molecules would be expected in the condensed phase.[22]

Deviations from the "additivity rule" are most pronounced for the S_0 state of 3ABN, where the predicted value is high, and for the S_1 state of 2ABN, where the predicted value is low. These effects may be traced to the MO's of the two molecules shown in Figure 4.6. As noted, while similar to the orbitals of AN and BN, the HOMO and HOMO-1 orbitals of the ABNs more closely resemble those of AN, whereas the LUMO and LUMO+1 orbitals bear a stronger resemblance to BN. Hence, it is reasonable that the dipole moment components are not strictly additive across the entire series of molecules.

Previous attempts to measure the permanent electric dipole moments of the three structural isomers of ABN by molecular beam deflection methods have led to ambiguous results.[9] Increasing deviations of the measured deflections compared to Stark-effect calculations were observed in the series 4ABN, 3ABN, and 2ABN. These deviations were attributed to the increasing asymmetry of the molecules across the series. To support this view, it was shown by first-principles calculations that the Stark-split energy levels of asymmetric tops begin to repel each other at high fields. These level repulsions lead to a mixing of rotational energy levels and a reduced energy shifting of the eigenvalues as the electric field is increased. That large molecules (whether asymmetric or not) excited to single ro-vibrational eigenstates are not deflected by an inhomogeneous electric field in a high density-of-states region was earlier established by the elegant infrared experiments of Fraser and Pate,[11] so the results of Abd El Rahim *et al.*[9] are not surprising.

Although the ABNs are certainly asymmetric (the κ values of 2ABN, 3ABN and 4ABN in their electronic ground state are -0.50, -0.74, and -0.94, respectively), their Stark-split energy levels are not dominated by avoided crossings at *low* field. This is shown explicitly for 2ABN in Figure 4.8. In fields up to 5 kV/cm, only three avoided crossings appear in the plots of state
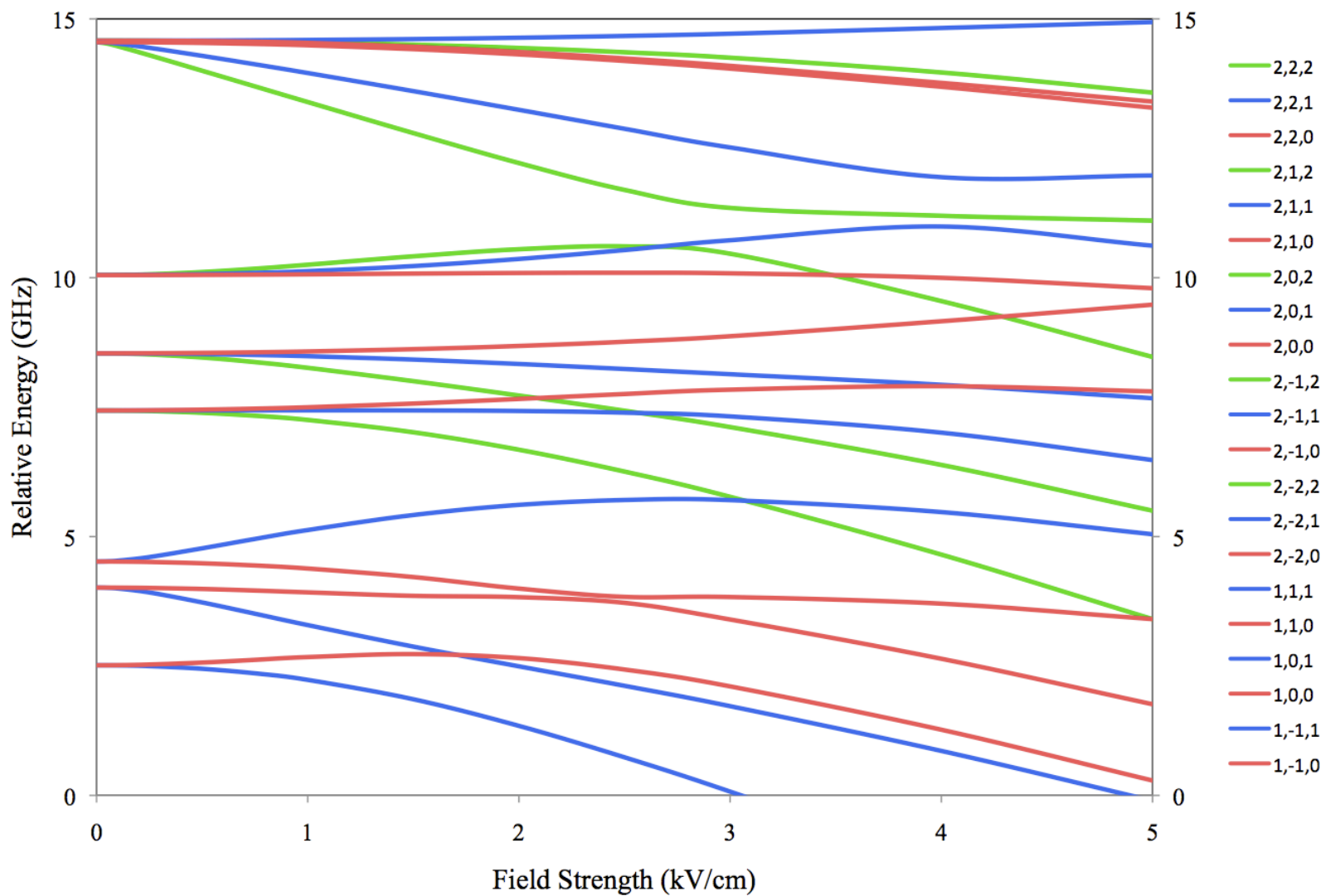
Figure 4.8. Stark-splitting energy level diagram for the ground state $J = 1$ and 2 rotational levels of 2ABN as a function of electric field. The simulation was run with the experimentally determined rotational constants and dipole moments.

energy versus field at low *J*. Even fewer appear at higher *J*, at low field strengths. Thus, the energy levels of both symmetric and asymmetric rotors are *regular*, not irregular, at low field strengths. Higher field strengths do lead to extensive level mixing, forming the basis for a number of creative applications, including studies of the dynamics of molecules in aligned rotational states ("pendular" states)[23] and the spatial separations of the structural isomers of neutral molecules according to their mass-to-dipole-moment ratios.[24] But, as the present application shows, lower field strengths are also useful. Selective excitation of the Stark-split spectra of large molecules leads to an unambiguous determination of the magnitude and orientation of their permanent dipole moments in different electronic states. Further experiments will exploit this fact in studies of the charge distributions of biologically relevant molecules in the gas phase, and how they are affected by the absorption of light.

4.6   ACKNOWLEDGEMENTS

4.7 REFERENCES AND NOTES

1. J. M. Berg, J. L. Tymoczko, and L. Stryer, *Biochemistry* (6th Ed.), W. H. Freeman and Co.: San Francisco (2006).

2. G. G. Tartaglia, A. Cavalli, R. Pellarin, and A. Caflisch, *Protein Sci.* **13**, 1939 (2004).

3. R. D. Brown, P.D. Godfrey, J. W. V. Stovey, and M. P. Bassez, *J. C. S. Chem. Comm.* 547 (1978); B. Vogelsanger, P. D. Godfrey, and R. D. Brown, *J. Am. Chem. Soc.* **113**, 7864 (1991); P. D. Godfrey, S. Firth, L. D. Hatherley, R. D. Brown, and A. P. Pierlot, *J. Am. Chem. Soc.* **115**, 9867 (1993).

4. See, for example, M. E. Sanz, A. Lesari, M. I. Peña, V. Vaquero, V. Cortijo, J. C. Lopez, and J. L. Alonso, *J. Am. Chem. Soc.* **128**, 3812 (2006).

5. See, for example, E. Gloaguen, F. Pagliarulo, V. Breuner, W. Chin, F. Piuzzi, B. Tardivel, and M. Mons, *Phys. Chem. Chem. Phys.* **9**, 4491 (2007).

6. I. Compagnon, F. C. Hagemeister, R. Antoine, D. Rayane, M. Broyer, P. Dugourd, R. R. Hudgins, and M. F. Jarrold, *J. Am. Chem. Soc.* **123**, 8440 (2001).

7. R. Antoine, I. Compagnon, D. Rayane, M. Broyer, P. Dugourd, G. Breaux, F. C. Hagemeister, D. Pippen, R. R. Hudgins, and M. F. Jarrold, *J. Am. Chem. Soc.* **124**, 6737 (2002).

8. P. Dugourd, R. Antoine, G. Breaux, M. Broyer, and M. F. Jarrold, *J. Am. Chem. Soc.* **127**, 4675 (2005).

9. M. Abd El Rahim, R. Antoine, M. Broyer, D. Rayane, and P. Dugourd, *J. Phys. Chem. A,* **109**, 8507 (2005).

10. D. R. Borst, T. M. Korter, and D. W. Pratt, *Chem. Phys. Letters*, **350**, 485 (2001).

11. G. T. Fraser and B. H. Pate, *J. Chem. Phys.* **100**, 6210 (1994), and references therein, especially R. G. J. Fraser, *Molecular Beams*, Methuen and Co: London (1937).

12. W. A. Majewski, J. F. Pfanstiel, D. F. Plusquellic and D. W. Pratt, in *Laser Techniques in Chemistry.* T. R. Rizzo and A. B. Meyers, Eds. J. Wiley & Sons: New York (1995); p. 101.

13. D. F. Plusquellic, Thesis, University of Pittsburgh (1992).

14. D. F. Plusquellic, R. D. Suenram, B. Maté, J. O. Jensen and A. C. Samuels, *J. Chem. Phys.* **115**, 3057 (2001).

15. T. M. Korter, D. R. Borst, C. J. Butler and D. W. Pratt, *J. Am. Chem. Soc.* **123**, 96 (2001).

16. P. Kolek, K. Pirowska and J. Najbar. *Phys. Chem. Chem. Phys.* **3**, 4874 (2001).

17. R. Howell, E. M. Joslin, A. G. Taylor and D. Phillips, *J. Chem. Soc, Faraday Trans.* **88**, 1605 (1992).

18. G. Herzberg, *Electronic Spectra of Polyatomic Molecules*, Van Nostrand: Princeton (1966).

19. M. J. Frisch, *et al. Gaussian 03*, Revision 6.0. Gaussian, Inc.: Wallingford, CT (2004).

20. A non-zero value of μ_c would also connect the even and odd symmetry levels of an inverting molecule, producing additional Stark shifts in the spectra (Ref. 22). However, given the anticipated large separation of these levels, and our experimental resolution, we consider this unlikely.

21. W. Gordy and R. L. Cook, *Microwave Molecular Spectra*, J. Wiley & Sons: New York (1984).

22. S. Jiang and D. H. Levy, *J. Phys. Chem. A,* **107**, 6785 (2003).

23. B. Friedrich and D. R. Herschbach, *Nature,* **353**, 412 (1991).

24. F. Filsinger, U. Erlekam, G. Von Helden, J. Kuepper, and G. Meijer, *Phys. Rev. Lett.* **100**, 13303 (2008).

5.0 HIGH RESOLUTION ELECTRONIC SPECTROSCOPY OF

9-FLUORENEMETHANOL IN THE GAS PHASE. NEW INSIGHTS INTO THE

PROPERTIES OF Π–HYDROGEN BONDS.

D. M. Miller, J. W. Young, P. J. Morgan, and D. W. Pratt

5.1   ABSTRACT

Rotationally resolved $S_1 \leftarrow S_0$ fluorescence excitation spectra of 9-fluorenemethanol (9FM) and deuterated 9-fluorenemethanol (9FMD) have been observed and assigned. Two conformers were detected, *sym*-9FM and *unsym*-9FM. The *sym* conformer has the –OH group symmetrically placed above the fluorene short axis, with its hydrogen atom pointing towards the top of an aromatic ring, whereas the *unsym* conformer has the –OH group tilted away from this axis, with its hydrogen atom pointing towards the side of an aromatic ring. Only the *sym* conformer shows a tunneling splitting associated with the torsional motion of the –OH group; the *unsym* conformer is "rigid." Additionally, a third subband was observed in the spectrum of *sym*-9FMD, evidencing secondary minima on the potential energy surfaces of the ground and excited electronic states. Studies of these surfaces along the –OH torsional coordinate provide new insights into the properties of π-hydrogen bonds.

5.2   INTRODUCTION

Many large organic molecules have been studied in a supersonic jet.[1] Often, these molecules possess one or more flexible side chains, resulting in the possibility of several conformations. What controls the preference of one conformation over another? It has been observed that weak interactions, such as π-hydrogen (π-H) bonding, can have a substantial influence. In the gas phase, the low energy conformers of benzyl alcohol, 2-phenethyl alcohol, and 2-indanol all exhibit a π-H bonding interaction.[2-8] As long as the attached side chain has the appropriate length, the most stable conformer of such molecules is the one in which the –OH

hydrogen atom is involved in an *intra*molecular hydrogen bond with the π-electrons of the aromatic ring.

9-Fluorenemethanol (9FM), having a –CH$_2$OH side chain and a large aromatic ring system, is another example of a molecule of this type (see Scheme 5.1). Owing to the weak
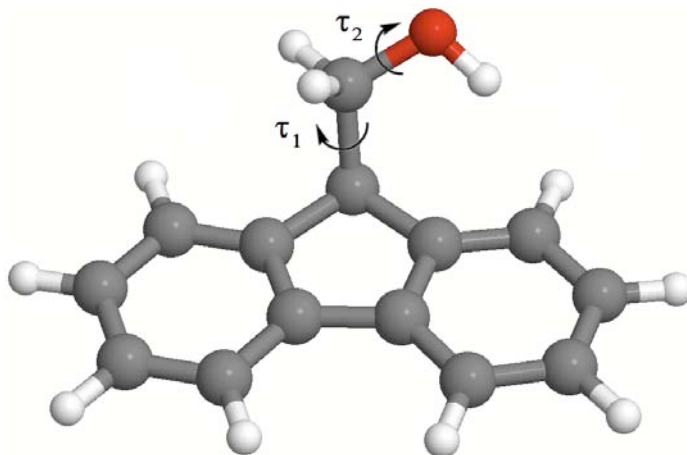
Scheme 5.1

nature of π-H bonds, large scale torsional motions might also be expected about one or both of the torsional angles, τ_1 and τ_2. In 2004, Basu and Knee[9] studied 9FM and its clusters with resonance enhanced multi-photon ionization (REMPI) and IR-UV hole burning spectroscopies. They found that two conformers of the bare molecule were present, one with the –OH group lying above the aromatic plane (*sym*-9FM), and a second with the –OH group tilted away from the plane (*unsym*-9FM). The two conformers exhibited distinct –OH stretching frequencies, 3618 and 3647 cm^{-1}, respectively. The band having the larger ν_{OH} value was assigned to *sym*-9FM.

Described here are high resolution S$_1$←S$_0$ fluorescence excitation experiments that were designed to distinguish the two conformers of 9FM based on differences in their rotational

constants. The experiments show that, indeed, two conformers are present, but also that their identities should be reversed. Additionally, the *sym* conformer origin band was found to be split into two subbands at high resolution, whereas the *unsym* conformer origin band was not. Deuterium substitution experiments clearly show that the motion that is responsible for this splitting is a torsional motion of the attached –OH(D) group. But, surprisingly, the high resolution spectrum of *sym*-9FMD was found to be split into *three* components, evidencing the presence of a secondary minimum on the –OH torsional surface. Observation of this minimum provides still more detailed information about the π-H bonding interaction between the flexible –CH_2OH tail and the aromatic system to which is attached.

5.3   EXPERIMENTAL

9FM (99.0% purity) was purchased from Sigma-Aldrich and used without further purification. A deuterated version of 9FM, referred to as 9FMD, also was prepared and studied. Deuteration was carried out by dissolving a solid sample of 9FM in deuterated methanol (99% atom D). The solution was mixed for several days on a magnetic stir plate, and the solvent was then removed with a vacuum line. This process was repeated several times to ensure a high yield of deuterated sample. A subsequent batch also was made using deuterated ethanol (99.5% atom D) as the solvent. A 300 MHz ^{1}H-NMR was taken of the samples both at the beginning and end of the process to confirm the success and selectivity of the deuteration.   In addition, an electrospray ionization mass spectrum was taken to confirm that there was only one site of deuteration, that of the hydrogen belonging to the –OH group.

Vibrationally resolved $S_1 \leftarrow S_0$ fluorescence excitation experiments were conducted according to the following specifications. The sample of interest, either 9FM or 9FMD, was heated to ~ 90 °C, seeded into 1810-2070 Torr of dry helium gas (> 90% purity), and expanded through a 1 mm diameter orifice pulsed valve (General Valve Series 9), operating at 10 Hz, into a vacuum chamber (10^{-5} Torr). The output of the nozzle was then crossed 2 cm downstream with the doubled output of a Quanta Ray Nd^{3+}: YAG (Model DCR-1A) pumped dye laser (Model PDL-1). To achieve the desired frequency, the Nd^{3+}:YAG laser was set to the second harmonic and Kiton Red dye was used. Frequency doubling was done externally with a potassium dihydrogen phosphate (KDP) crystal. The visible portion of the laser output was filtered, leaving ultraviolet (UV) light with a spectral resolution of ~ 1 cm^{-1}. A photomultiplier tube (EMI 98139B), positioned at right angles to both the laser and molecular beams, was used to collect the fluorescence. A boxcar integrator (Stanford Research Systems) was used to process the data, and Quick Data Acquisition software (Version 1.0.5) was used to record the data.

Rotationally resolved $S_1 \leftarrow S_0$ fluorescence excitation experiments were performed using a molecular beam laser spectrometer, described in detail elsewhere.[10] Briefly, the sample was heated to ~150 °C, seeded in dry argon gas (>99% purity), and expanded into a vacuum through a 240 µm quartz nozzle. The molecular beam was skimmed 2 cm downstream with a 1 mm diameter skimmer and then crossed 15 cm downstream with the output of a modified Ar^+-pumped wave continuous ring dye laser (Spectra-Physics 380D). For the origin bands of 9FM and 9FMD, Rhodamine 590 dye was used to obtain the correct visible frequency, and a 600 nm $LiIO_3$ crystal was used for intra-cavity frequency doubling. Approximately 200 µW of UV light was produced. For the vibronic band of 9FMD, the output of the ring dye laser was doubled externally by a Spectra-Physics Wavetrain using a 600 nm BBO crystal. Roughly 500 µW of

UV light was produced. In all cases, fluorescence was collected using spatially selective optics and detected by a photomultiplier tube (EMI 9813 QB) and photon counting system. An iodine (I_2) absorption spectrum and relative frequency markers were simultaneously collected. All information was processed using the jba95 data acquisition system.[11] Absolute transition frequencies of the excitation spectrum were determined by comparison with the I_2 spectrum (accuracy ~ 30 MHz).[12] The frequency markers were generated by a stabilized etalon with a free spectral range of 299.7520±0.0005 MHz in the fundamental frequency of the dye. Fitting of the spectrum was done using the least squares fitting program jb95.[13]

5.4 RESULTS

5.4.1 9-Fluorenemethanol (9FM)

The vibrationally resolved $S_1 \leftarrow S_0$ fluorescence excitation spectrum of 9FM is shown in Figure 5.1. This spectrum is very similar to the REMPI spectrum previously recorded by Basu and Knee[9], who found two origins, or 0_0^0 bands, at ~ 33565 and ~ 33790 cm^{-1}, Bands I and II, respectively. Two minimum energy conformations of 9FM were identified in the previous work; the *sym* conformer, in which the heavy atoms of the methanol group are in a symmetric arrangement with respect to the aromatic plane, and the *unsym* conformer, in which the heavy atoms are unsymmetric with respect to this plane. These structures are shown in Fig. 5.2. Basu and Knee[9] argued that their studies of clusters of 9FM supported the assignments of Band I at 33565 cm^{-1} to *unsym*-9FM and Band II at 33790 cm^{-1} to *sym*-9FM. However, this assignment was inconsistent with the reported *ab initio* calculations (B3LYP/6-
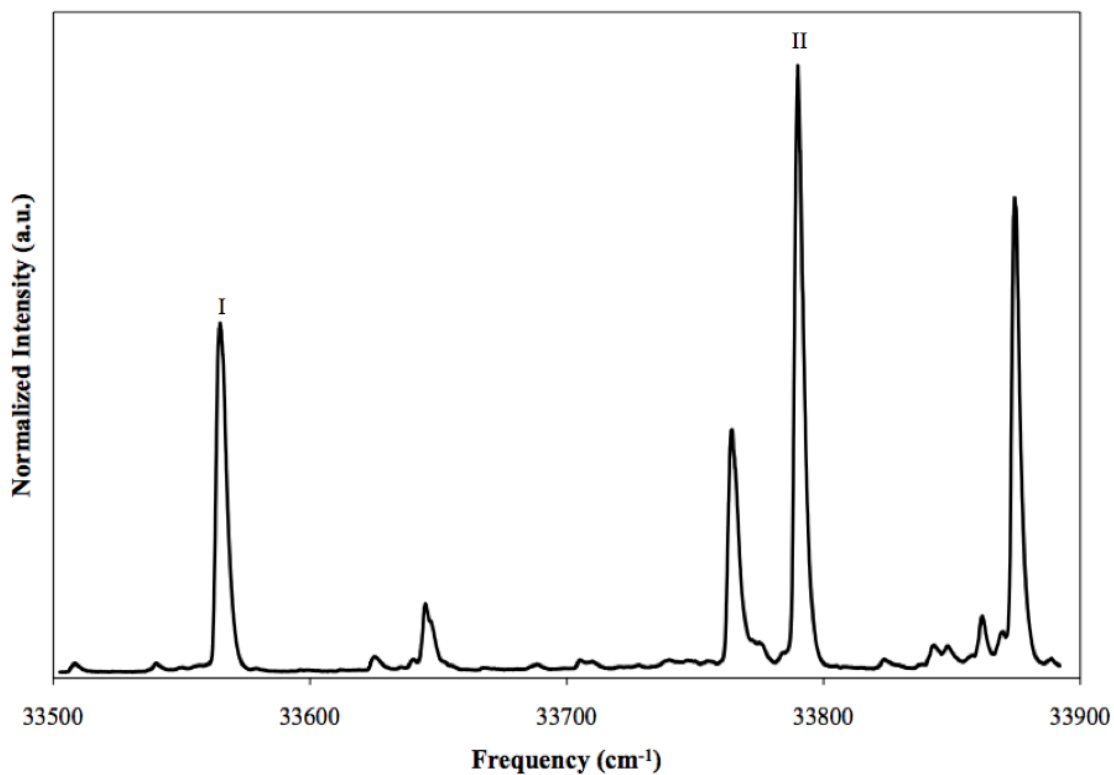
Figure 5.1. Vibrationally resolved $S_1 \leftarrow S_0$ fluorescence electronic excitation spectrum of 9FM. Origin bands occur at ~33565 cm^{-1} and ~33790 cm^{-1} and are designated as I and II, respectively.
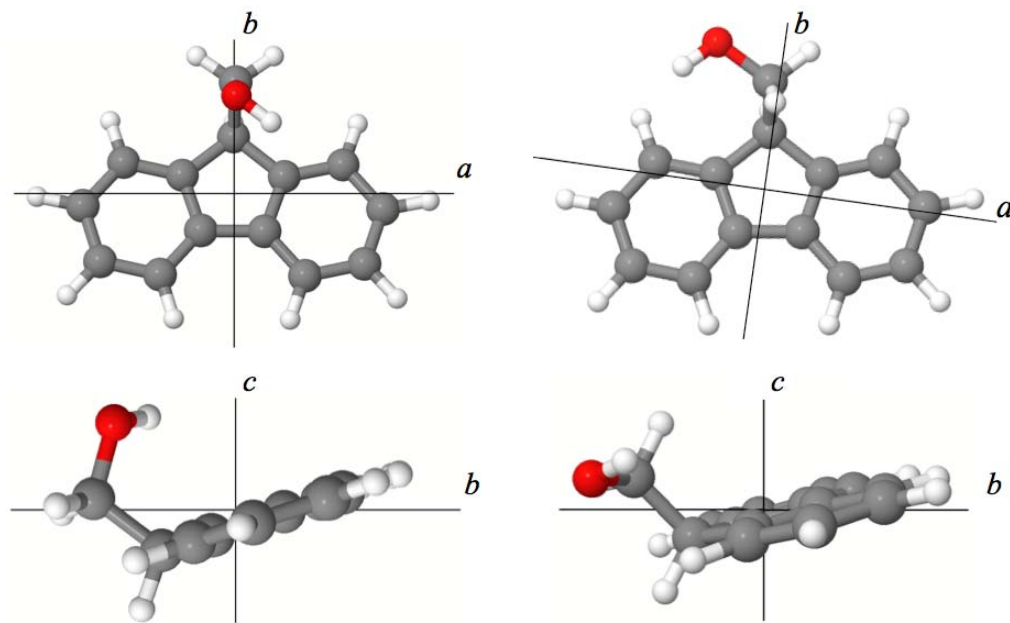
Figure 5.2. Illustrations of the two minimum energy conformations of 9FM. The structures on the left show the *sym* conformer, and the structures on the right show the *unsym* conformer. Inertial axes are labeled for reference.

31G*),[9] which predicted the *unsym* conformer to lie lower in energy than the *sym* conformer by ~ 100 cm^{-1}, suggesting that Band II (the stronger band) should be assigned to *unsym*-9FM.

An unambiguous assignment of the two origin bands of 9FM was provided by studies of the rotationally resolved spectra. Interestingly, Band I was found to be split into two subbands, separated by 1.9 cm^{-1}. These are shown in Figs. 5.3 and 5.4, and will be referred to as Bands I$_{red}$ and I$_{blue}$, respectively. (The appearance of subbands in Band I is an intriguing result and will be discussed in detail later.) The spectrum of Band II is shown in Fig. 5.5 and is found to consist of a single band. All three bands (I$_{red}$, I$_{blue}$, and II) appear to be predominantly *a*-type in character, just as for the parent molecule, fluorene (FLU).[14]

Each of the three bands was then fit using rigid rotor Hamiltonians for each state,

$$\hat{H}_r = AP_a^2 + BP_b^2 + CP_c^2 \tag{5.1}$$

Here, P_a, P_b, and P_c are the components of the rotational angular momentum about the *a*, *b*, and *c* inertial axes of the molecule; A, B, and C are the rotational constants (in Hz) about each axis; and I_a, I_b, and I_c, are the corresponding moments of inertia:

$$I_a = \frac{h}{8\pi^2 A}, \qquad I_b = \frac{h}{8\pi^2 B}, \quad and \quad I_c = \frac{h}{8\pi^2 C} \tag{5.2}$$

Ab initio calculations were used to determine initial values of rotational constants from the optimized geometries of both conformers; ground state constants were calculated at the MP2 level with a 6-31G** basis set, and excited state constants were obtained with CIS calculations using a 6-31G** basis set.[15] Refined values of the constants were then obtained by comparing simulated spectra to observed ones and minimizing the differences between the calculated and experimental line positions in a least-squares fashion. This process was iterated until the simulated spectrum matched all of the features of the experimental spectrum, yielding an OMC
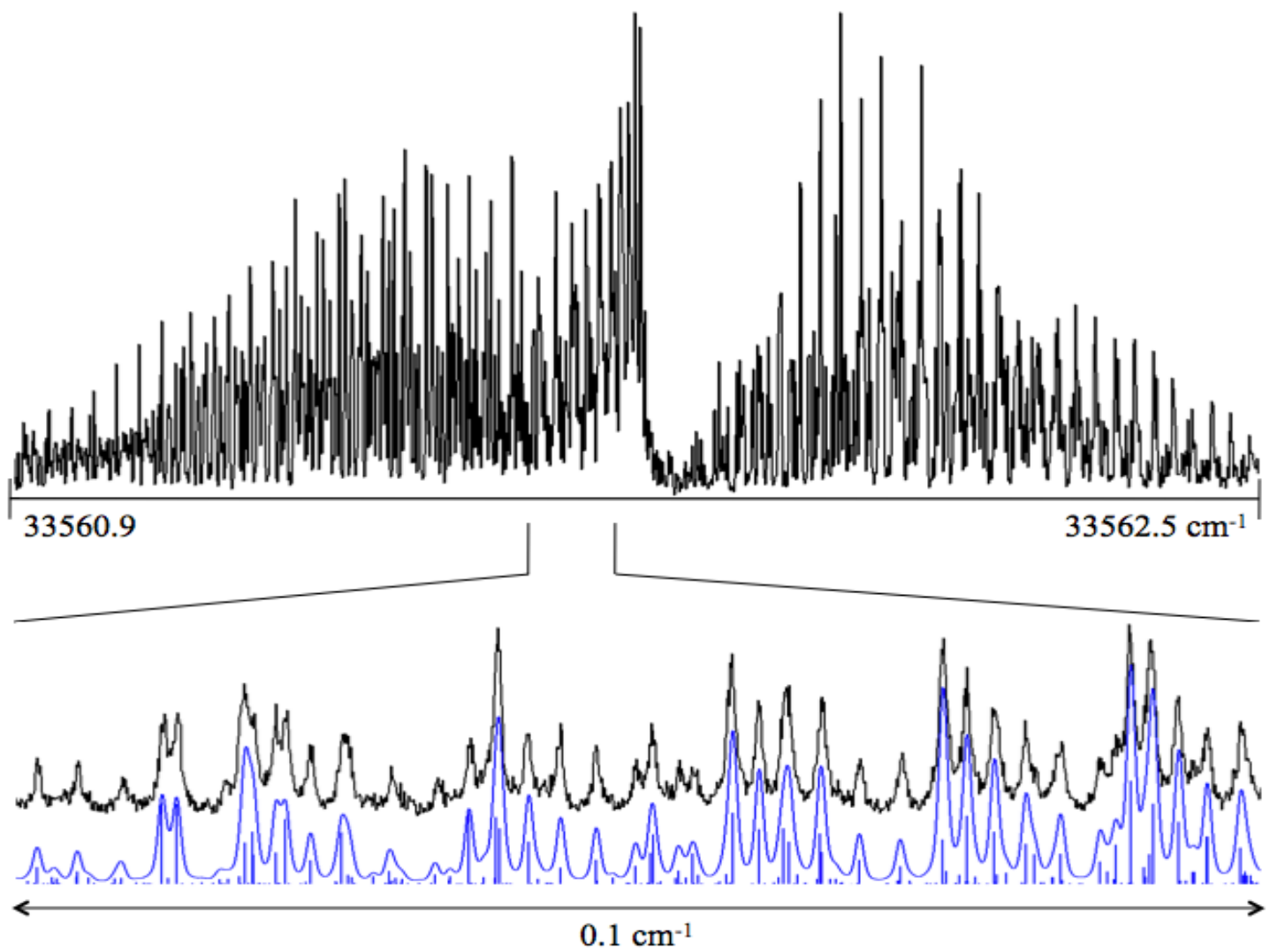
Figure 5.3. Rotationally resolved $S_1 \leftarrow S_0$ fluorescence electronic excitation spectrum of Band I_{red} of 9FM, with the origin occurring at 33561.7 cm^{-1}. The top panel shows the entire spectrum, and the bottom panel shows a comparison of a portion of the experimental spectrum (black trace) with two simulated spectra (blue trace), with and without a convoluted lineshape function.
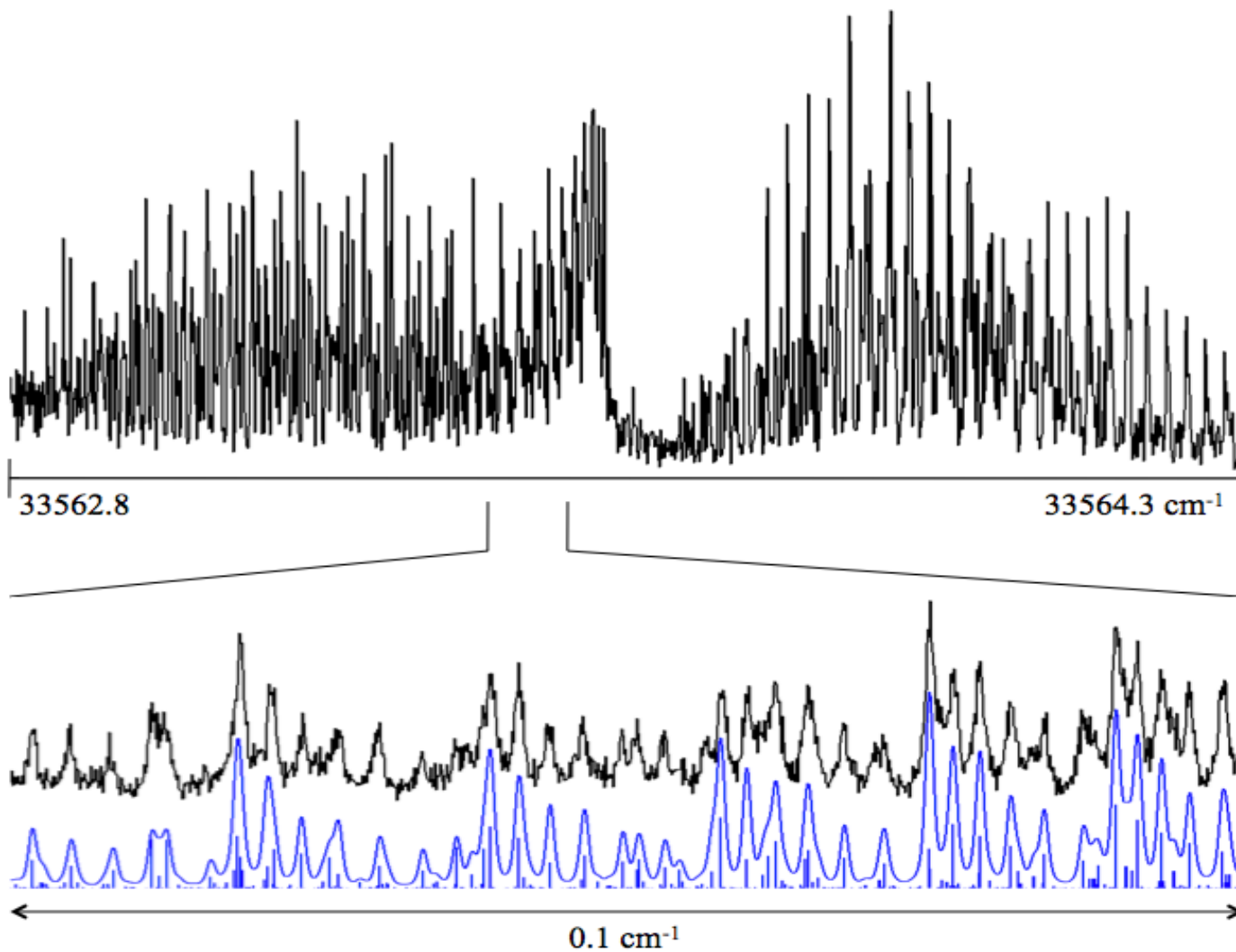
Figure 5.4. Rotationally resolved $S_1 \leftarrow S_0$ fluorescence electronic excitation spectrum of the I_{blue} band of 9FM, with the origin occurring at 33563.6 cm^{-1}. The top panel shows the entire spectrum, and the bottom panel shows a comparison of a portion of the experimental spectrum (black trace) with two simulated spectra (blue trace), with and without a convoluted lineshape function.
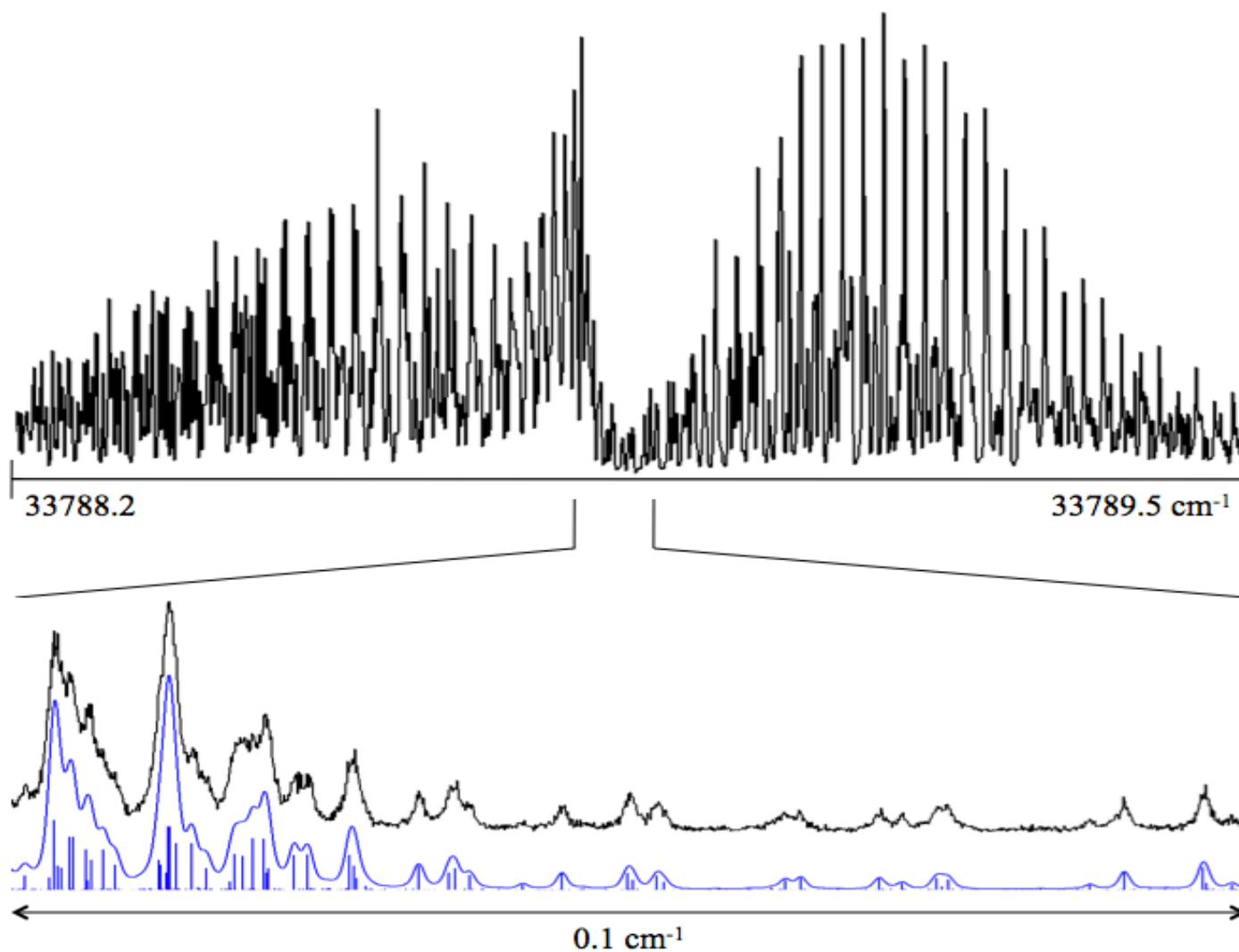
Figure 5.5. Rotationally resolved $S_1 \leftarrow S_0$ fluorescence electronic excitation spectrum of Band II of 9FM, with the origin at 33788.8 cm^{-1}. The top panel shows the entire spectrum, and the bottom panel shows a comparison of a portion of the experimental spectrum (black trace) with two simulated spectra (blue trace), with and without a convoluted lineshape function.

(observed minus calculated) standard deviation of the fit of less than 2.8 MHz for all 9FM spectra. The addition of Watson distortion terms[16] did not significantly improve the OMC.

Table 5.1 summarizes the results obtained from the fits of all three bands of 9FM. Comparison of the observed values of A, B, and C with those predicted for the two conformers shows immediately that Bands I_{red} and I_{blue} should be assigned to *sym*-9FM, and that Band II should be assigned to *unsym*-9FM. This is the opposite of the assignment of Basu and Knee.[9] Most notable in Table 5.1 are the planar moments; *sym*-9FM has an inertial defect $\Delta I = -0.5 P_c = -137$ amu Å^2 in the ground state, whereas *unsym*-9FM has $\Delta I = -0.5 P_c = -57.6$ amu Å^2 in the ground state, the smaller (in magnitude) value arising from the smaller displacement of the $-CH_2OH$ group from the aromatic plane (*cf.* Fig. 5.2). Comparing the P_a and P_b values (Table 1) leads to the same conclusion. The two conformers have approximately the same fluorescence lifetimes; the Lorentzian contributions to the single rovibronic linewidths are 12 and 15 MHz, respectively, for *sym*- and *unsym*-9FM.

5.4.2 Deuterated 9-Fluorenemethanol (9FMD)

Next, 9FMD was studied at high resolution, in order to explore in greater detail the splitting of the *sym*-9FM origin band into two subbands. The corresponding band of 9FMD lies at ~ 33569 cm^{-1}, blue shifted from the *sym*-9FM origin band by 4 cm^{-1}. Its high resolution spectrum is shown in Fig. 5.6. Again, there appear to be two subbands, but the magnitude of their separation is significantly reduced from 1.9 to 0.3 cm^{-1}. This shows that the splitting of the *sym*-9FM origin is primarily associated with the torsional motion of the $-OH(D)$ group. Again, both subbands are predominantly *a*-type in character, and could be fit with rigid-rotor Hamiltonians for both electronic states. The resulting parameters are listed in Table 5.2. Single

Table 5.1. Experimental inertial parameters of 9FM. Parameters calculated at the MP2/6-31G** and CIS/6-31G** level of theory have also been included for comparison.

	Experimental			Calculated	
	Band I$_{red}$	**Band I$_{blue}$**	**Band II**	**Sym**	**Unsym**
S$_0$					
A (MHz)	1024.6 (1)	1025.2 (2)	936.2 (2)	1047.7	957.4
B (MHz)	543.4 (1)	543.5 (1)	551.4 (1)	541.2	547.8
C (MHz)	392.8 (1)	392.9 (1)	361.3 (1)	397.1	364.5
ΔI (amu Å^2)	-136.7 (2)	-136.5 (2)	-57.6 (2)	-143.5	-63.9
P_a (amu Å^2)	861.7 (2)	861.6 (2)	887.7 (2)	862.0	890.6
P_b (amu Å^2)	424.9 (2)	424.7 (2)	511.0 (2)	410.6	495.9
P_c (amu Å^2)	68.3 (2)	68.3 (2)	28.8 (2)	71.7	32.0
S$_1$					
ΔA (MHz)	-28.5 (1)	-28.4 (2)	-27.6 (2)	-48.5	-36.8
ΔB (MHz)	5.6 (1)	5.5 (1)	4.9 (1)	8.5	8.2
ΔC (MHz)	-1.3 (1)	-1.3 (1)	-2.2 (1)	-1.3	2.4
ΔI (amu Å^2)	-137.0 (2)	-137.0 (2)	-57.3 (2)	-148.2	-80.5
OMC	1.7	2.4	1.7		
Assigned lines	169	138	100		
$a/b/c$	97/1/2	98/1/1	97/2/1		
Temperature (K)	3.5	4.5	3		
Origin (cm^{-1})	33561.7	33563.6	33788.8		

Figure 5.6. Rotationally resolved $S_1 \leftarrow S_0$ fluorescence electronic excitation spectrum of the *sym*-9FMD origin band. The top panel shows a comparison of the entire experimental spectrum (black trace) to a simulation. The blue trace is composed of two subbands occurring at 33568.9 and 33569.2 cm^{-1}, and the third subband, occurring at 33568.8 cm^{-1}, is shown in orange. The bottom panels show comparisons of small portions of the experimental spectrum (black trace) with the simulations, which include a convoluted lineshape function. The blue trace is that of the two subbands, with the individual simulated transitions of each subband shown in blue and red; the third subband is shown in green (note, the color has been changed from orange for visual purposes).

Table 5.2. Experimental inertial parameters for the subbands I_{red} and I_{blue} of the *sym*-9FMD origin band and the +198 cm^{-1} vibronic band. A comparison to theory (MP2/6-31G** and CIS/6-31G**) is included.

	Experimental				Calculated
	Origin Band		Vibronic Band		Origin Band
	Band I_{red}	**Band I_{blue}**	**Band I_{red}**	**Band I_{blue}**	
S_0					
A (MHz)	1011 (2)	1015 (3)	1014 (1)	1006 (1)	1015
B (MHz)	541.4 (2)	541.4 (3)	540.8 (1)	542.3 (1)	540.8
C (MHz)	391.8 (1)	392.0 (1)	391.8 (1)	391.8 (1)	392.1
ΔI (amu Å^2)	-143 (1)	-142 (2)	-143.0 (6)	-144.4 (6)	-143.5
S_1					
ΔA (MHz)	-27 (2)	-28 (3)	-27 (1)	-28 (1)	-28.1
ΔB (MHz)	5.6 (2)	5.0 (2)	6.1 (1)	5.3 (1)	6.8
ΔC (MHz)	-1.3 (1)	-1.4 (1)	-1.5 (1)	-1.4 (1)	-2.4
ΔI (amu Å^2)	-143 (1)	-143 (2)	-141.3 (6)	-145.1 (6)	-153.9
OMC	9.0	7.9	7.8	10.3	
Assigned lines	66	50	114	95	
Temperature (K)	5	4.5	3	3	
a/b/c	98/1/1	98/1/1	95/1/4	95/1/4	
Origin (cm^{-1})	33568.9	33569.2	33767.1	33767.4	

rovibronic lines exhibited Voigt profiles with Gaussian linewidths of 18 MHz and Lorentzian linewidths of 13 MHz.

A closer examination of the data in Table 5.2 shows that the OMC's of the fits of the *sym*-9FMD origin subbands are significantly larger than those for the *sym*-9FM origin subbands. Additionally, there are several intense transitions near 33569 cm^{-1} that are not accounted for by the simulations (see Fig. 5.6). Much effort was devoted to fitting these using only two subbands, including several attempts with genetic algorithms.[17]

After these endeavors proved unsuccessful, a third subband was added to the spectrum. By placing the origin at 33568.8 cm^{-1}, it was found that the Q-branch transitions of this subband could account for the general features that were missing from the fit (see Fig. 5.6). The simulated rotational parameters for the third subband are listed in Table 5.3. It should be noted that these parameters are not the result of a "genuine fit"; *i.e.*, individual transitions were not assigned. Rather, the parameters are the result of manually adjusting the rotational constants by eye to produce a simulation that agrees with the patterns in the experimental spectrum. The reported ΔA, ΔB, and ΔC values were essential to replicate the intense lines near 33569 cm^{-1}; small adjustments of these values result in simulations that no longer reproduced these features. However, the ground state A, B and C rotational constants were not as crucial to the fit, and the values shown in Table 5.3 could be varied a fair amount without negatively affecting the simulation's Q-branch pattern that accounts for the previously missing intensity. Single rovibronic lines exhibited Lorentzian linewidths of 18 MHz, and the maximum simulated J value was 9 (in contrast to the J_{max} values of ~ 40 used for the fits given in Tables 5.1 and 5.2).
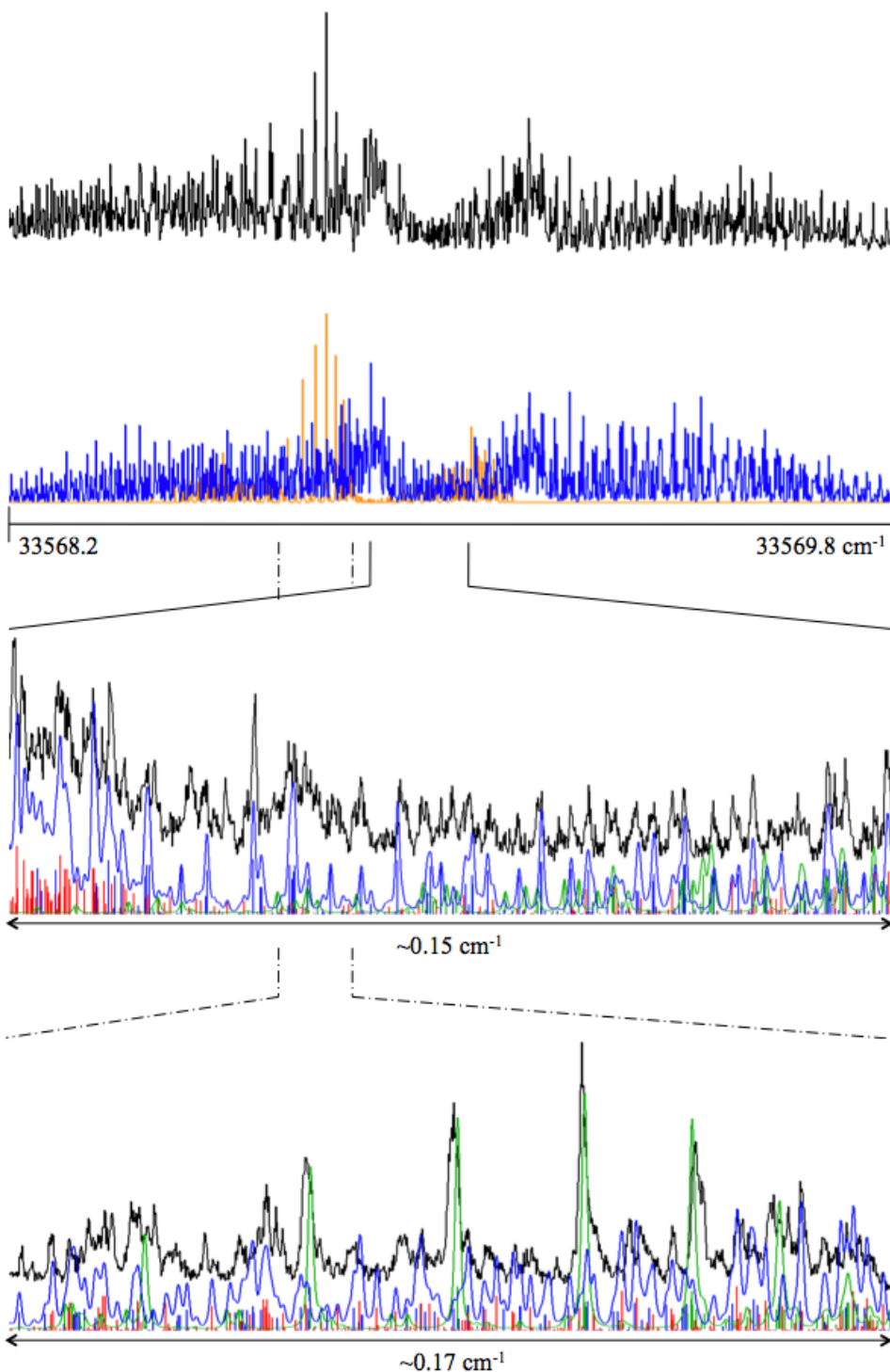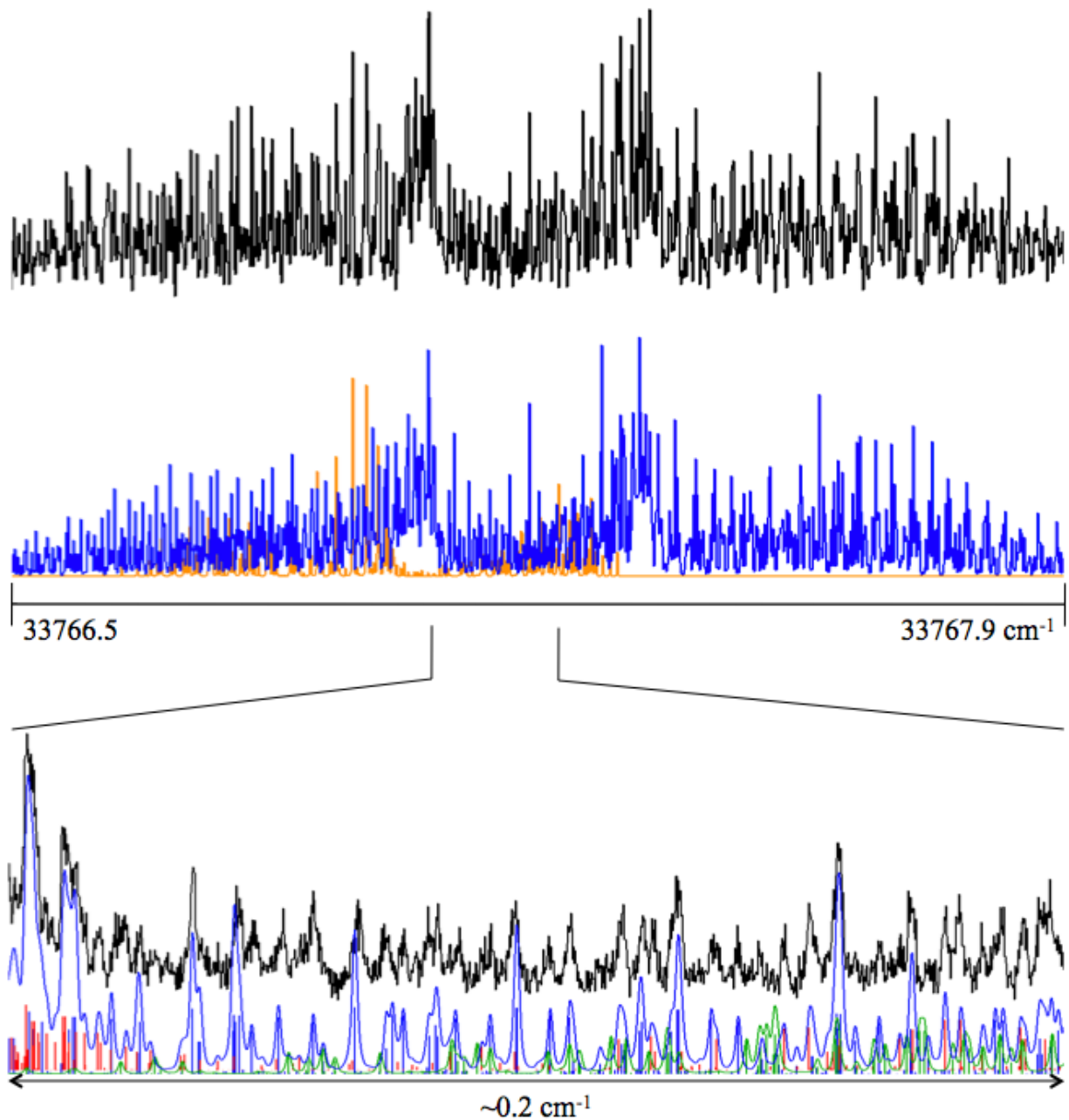
Figure 5.7. Rotationally resolved $S_1 \leftarrow S_0$ fluorescence electronic excitation spectrum of the *sym*-9FMD +198 cm^{-1} vibronic band. The top panel shows a comparison of the entire experimental spectrum (black trace) to a simulation. The blue trace is composed of two subbands occurring at 33767.1 and 33767.4 cm^{-1}, and the third subband, occurring at 33767.0 cm^{-1}, is shown in orange. The bottom panel shows a comparison of a portion of the experimental spectrum (black trace) with the simulations, which include a convoluted lineshape function. The blue trace is that of the two subbands, with the individual simulated transitions of each subband shown in blue and red; the third subband is shown in green (note, the color has been changed from orange for visual purposes).

A high resolution spectrum also was recorded for the +198 vibronic band of *sym*-9FMD and is shown in Figure 5.7. FLU (and several substituted fluorenes) also has a vibronic band located near 200 cm^{-1}, which has been assigned to a symmetric in-plane bending mode.[18] As was the case in the origin band, two subbands alone could not reproduce all of the spectral features observed in this band; there are several intense broad lines occurring near 33767 cm^{-1} that were not accounted for by a simulation using only two subbands. It was again observed that the addition of a third simulated band resulted in a reasonable match of the missing spectral features. Single rovibronic lines exhibited Lorentzian linewidths of 18 MHz, and the maximum simulated *J* value was 9. The rotational parameters for all three subband simulations are given in Tables 5.2 and 5.3.

Table 5.3. Experimental inertial parameters for the third subbands observed in the *sym*-9FMD origin and +198 cm^{-1} vibronic bands. A comparison to theory (MP2/6-31G** and CIS/6-31G**) is included.

	Experimental		Calculated
	Origin Band	**Vibronic Band**	**Origin Band**
S$_0$			
A (MHz)	1015	1015	1015.4
B (MHz)	541	544	540.9
C (MHz)	394	393	393.0
ΔI (amu Å^2)	-149.4	-141.0	-149.4
S$_1$			
ΔA (MHz)	-48.5	-50.0	-37.1
ΔB (MHz)	0.0	0.0	5.8
ΔC (MHz)	-1.4	-1.4	2.1
ΔI (amu Å^2)	-169.8	-165.4	-161.9
Origin (cm^{-1})	33568.8	33767.0	

New insights into the structural and dynamical properties of π-hydrogen (π-H) bonds are provided by the accumulated results of these spectroscopic studies. 9FM has two stable conformers, *sym* and *unsym*. The *sym* conformer has the oxygen atom of its –OH group symmetrically placed above the fluorene short axis, with the hydrogen atom pointing towards the top of an aromatic ring, whereas the *unsym* conformer has the oxygen atom tilted away from this axis, with the hydrogen atom pointing towards the side of an aromatic ring. Evidence for a stabilizing π-H bonding interaction in the *sym* structure is found in the difference in their –OH stretching frequencies; 3618 cm^{-1} for the *sym* conformer and 3647 cm^{-1} for the *unsym* conformer.[9] A decrease in this frequency is indicative of an *intra*molecular hydrogen bonding interaction between the –OH group and the π-electrons of the ring, as in the analogous case of "back-bonding" in transition metal carbonyl complexes. A similar effect occurs in 2-phenethyl alcohol.[4]

More information about the motion of the attached –CH$_2$OH group in both electronic states of 9FM was provided by relaxed scans[15] of their potential energy surfaces (PES's) along the two torsional coordinates, τ_1 and τ_2. [It will be recalled that changing τ_1 rotates the –CH$_2$OH group about the C-C bond connecting it to the five-membered ring, whereas changing τ_2 rotates the –OH group about the C-O bond (see Scheme 5.1).] The results for the ground state (MP2/6-31G**) are shown in the lower right-hand portion of Fig. 5.8, and the results for the excited state (CIS/6-31G**) are shown in the upper right-hand portion of Fig. 5.8. Qualitatively, the two surfaces are similar. The two identical *sym* conformers are found at $(\tau_1, \tau_2) = (180°, 60°)$ and $(180°, 300°)$;   the two identical *unsym* conformers are found at $(\tau_1, \tau_2) = (60°, 70°)$ and

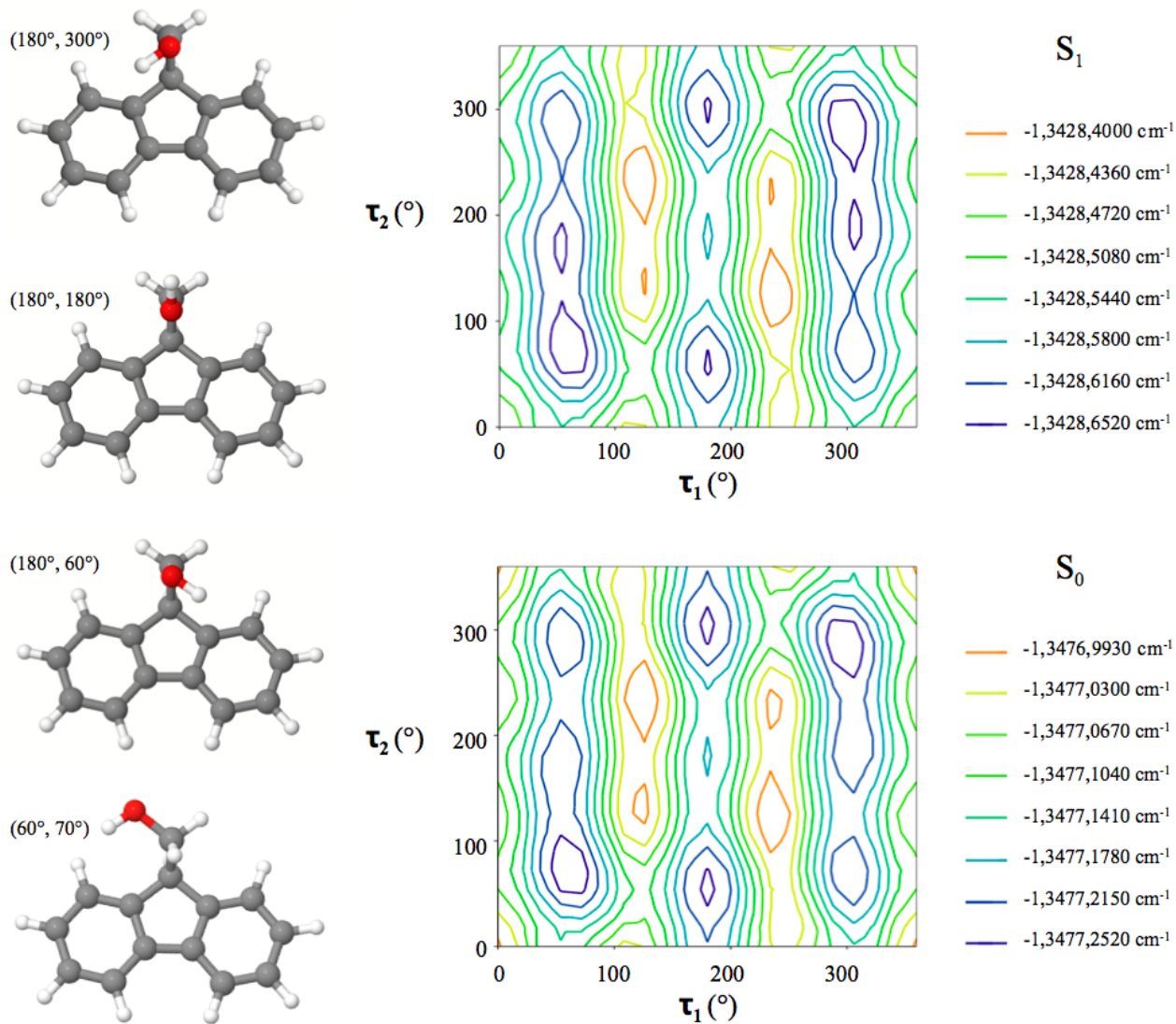**Figure 5.8.** Contour plots resulting from relaxed potential energy surface scans done for the ground (lower) and excited states (upper) of 9FM. The angles τ_1 and τ_2 were each changed in 10° steps. Energies were calculated at the MP2/6-31G** and CIS/6-31G** levels of theory. Several of the corresponding structures are shown on the left, and the (τ_1, τ_2)-coordinates have been specified for each.

(300°, 290°). [The small difference between the cited values of τ_2 and their canonical values in the *unsym* conformers (*e.g.,* $\tau_2 = 70°$ rather than 60°) may be attributed to a repulsive interaction involving the ring hydrogen atoms, H1 or H8, possibly mediated by backbone correlation effects.] The one-dimensional barriers along the τ_1 coordinate (-CH$_2$OH torsion) are predicted to be of order 2000 cm^{-1} whereas those along the τ_2 coordinate (-OH torsion) are predicted to be of order 500 cm^{-1}, in the ground electronic state. This explains why only the *sym*-9FM conformer exhibits an –OH tunneling splitting in its electronic spectrum.

The data in Fig. 5.8 also provide important clues about the origin of the third subband in the high resolution spectrum of *sym*-9FMD. The presence of this feature initially seemed very puzzling to us, especially since it did not appear in the spectrum of the unsubstituted molecule. Several attempts to account for it failed. First, 300 MHz ^{1}H-NMR and electrospray ionization mass spectrometry both verified that the deuteration was selective. Then, the molecular beam expansion conditions in the high resolution experiment were varied over a wide range but the relative intensities of the three subbands always remained the same, showing that another species could not be responsible for the third subband. Next, spectra were taken in both helium and argon, a water trap was added, and the deuteration was carried out with both methanol and ethanol, to rule out the possible formation of other complexes. No changes were observed. Finally, the appearance of a similar feature in the high resolution spectrum of the +198 vibronic band of *sym*-9FMD convinced us that the third subband was a property of the isolated molecule.

Re-examining Fig. 5.8, we see that there is a secondary minimum on the isomerization pathway linking the two *sym*-9FM structures, located at the point $(\tau_1, \tau_2) = $ (180°, 180°). This point identifies a *sym*-up conformer, shown in Scheme 5.2 below. This structure has the
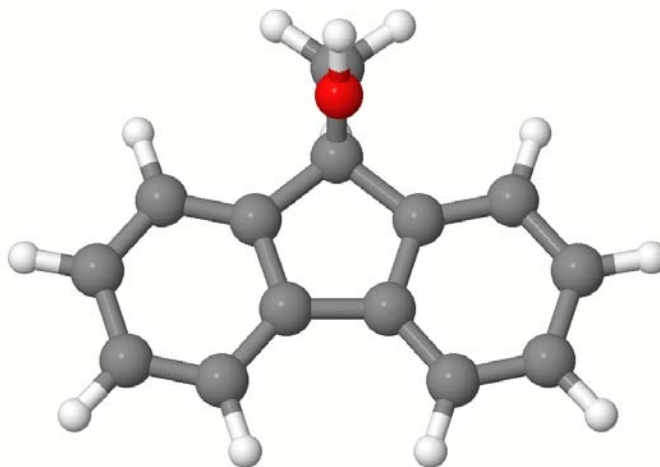
Scheme 5.2

hydrogen atom of its –OH group pointing away from the five-membered ring, in an "up" configuration. The calculated energy of this structure is ~ 1000 cm^{-1} above the two *sym*-9FMD conformers (now called *sym*-down). Thus, the barrier connecting them is relatively low. We therefore postulate that, in 9FMD, the molecule can be trapped in a shallow well midway between the two *sym*-down structures, and that the third subband in the spectrum of 9FMD is the rotationally resolved spectrum of this "in-between" structure, *sym*-up. Apparently, the zero-point energy (ZPE) level of the protonated species in the ground state lies above the barrier connecting the shallow well to the deeper wells of the *sym*-down structures, thereby explaining why the third sub-band is only observed in the spectrum of the deuterated molecule.

Other data support this interpretation. Table 5.3 lists the calculated (MP2/ and CIS/6-31G**) rotational constants of the *sym*-up structure and compares them to the experimental values. Given the uncertainty in these, the agreement is excellent. Further, we note that the maximum *J* observed in the simulated spectrum of the third subband is *J* = 9, so it is not unreasonable to suppose that the spectrum "breaks-off" above this value. At *J* = 9, the total rotational energy of the molecule is only a few cm^{-1}, which supports that idea that the ZPE level of the deuterated molecule is very weakly bound in the shallow potential of the *sym*-up structure.

Quantitatively, we can reproduce the general shape of the calculated PES using a three-term potential of the form[19]

$$V(\tau_2) = \frac{1}{2}V_1(1 - \cos\tau_2) + \frac{1}{2}V_2(1 - \cos 2\tau_2) + \frac{1}{2}V_3(1 - \cos 3\tau_2) \qquad (5.3)$$

Here, a positive V_1 creates a barrier at $\tau_2 = 180°$, a positive V_2 creates two barriers at $\tau_2 = 90°$ and 270°, and a positive V_3 creates three barriers at 60°, 180°, and 300°. Using the energies calculated in the relaxed scans along the τ_2 coordinate, while keeping $\tau_1 = 180°$, the resulting potential energy curves of both electronic states were fit to Eq. (5.3) in a least-squares fashion. Fig. 5.9 shows a comparison between the two ground state curves. The best fit curve has V_1, V_2, and V_3 values of 795, -247, and -546 cm^{-1} in the ground state; the corresponding excited state curve has V_1, V_2, and V_3 values of 596, -346, and -532 cm^{-1}.

Examining the ground state curve, we see that the two *sym*-down structures lie in wells about 500 cm^{-1} below the $\tau_2 = 0$ structure. A barrier of approximately 1000 cm^{-1} lies between the two *sym*-down wells. Nestled in this barrier is the secondary minimum of the *sym*-up structure, stabilized by approximately 200 cm^{-1}. The V_3 term in Eq. (5.3) accounts for the energy differences between the staggered and eclipsed forms of 9FM, generating three minima (see Scheme 5.3); the PES is then modified by the addition of the V_1 and V_2 terms. With V_3 negative, addition of a positive V_1 raises the energy of the *sym*-up structure with respect to that of the *sym*-down structures. Addition of a negative V_2 reduces the depth of the *sym*-up well relative to the depths of the *sym*-down wells. (All structures with τ_2 values lying between 0° and 180° have corresponding mirror image structures with τ_2 values lying between 180° and 360°.)

Fluorene 60° Fluorene 180° Fluorene 300°
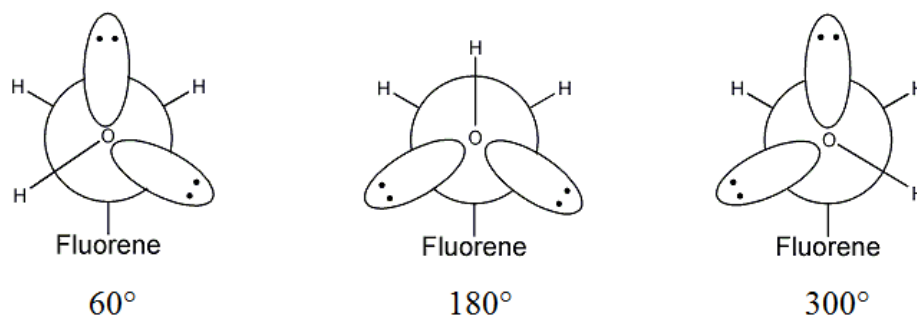
Scheme 5.3
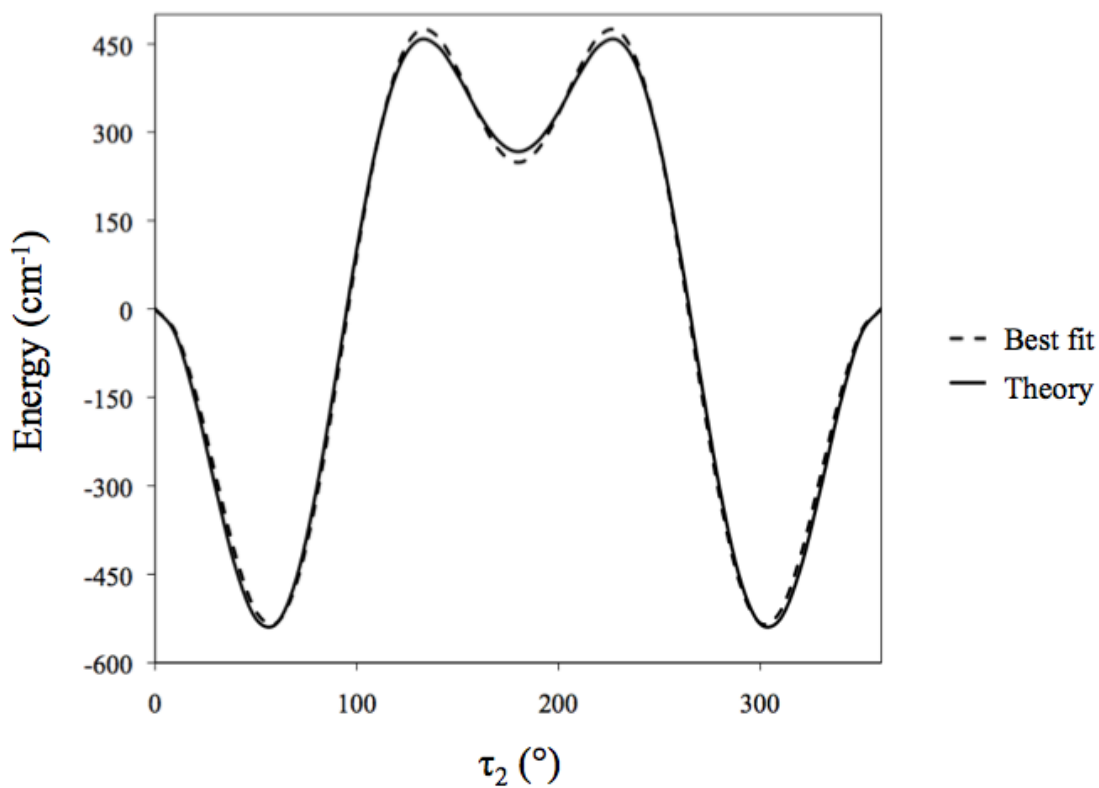
Figure 5.9. Comparison between the *ab initio* potential energy curve (solid) and the best fit curve (dashed) obtained for the ground state using Equation 5. V_1, V_2 and V_3 potential terms were found using a least squares analysis. The best fit values are $V_1 = 795$, $V_2 = -247$ and $V_3 = -546$ cm^{-1}.

Improved values of V_1, V_2, and V_3 in both states can be determined from the measured subband separations, 1.9 and 0.3 cm^{-1} in 9FM and 9FMD, respectively. Owing to selection rules, these separations represent the *difference* in the tunneling splittings along the torsional coordinate in the two electronic states. Thus, we write for each electronic state a "particle-on-the-ring" Hamiltonian[19]

$$\hat{H} = \hat{H}_0 + \hat{H}_1 \tag{5.4}$$

with

$$\hat{H}_0 = -\frac{\hbar^2}{2I_r}\frac{d^2}{d\tau_2^{2}} \tag{5.5}$$

and

$$\hat{H}_1 = \frac{1}{2}V_1\left(1 - \cos\tau_2\right) + \frac{1}{2}V_2\left(1 - \cos 2\tau_2\right) + \frac{1}{2}V_3\left(1 - \cos 3\tau_2\right) \tag{5.6}$$

Here, I_r is the reduced moment of inertia, 1.56 x 10^{-47} kg m^2 for the –OH group and 3.11 x 10^{-47} kg m^2 for the –OD group. The zero-order wavefunctions are of the form

$$\psi_m = \sqrt{\frac{1}{2\pi}}\exp^{im\tau_2} \tag{5.7}$$

giving rise to the matrix elements

$$\left(H_0\right)_{m,m} = m^2\frac{\hbar^2}{2I_r} \tag{5.8}$$

and

$$
\begin{aligned}
\left(H_1\right)_{m,\,m'} = {} & \frac{V_1}{2}\delta_{m,\,m'} - \frac{V_1}{4}\delta_{m',\,m\pm1} + \frac{V_2}{2}\delta_{m,\,m'} \\
& - \frac{V_2}{4}\delta_{m',\,m\pm2} + \frac{V_3}{2}\delta_{m,\,m'} - \frac{V_3}{4}\delta_{m',\,m\pm3}
\end{aligned}
\tag{5.9}
$$

Diagonalization of Eq. (5.4) then leads to the energy eigenvalues of each of the torsional states; $m = 0$, $m = +/-1$, *etc.*, from which the tunneling splittings and subband separations can be determined, for assumed values of V_1, V_2, and V_3 in the two electronic states. Initially, the best-fit barriers estimated from the PES's were used; this led to predicted subband spacings of 0.7 and 0.05 cm^{-1}, much smaller than the experimental values. Then, V_1 was varied between 400 – 1200 cm^{-1}, V_2 was varied between -600 – 0 cm^{-1}, and V_3 was varied between -800 – -200 cm^{-1}. The results were judged based on several criteria; matching the experimental subband spacings, generating a third minimum that was sufficiently shallow in the ground state, but deeper in the excited state, and, finally, producing an origin of the third subband that lies very close (red shifted by ~ 0.1 cm^{-1}) to the origin of the red subband. The parameters were varied in ~ 100 cm^{-1} steps at first, resulting in a handful of candidates that reasonably satisfied the criteria; these candidates were then adjusted in smaller increments to produce the best match. Best fit values of $V_1 = 1140$, $V_2 = -303$, and $V_3 = -390$ cm^{-1} in the ground state, and $V_1 = 1200$, $V_2 = -214$, and $V_3 = -600$ cm^{-1} in the excited state were obtained, yielding predicted subband spacings of 1.9 cm^{-1} in 9FM and 0.3 cm^{-1} in 9FMD, in excellent agreement with experiment.

Figure 5.10 shows plots of these surfaces along the –OH torsional coordinate. While only approximate, they clearly show that excitation of 9FM by light results in a substantial increase in the barrier to torsional motion along the –OH coordinate. Most of the subband splitting comes from the ground state; thus, the isomerization dynamics in the two electronic
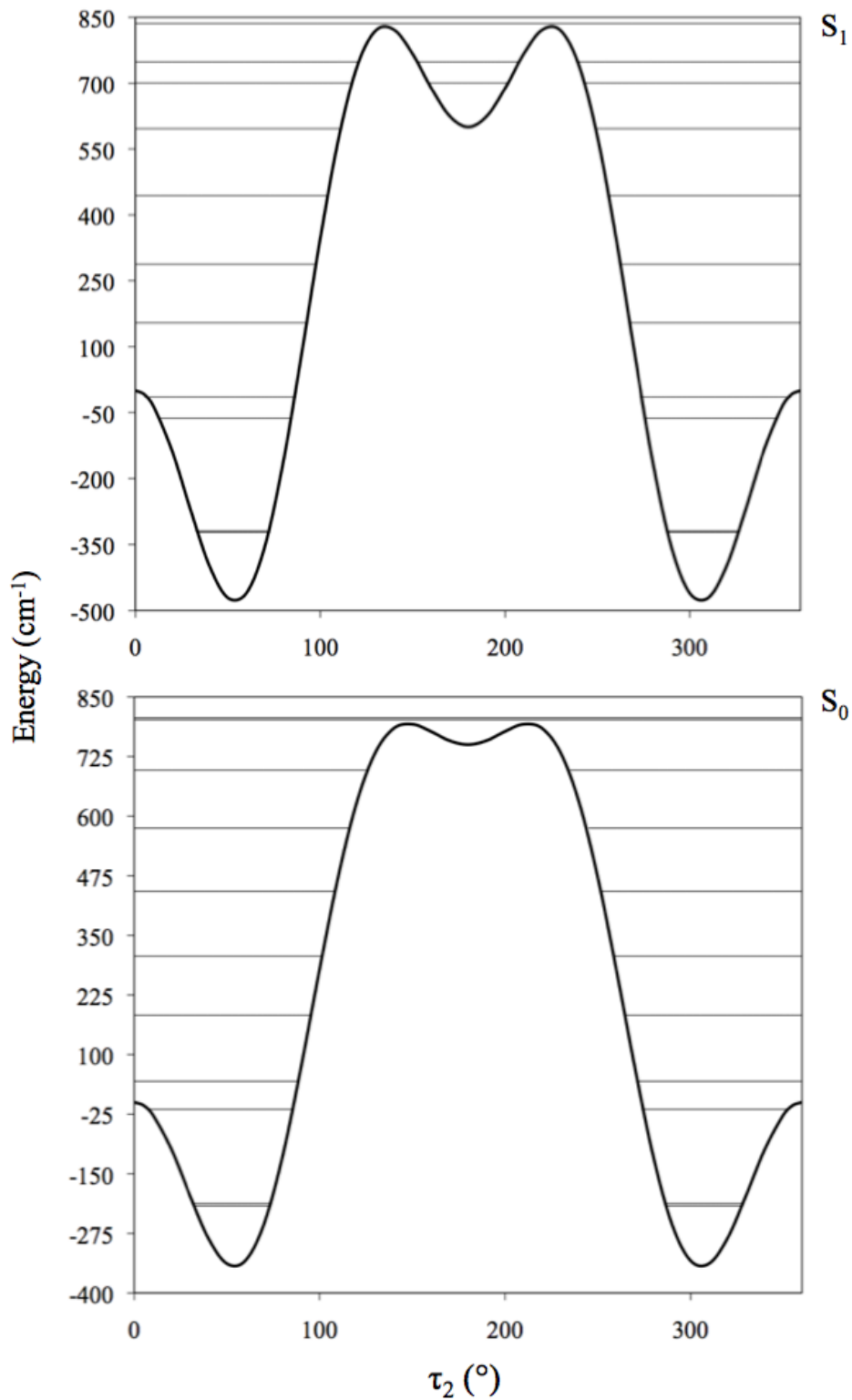
Figure 5.10 Best fit potential energy curves and energy levels for the ground and excited states of *sym*-9FM, plotted against the –OH torsional coordinate (τ_2). In the ground state, $V_1 = 1140$, $V_2 = -303$, and $V_3 = -390$ cm^{-1}; in the excited state, $V_1 = 1200$, $V_2 = -214$, and $V_3 = -600$ cm^{-1}.

states are predicted to be quite different. The depth of the secondary minimum increases from ~ 50 cm^{-1} in the S_0 state to ~ 250 cm^{-1} in the S_1 state, owing to a large increase in the magnitude of the V_3 term and a smaller decrease in the magnitude of the V_2 term, relative to the ground state. The enhanced secondary minimum on the S_1 surface could significantly restrict vibrational energy flow from the torsional coordinate into other energetically accessible modes of the isolated molecule.

The *sym*-up structure has two lone-pair interactions with the aromatic rings, whereas the *sym*-down structures each have one π-H bond and one lone-pair interaction with the rings (see Scheme 5.3). We surmise that the lone pair interactions are relatively unimportant, and that the π-H bond is primarily responsible for the difference in the energies of the two structures. This difference is approximately 1000 cm^{-1} in the two states, or about 12 kJ/mol. This is a reasonable value compared to what is known about the properties of such bonds from a theoretical perspective.[20] Apparently (see Fig. 5.10), there is a small decrease in the strength of this bond when 9FM is excited by light. In any event, this work clearly shows that cation-π interactions with a partial positive charge on the hydroxylic hydrogen atom are more important than the lone-pair-π interactions depicted in Scheme 3, in both electronic states

5.6   SUMMARY

Rotationally resolved $S_1 \leftarrow S_0$ fluorescence excitation spectra of 9-fluorenemethanol have been analyzed and used to assigned bands to either symmetric (*sym*) or unsymmetric (*unsym*) conformers of the isolated molecule. The two conformers differ in the orientation of the attached –CH$_2$OH group with respect to the ring plane. Band I has been assigned to the *sym* conformer,

while Band II has been assigned to the *unsym* conformer, based on differences in their measured rotational constants.   This assignment is the opposite of that made previously using REMPI spectroscopy.[9]

Additionally, splittings have been observed in the high resolution spectrum of the *sym* conformer. Substitution of the hydroxyl hydrogen atom with deuterium shows that the motion which is responsible for this splitting is the torsional motion of the –OH group about the C-O bond. The deuterium labeling experiment further shows that there are three minima along this coordinate; a *sym*-up conformer in which the hydrogen atom of the –OH group points away from the five-membered ring, and two *sym*-down conformers in which the hydrogen atom of the –OH group points towards one of the two six-membered rings, in a π-hydrogen bonding configuration. The ground state well corresponding to the *sym*-up conformer is so shallow that no bound states exist for 9FM, and only two subbands are present in the spectrum.

Quantitative fits of the observed subband splittings in the two molecules lead to estimates of approximately 1000 cm^{-1} for the π-hydrogen bond strengths of 9FM in its ground and electronically excited states.

5.7   ACKNOWLEDGEMENTS

5.8   REFERENCES AND NOTES

1. D. W. Pratt, *Ann. Rev. Phys. Chem.* **49**, 481 (1998).

2. E. R. Bernstein, H. V. Secor, and J. I. Seeman, *J. Am. Chem. Soc*. **113**, 4422 (1991).

3. N. Guchhait, T. Ebata, and N. Mikami, *J. Am. Chem. Soc*. **121**, 5705 (1999).

4. M. Mons, E. G. Robertson, L. C. Snoek and J. P. Simons, *Chem. Phys. Lett.* **310,** 423 (1999).

5. M. Mons, E. G. Robertson and J. P. Simons, *J. Phys. Chem. A*. **104,** 1430 (2000).

6. A. Das, K. K. Mahato, S. S. Panja and T. Chakraborty, *J. Chem. Phys*. **119**, 2523 (2003).

7. K. Utzat, A. A. Restrepro, R. K. Bohn, and H. H. Michels, *Int. J. Quant. Chem*. **100**, 964 (2004).

8. R. K. Bohn, *et al.*, in preparation.

9. S. Basu and J. L. Knee, *J. Chem. Phys.* **120**, 5631 (2004).

10. W. A. Majewski, J. F. Pfanstiel, D. F. Plusquellic and D. W. Pratt, in *Laser Techniques in Chemistry.* T. R. Rizzo and A. B. Myers, Eds. J. Wiley & Sons: New York (1995); p. 101.

11. D. F. Plusquellic, Ph. D. Thesis, University of Pittsburgh (1992).

12. S. Gerstenkorn and P. Luc, *Atlas du spectroscopie d'absorption de de la molecule d'iode*, CNRS, Paris (1998/1982).

13. D. F. Plusquellic, R. D. Suenram, B. Maté, J. O. Jensen and A. C. Samuels, *J. Chem. Phys.* **115**, 3057 (2001).

14. W. L. Meerts, W. A. Majewski, and W. M. van Herpen, *Can. J. Phys.* **62**, 1293 (1983).

15. M. J. Frisch, *et al.*, *Gaussian 03*, Revision C.02; Gaussian, Inc.: Wallingford, CT (2004).

16. J. K. G. Watson, *J. Chem. Phys*. **48**, 4517 (1968).

17. (a) J. A. Hageman, R. Wehrens, R. de Gelder, W. L. Meerts, and L. M. C. Buydens, *J. Chem. Phys.* **113**, 7955 (2000). (b) M. Schmitt and W. L. Meerts, in *Handbook of High Resolution Spectroscopy*, edited by M. Quack and F. Merkt (Wiley, New York, 2008).

18. J. T. Yi, L. Alvarez-Valtierra, and D. W. Pratt, *J. Chem. Phys.* **124**, 244302 (2006).

19. W. H. Flygare, *Molecular Structure and Dynamics*, (Prentice-Hall, Englewood Cliffs, NJ, 1978), pp. 120-135.

20. See, for example, J. L. Knee, L. R. Khundkar, and A. H. Zewail, *J. Chem. Phys*. **87**, 115 (1987).

APPENDIX A

FURTHER DISCUSSION AND CALCULATIONS

A.1.1 *Ab initio* calculations

Additional calculations were run for comparison to the measured dipole moments of PABA, 2ABN, and 3ABN. Here, we present the results of ground state calculations run using the second-order Moller-Plesset perturbation (MP2) method[1] and excited state calculations obtained using the configuration interaction of singles (CIS) method, all run with several different basis sets.

Tables A.1 and A.2 compare the experimentally determined dipole moment values of 2ABN, 3ABN and PABA to calculated values in the ground and excited states, respectively. The dipole moment values listed are those calculated for the optimized geometry. Looking at Table A.1, ground state calculations run with an aug-cc-pVDZ basis set are in good agreement with the experimental values for both 2ABN and PABA in the ground state, with the special exception of μ_c.[2] In the case of 3ABN, all basis sets overestimate the values of the dipole moment

Table A.1. Comparison between the experimentally determined dipole moment values of 2ABN, 3ABN and PABA in the ground state and values obtained with *ab initio* calculations performed at the MP2 level of theory using the Gaussian[3] program.

|	Experimental	6-31G**	cc-pVDZ	cc-pVTZ	aug-cc-pVDZ
2ABN					
μ_a (D)	3.6 (1)	3.44	3.23	3.43	3.55
μ_b (D)	1.9 (2)	1.73	1.79	1.85	1.79
μ_c (D)	0.0 (1)	1.05	1.03	0.86	0.84
μ (D)	4.1 (2)	3.99	3.83	3.99	4.06
3ABN					
μ_a (D)	4.8 (3)	5.10	5.03	5.27	5.28
μ_b (D)	1.2 (4)	0.55	0.42	0.51	0.58
μ_c (D)	0.0 (1)	1.19	1.13	0.99	0.97
μ (D)	4.9 (4)	5.26	5.17	5.38	5.40
PABA					
μ_a (D)	3.12 (8)	2.75	2.64	2.98	3.10
μ_b (D)	1.2 (2)	1.24	1.22	1.29	1.31
μ_c (D)	0.00 (1)	-1.18	-1.12	-0.98	-0.96
μ (D)	3.3 (2)	3.24	3.12	3.39	3.50

Table A.2. Comparison between the experimentally determined dipole moment values of 2ABN, 3ABN and PABA in the excited state and values obtained with *ab initio* calculations performed at the CIS level of theory using the Gaussian[3] program.

	Experimental	6-31G**	cc-pVDZ	cc-pVTZ	aug-cc-pVDZ
2ABN					
μ_a (D)	3.4 (2)	3.91	3.59	3.78	3.81
μ_b (D)	3.4 (2)	3.46	3.54	3.51	3.51
μ_c (D)	0.0 (1)	0.00	0.00	0.00	0.00
μ (D)	4.8 (3)	5.22	5.05	5.15	5.18
3ABN					
μ_a (D)	6.8 (3)	8.12	8.04	8.09	7.82
μ_b (D)	0.0 (4)	-0.38	0.55	0.51	0.51
μ_c (D)	0.0 (1)	0.00	0.00	0.00	0.00
μ (D)	6.8 (3)	8.12	8.05	8.11	7.84
PABA					
μ_a (D)	4.21 (8)	5.35	5.07	5.28	6.91
μ_b (D)	1.3 (2)	1.74	1.51	1.49	0.75
μ_c (D)	0.00 (1)	-0.82	-0.82	-0.63	0.00
μ (D)	4.4 (1)	5.69	5.35	5.52	6.95

components. Looking at Table A.2, it can be seen that for all molecules, the values of the dipole moments are overestimated.

A.1.2 PABA resonance structures

Our experimental measurements of PABA's dipole moments in the gas phase provide the ability to assess the relative importance of resonance structures, such as the zwitterionic form seen in Scheme A.1. The expected dipole of the zwitterion is ~ 31 D. It can be concluded that, because our measured values are much smaller than this (see Table A.1), the zwitterionic form is not an important contributor to PABA's structure in the gas phase.
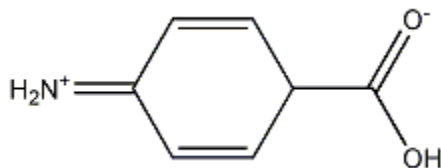
Scheme A.1

A.1.3 Polarizabilities

At the field strengths used in this work, the polarizabilities of the molecules are not expected to contribute significantly to the observed Stark shifts. As a reference, field strengths on the order of 100 kV/cm were required to produce shifts that could be used to measure the polarizability of benzene.[4]

A.1.4 Correlation coefficients

Pearson product-moment correlation coefficients have been calculated from the least squares fits of the Stark data. For the PABA data taken at 677 V/cm, the coefficient for μ_a' and μ_a'' is 0.9, the coefficient for μ_b' and μ_b'' is 0.2, the coefficient for μ_a' and μ_b' is 0.2, and the coefficient for μ_b'' and μ_a'' is -0.1. In general, these values are similar to those for the fits of other field strengths. For the 2ABN data taken at 950 V/cm, the coefficient for μ_a' and μ_a'' is 0.9, the coefficient for μ_b' and μ_b'' is 0.4, the coefficient for μ_a' and μ_b' is 0.0, and the coefficient for μ_b'' and μ_a'' is -0.1. In general, these values are similar to those for the fits of other field strengths, and to the coefficients for the fits of 3ABN.

A.1.5 References

1. A work by Rubio-Pons and Luo [O. Rubio-Pons and Y. Luo, *J. Chem. Phys*. **121**, 157 (2004)] on the ground state dipole moments of PABA determined that hybrid density function theory (at the B3LYP level) failed to reproduce accurate values of the dipole moment, while significant improvements were seen at the MP2 level. Thus, we have focused on MP2 level calculations.

2. Differences in the out-of-plane component of the dipole, μ_c, are anticipated. See the relevant discussions in Chapters 3 and 4.

3. M. J. Frisch, *et al.*, *Gaussian 03*, Revision C.02; Gaussian, Inc.: Wallingford, CT (2004).

4. M. Okruss, R. Müller, and A. Hese, *J. Chem. Phys*. **110**, 10393 (1999).

APPENDIX B

ON THE ORIGIN OF THE THIRD SUBBAND IN 9FMD

Comparison between the ground state energy levels of 9FM and 9FMD, shown in Figure B.1, reveals why a third subband is observed in the spectrum of 9FMD but not that of 9FM. The substitution of hydrogen with deuterium results in a lowering of the energy levels, and, in 9FMD, a bound energy state exists in the upper (*sym*-up) well. The real part of the wavefunction for this state has been plotted, and it can be seen in Figure B.1 that a significant portion of the amplitude lies outside the well; thus deviations in the rotational constants from those of the calculated *sym*-up structure are expected.
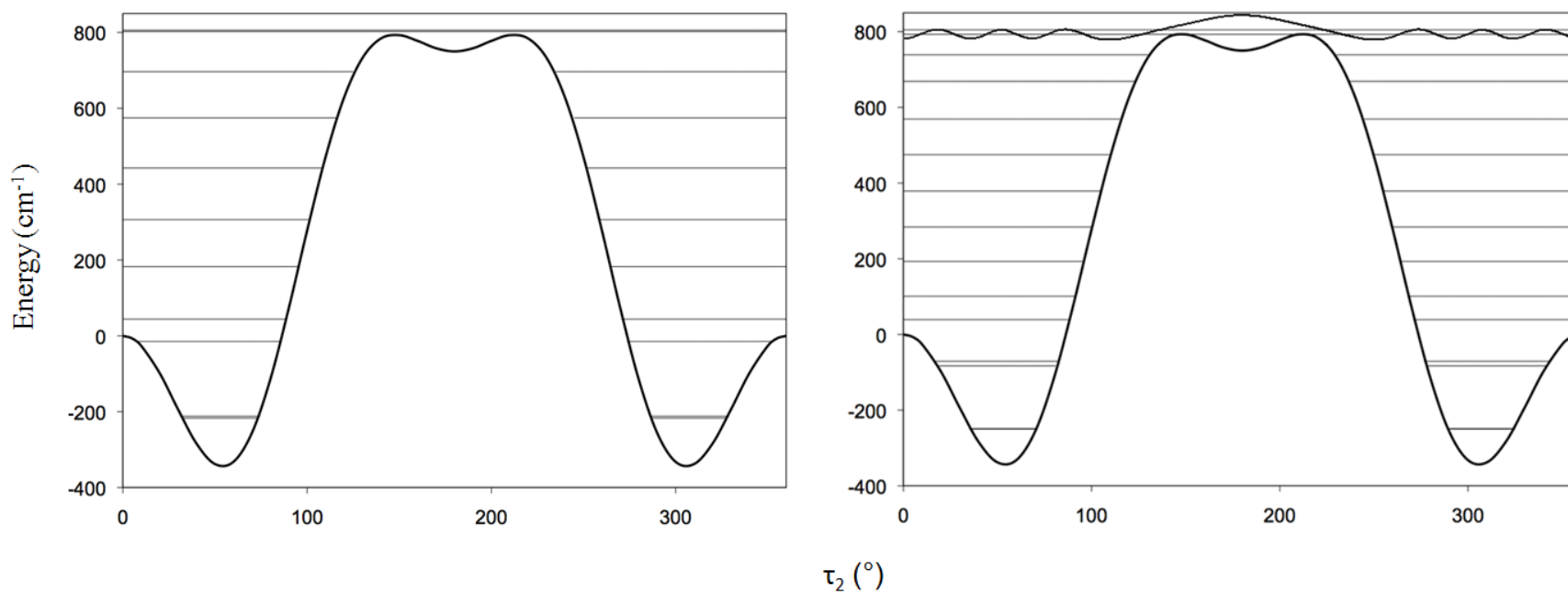
Figure B.1. Ground state potential energy curves plotted against the –OH torsional coordinate (τ_2). On the left, the energy levels of *sym*-9FM are shown, and on the right, the energy levels of *sym*-9FMD are shown. Notice that in 9FMD there is now a bound energy level in the upper well; the real part of the wavefunction has been plotted for this level (the amplitude has been multiplied for visual purposes). $V_1 = 1140$, $V_2 = -303$, and $V_3 = -390$ cm^{-1}.

APPENDIX C

COLLABORATIVE WORK

What follows is a summary of collaborative work. In Part 1, a series of ethynlstyrenes were studied using rotationally resolved experiments to make an unambiguous assignment of conformers. In Part 2, conformers of *p*-vinylphenol, a decomposition product of *p*-coumaric acid, were investigated and assigned.

C.1   *o*-, *m*-, AND *p*-ETHYNYLSTYRENES

This work was published in and is reproduced with permission from *J. Phys. Chem. A*.

C.1.1   Motivation

Substituted benzenes are recognized to play an important role in the pathways to larger polyaromatic hydrocarbons (PAHs) in combustion engines and more generally in flames.[1,2] The

chemical complexity of many of the substituted aromatics in fuel and fuel-rich flames necessarily opens the possibility for structural and conformational isomers. Here, the structural isomers of ethynylstyrene (*o*-, *m*-, and *p*-) have been studied.
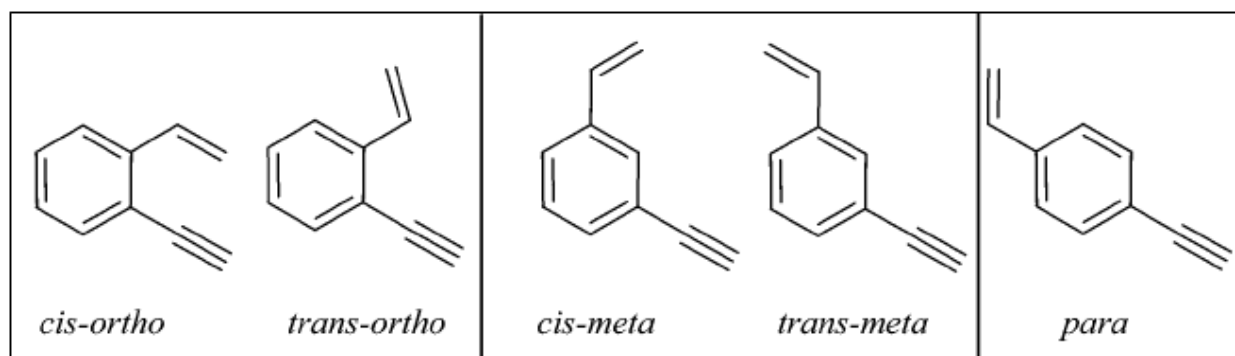
Scheme C.4

C.1.2 Results

In the Zwier lab at Purdue University, *o*-, *m*-, and *p*-ethynylstyrene (*o*ES, *m*ES, and *p*ES) were studied by a combination of methods, including resonance-enhanced two-photon ionization (R2PI), UV-UV hole-burning spectroscopy (UVHB), and resonant ion-dip spectroscopy (RIDIRS). For *m*ES, two conformers were observed (origin bands appearing at 32672 and 32926 cm^{-1}), but it was unclear which band belonged to *cis-m*ES and which belonged to *trans-m*ES. To make a concrete conformational assignment of *m*ES and to probe the structures and transition moments of *m*ES and *p*ES more directly, rotationally resolved fluorescence excitation spectra (FES) were recorded at the University of Pittsburgh for the origin bands of *p*ES and the *m*ES conformer at 32672 cm^{-1}. From the FES, rotational parameters were determined and compared with calculations, and the origin band of *m*ES (32672 cm^{-1}) was assigned to the *cis* structure. By

process of elimination, the *m*ES conformer with an origin band at 32926 cm^{-1} was assigned to the *trans* isomer.

C.1.3 References

1. A. Roubaud, O. Lemaire, R. Minetti, and L. R. Sochet. *Combust. Flame*, **123**, 561 (2000).

2. P. J. Tancell, M. M. Rhead, R. D. Pemberton, and J. Braven. *J. Fuel*, **75**, 717 (1996).

C.2 *p*-VINYLPHENOL

C.2.1 Motivation

Trans-p-coumaric acid (*p*CA) is the chromophore of photoactive yellow protein (PYP). Recently, a new controversy about *p*CA has developed regarding the correct assignment of two closely spaced bands in the $S_1 \leftarrow S_0$ excitation spectrum. Ryan *et al.*[1] reported the first vibrationally resolved fluorescence excitation spectrum of *trans-p*CA in 2002. Later, de Groot and Buma[2] studied the same spectrum with REMPI and found that the two bands were associated with an ion having a mass of 120 amu, rather than the expected mass of 164 amu, causing them to assign the spectrum to *p*-vinylphenol (*p*VP), a thermal decarboxylation product of *trans-p*CA. The method of high resolution electronic spectroscopy was used to resolve this issue.

C.2.2 Results

Rotationally resolved spectra were taken for the two closely spaced bands in the vibrationally resolved $S_1 \leftarrow S_0$ excitation spectrum (see Figure C.1). Both bands were fit, yielding rotational constants that, when compared with theory, showed that the two bands were indeed *p*VP. Band I was assigned to *trans-p*VP, and Band II was assigned to *cis-p*VP.
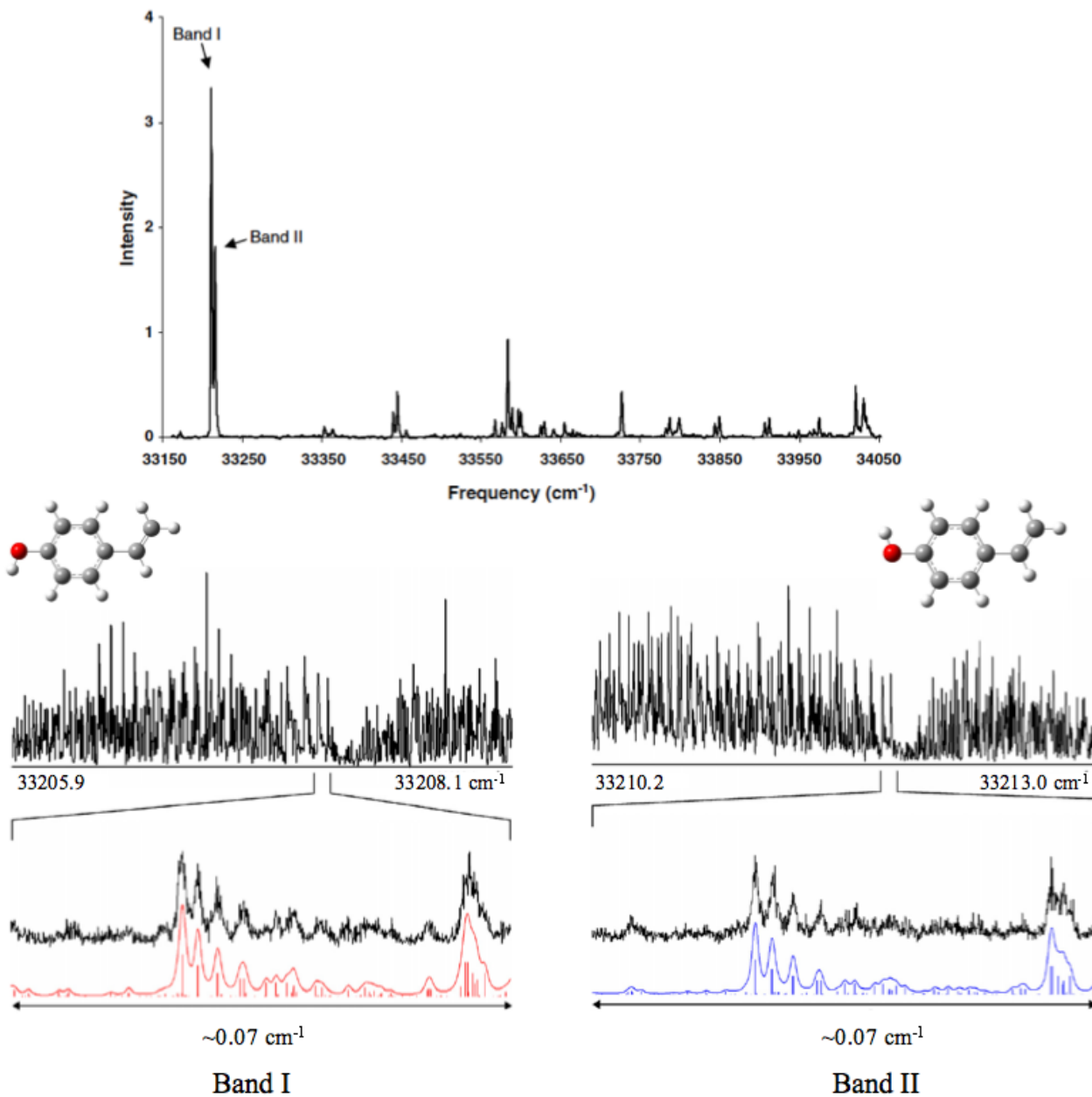
Figure C.1. Vibrationally resolved (upper) and rotationally resolved (lower) $S_1 \leftarrow S_0$ fluorescence electronic excitation spectra the two conformers of pVP.

C.2.3   References

1. W. L. Ryan, D. J. Gordon, and D. H. Levy. *J. Am. Chem. Soc.* **124**, 6194 (2002).

2. M. de Groot and W. J. Buma. *J. Phys. Chem. A*, **109**, 6135 (2005).